NORTHWESTERN UNIVERSITY

Realistic Modeling of Rod Bipolar and AII Amacrine Cells: Synaptic and Intrinsic Properties of Neurons Comprising a Retinal Microcircuit

A DISSERTATION

SUBMITTED TO THE GRADUATE SCHOOL
IN PARTIAL FULFILLMENT OF THE REQUIREMENTS

for the degree

DOCTOR OF PHILOSOPHY

Field of Engineering Sciences and Applied Mathematics

By

Mark Steven Cembrowski

EVANSTON, ILLINOIS

December 2011

Abstract

Realistic Modeling of Rod Bipolar and AII Amacrine Cells: Synaptic and Intrinsic Properties of Neurons Comprising a Retinal Microcircuit

Mark Steven Cembrowski

In order to elucidate how neuronal circuits transform input to output, it is important to characterize the properties of signaling between cells as well as the intrinsic features of individual cells. In this work, we seek to address both of these areas in the context of a retinal microcircuit by studying rod bipolar (RB) and AII amacrine (AII) cells. Our work presented here describes two complementary features of circuit processing: first, we elucidate the mechanisms of synaptic communication between presynaptic RBs and postsynaptic AIIs; second, we describe the membrane conductances and the electrotonic structure of the AII. In both of these areas, we employ computational modeling in close conjunction with experimental recordings.

For the first line of inquiry, we study physiological signaling between presynaptic RBs and postsynaptic AIIs. Using experimental data from the Singer Laboratory, we employ techniques from systems identification to construct a phenomenological description of the transfer function at this synapse. To generate mechanistic insight into these experimental results, we build a realistic model of vesicle cycling at the RB-AII synapse. This model captures experimentally-observed gain changes; moreover, our model demonstrates that different forms of

adaptation can emerge at this synapse due to variable contributions of vesicle depletion, Ca channel inactivation, and uncorrelated release.

For the second line of inquiry studying the intrinsic properties of the AII, we aim to elucidate the mechanisms underlying the small, TTX-sensitive spikes seen at the AII soma. Using a stylized computational model, we show that firing in AIIs can be explained by an unexpected but simple electrotonic structure: spikes in the AII are initiated at a single dendritic location that is electrotonically distal to the soma. We demonstrate that the small spikes recorded at the soma represent filtered waveforms of larger dendritic events that resemble action potentials. This distal spiking is modulated by a source of slow negative feedback, likely an M-type K conductance, that is electrotonically colocalized with dendritic Na. To our knowledge, this description of distal dendritic spiking from a single location is unique among mammalian neurons.

Acknowledgements

First, I would like to thank my two advisors in Applied Math, Hermann Riecke and William Kath. I have absolutely loved my time here as a student at Northwestern, and as I reflect back upon this stage of my life, I realize this is due in large part to the inspiration and guidance that you have provided me. Your tireless contributions and assistance have been invaluable, and I feel incredibly fortunate to have had your mentorship during my time at Northwestern. Thank you for teaching me what it means to be a scientist and for making my graduate student life such a great experience.

I would also like to thank my third advisor, Joshua Singer. I have had a wonderful time being your student and being a part of your laboratory. I want to especially express gratitude for your patience and insight as I learned how to do experiments. Without a doubt, this experience was the most humbling component of my graduate school career, and I thank you for maintaining your faith in me as I acquired data at a snail's pace.

I would also like to extend thanks to my final committee member, David Chopp. Thank you for taking the time to review my thesis and be on my committee.

In my time collaborating with the Singer Laboratory, I have been fortunate to work with many wonderful experimental neuroscientists. I would especially like to thank Tim Jarsky and Stephen Logan, both of whom I have worked with quite closely with during my time at Northwestern. Tim, despite your incredibly busy schedule, you have always found time to help me. I feel quite fortunate that, although you left the laboratory more than a year ago, we still remain in close contact and I continue to learn from you. Steve, thank you for your dedication and continuous contributions to our work here at Northwestern. Many of figures and

conclusions in this thesis would be absent, if not for your technical expertise and willingness to try crazy experiments. Finally, thank you to everyone else that I have worked with in the Singer Laboratory.

A big thanks to all of my friends in the ESAM Department. I have been lucky to be surrounded by a great group of people during my time at Northwestern and I will look back at our experiences fondly.

Without the continual support of my family, I would never have had the courage or strength to pursue such a journey. Mom, Dad, Adam, and John, thank you for being such a loving family and always being there for me. Although we now live farther away than we have before, it still feels as though we are as close as ever.

Finally, and most importantly, thank you to my wife Shannon. It has been an incredible adventure here in Chicago, filled with times both wonderful and trying. Thank you so much for your ever-present patience and support, especially throughout all the (numerous) days and nights that I've been stressed or busy. I wouldn't have been able to do it without you. I can recall four years ago when moving and starting a new life in Chicago was a daunting prospect; as we now draw near to the end of this journey, I am so glad we took this risk and I thank you for taking this leap of faith. I am so lucky to have spent this time with you and I am very excited for our next adventure together.

Table of contents

List of Tables

List of Figures

CHAPTER 1

Introduction

Computational neuroscience has produced multiple foundational insights into nervous system behavior by providing a means to investigate functionality that would be intractable through experimental methods. The gold standard of this field is the work of Hodgkin and Huxley, who elucidated the ionic mechanisms of the action potential by describing their dynamics through a system of nonlinear ordinary differential equations. This work represents a triumph in developing realistic and informative models, and serves as a testament to the power that mathematics can have when applied closely to neuronal data.

The focus of this thesis is to build realistic computational models, founded upon experimental data, in order to elucidate synaptic and intrinsic neuronal functionality in a retinal microcircuit. This microcircuit is comprised of the rod bipolar cell (RB) and AII amacrine interneuron (AII), in which we pursue two complementary lines of inquiry. First, we elucidate the properties of synaptic transmission between RBs and AIIs. In this section, we demonstrate that signaling at this synapse adapts to both the mean and variance of the stimulus, and we suggest differential contributions from three mechanisms which together can account for these adaptations. Second, we investigate the intrinsic properties of the AII interneuron, with a particular focus on clarifying the mechanisms underlying the atypical spiking seen in these axonless cells. We show that spiking likely arises from a single, electrotonically-distal dendritic location, suggesting that AIIs possess a dendritic compartment that bears similarities to an axon initial segment in conventional neurons.

1.1. The retina and the rod bipolar pathway

The mammalian visual system can reliably encode stimuli ranging from starless nights to bright, sunny days; this dynamic range is remarkable considering that these scenes vary in light intensity by 10-12 orders of magnitude. The retina is the first major component of this system and is tasked with transforming incident photons into a continuous, informative neuronal representation of the visual environment. Despite the wide range of stimuli encountered both throughout the day and within a given visual scene, the retina effectively provides higher brain areas with signals to reconstruct much of the visual environment; moreover, the retina even performs many complex operations itself (Gollisch and Meister, 2010). Among the techniques that the retina uses to preserve signal fidelity is to employ multiple pathways, each performing distinct operations, in order to convey parallel signals from input photoreceptors to output ganglion cells (Bloomfield and Dacheux, 2001; Sharpe and Stockman, 1999).

One particular retinal pathway that has received significant attention is termed the rod bipolar pathway (Tsukamoto et al., 2001). This circuit operates during illumination akin that of moonless nights (Deans et al., 2002; Volgyi et al., 2004), near the absolute threshold for vision (Field et al., 2005). Within this circuit, input is derived at rod photoreceptors (Fig. 1.1). Rods signal to rod bipolar cells (RBs) (Field and Rieke, 2002; Sampath and Rieke, 2004), which in turn relay signals to AII amacrine cells (AIIs) via excitatory glutamatergic synapses (Dacheux and Raviola, 1986). AIIs then divide these signals into the parallel ON and OFF pathways. Signals to the ON stream are routed to ON cone bipolars (CBs) via gap junctions (Veruki and Hartveit, 2002b), which deliver signals to ON ganglion cells (GCs) (Freed, 2000; Levitan and Buchsbaum, 1996). Transmission to the OFF stream is predominantly conveyed from AIIs

directly to OFF GCs via inhibitory glycinergic synapses (Margolis and Detwiler, 2007; van Wyk et al., 2009). Both ON and OFF classes of GCs subsequently relay signals to higher brain centres via the optic nerve.

This thesis studies the RB and the AII within this retinal circuit, in particular investigating two complementary areas. First, excitatory glutamatergic signaling from RBs to AIIs is studied. This synapse has been implicated as a key source of gain control within the retina (Dunn et al., 2006; Dunn and Rieke, 2008); here, we seek to clarify how this synapse adapts to different RB command protocols. Second, the intrinsic properties of the AII are studied. This cell is central in the RB pathway (Dacheux and Raviola, 1986; Tsukamoto et al., 2001) and has also been shown to be directly involved in several other modes of vision (Field et al., 2009; Manookin et al., 2008; Munch et al., 2009); therefore, elucidating this interneuron may help to clarify processing in several distinct retinal circuits.

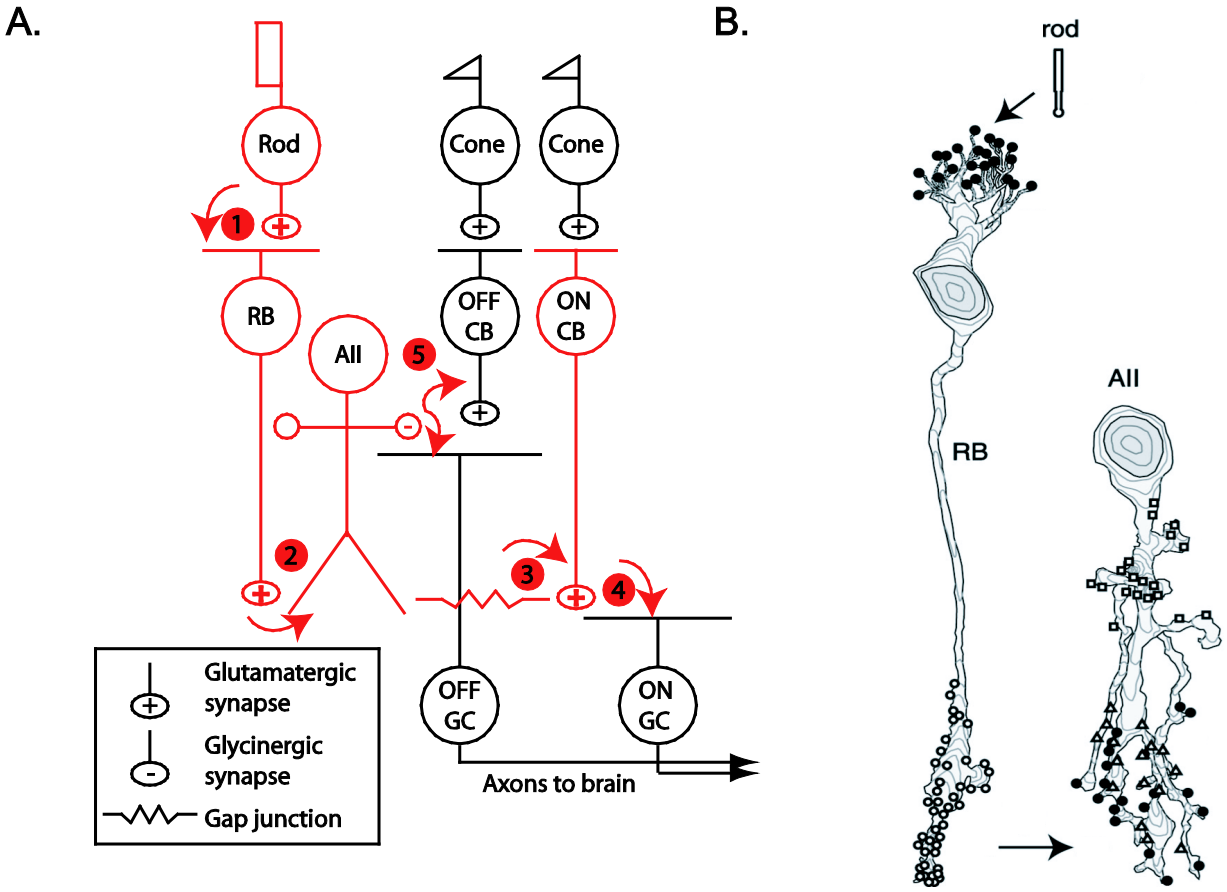

Figure 1.1. The rod bipolar pathway of the mammalian retina
A. Schematic of basic circuitry in the mammalian retina. Arrows indicate the direction of signaling in the RB pathway, relaying signals from input at rod photoreceptors to output at GCs. B. Electron microscopic reconstructions of an RB (left) and an AII (right) (from Tsukamoto et al., 2001). Open circles on the RB indicate presynaptic active zones which contact AIIs. Black circles on the AII denote contacts from presynaptic RBs.

1.2. The rod bipolar cell and the RB-AII synapse

In this section, we provide a summary of the intrinsic behavior of the RB cell, as well as the contributions that the RB gives to network processing. The initial subsections (Sects. 1.2.1-1.2.3) are dedicated to providing a condensed and comparative summary of the work done in each of these areas. The final subsection (Sect. 1.2.4) is intended to provide motivation and context for our work on the RB-AII synapse.

1.2.1. Role of the RB in visual processing

The RB cell has traditionally been studied for its role as a central neuron within the rod bipolar pathway; indeed, it is now believed that this is the only circuit where the RB plays an important role. Within this pathway, RBs are the second-order neuron, receiving input from rod photoreceptors. Synaptic transmission from rods to RBs occurs via a sign-inverting metabotropic glutamate receptor, causing presynaptic glutamate release from rods to hyperpolarize postsynaptic RBs (Field and Rieke, 2002; Sampath and Rieke, 2004). RBs in turn relay signals to two postsynaptic cells via dyad synapses, contacting both AII and A17 amacrine interneurons (Raviola and Dacheux, 1987). Signaling to AIIs is strictly unidirectional, whereas the A17 imposes feedback inhibition on the RB terminal (Dong and Hare, 2003; Freed et al., 2003; Grimes et al., 2009).

It has been demonstrated that RBs respond sluggishly to light, exhibiting both disinhibitory (that is, removal of inhibitory) synaptic inputs (Field and Rieke, 2002) and membrane depolarizations (Dacheux and Raviola, 1986; Euler and Masland, 2000; Trexler et al., 2005) that last for hundreds of milliseconds. The latter slow, sustained voltage responses have

led to RBs being traditionally classified as analog neurons (Masland, 2001). However, contrasting results from other studies have reported Ca-mediated spike behavior in zebrafish RBs *in vitro* (Palmer, 2006; Protti et al., 2000) and more recently *in vivo* (Dreosti et al., 2011). Similar spiking has also been demonstrated in mammalian RBs (rat; Ma and Pan, 2003). The reasons for the different signaling modes between experiments are unknown, and thus, the mode of the output that the RB employs in a physiological setting is currently uncertain.

1.2.2. Intrinsic properties of the RB

Little, too, is known about the intrinsic properties of RBs. One study has demonstrated that RBs express HCN channels, a type of slow, voltage-gated nonspecific conductance. This conductance can enable the cell to act as a band-pass filter with sufficient hyperpolarization (Cangiano et al., 2007) (see also Ma et al., 2003). The consequences of this conductance at a circuit level are unclear, however, as this modulation occurs at potentials far below the threshold for synaptic release to occur (Jarsky et al., 2010). Another study has demonstrated that exocytosis is mediated exclusively through L-type Ca channels (Jarsky et al., 2010) (but see Pan et al., 2001), which are present in the axon terminals of RBs (Pan, 2000). Two studies have characterized voltage-gated K channels in RBs, with one showing strong inactivation (Klumpp et al., 1995a) and the other showing noninactivation (albeit on shorter timescales; Hu and Pan, 2002). Finally, RBs are not believed to express Na channels (Pan and Hu, 2000; Tian et al., 2010), in contrast with conventional neurons.

1.2.3. RB-AII signaling

RBs contact AIIs through structures termed ribbon synapses (Sterling and Matthews, 2005). These types of synaptic contacts, designed to facilitate vesicular release in analog neurons, tether presynaptic vesicles close to active zones. At the RB-AII synapse, Ca channels are closely located to these docking sites and underlie nanodomain coupling with release machinery for brief stimuli (Jarsky et al., 2010). Postsynaptically, the AII reads off release with AMPA-type receptors (e.g., Morkve et al., 2002; Singer and Diamond, 2003; Veruki et al., 2003). In addition, some studies suggest AIIs also employ NMDA receptors (Boos et al., 1993; Hartveit and Veruki, 1997); however, other work has not found evidence for this property (Fletcher et al., 2000; Singer and Diamond, 2003).

Study of release from RBs has received particular attention for at least three reasons. First, in goldfish, the giant Mb1 bipolar cell (the analog of the mammalian RB) has been a model cell to study presynaptic vesicle dynamics. This cell contains an usually large synaptic terminal that can be employed for high signal-to-noise capacitance recordings (e.g., Heidelberger et al., 1994; Palmer et al., 2003). As a consequence, this cell has been used to study both endo- and exocytosis, with capacitance measurements helping to avoid any potential complications from soma-axonal filtering or postsynaptic receptor effects.

Second, in mammals, this synapse has been implicated to be the predominant site of gain adaptation within the RB pathway (Dunn et al., 2006). Within this circuit, it has been shown that responses to single photons modulate gain at the RB-AII synapse by evoking synaptic depression that can last hundreds of milliseconds (Dunn and Rieke, 2008). Although it has been shown that this feature arises from presynaptic properties, the specific mechanisms involved in this

depression are currently unknown; based on the timescale of depression, a likely candidate would be vesicle depletion (Singer and Diamond, 2006; Singer et al., 2004).

Finally, the relative simplicity of the RB and the RB-AII synapse conveys numerous advantages to studying this microcircuit in an experimental setting. First, the relatively low-level nature of the RB within the retina suggests the RB can be stimulated electrically in a manner which well-approximates physiological light stimuli. Second, the basic morphology of the RB enables the axon terminal voltage to be successfully controlled from somatic recordings (Jarsky et al., 2010). Third, RBs are believed to comprise just a single cell type (but see Pang et al., 2004). Fourth, postsynaptic receptor effects in the AII are believed to be minimal, as the synapse appears to operate without desensitization or saturation (Singer and Diamond, 2006; Singer et al., 2004; Veruki et al., 2003); thus, postsynaptic voltage-clamp recordings are believed to reflect presynaptic dynamics only.

1.2.4. Work presented: signal transmission at the RB-AII synapse

The RB-AII synapse has generally been studied in two ways. In one set of experiments (Dunn et al., 2006; Dunn and Rieke, 2008), all synaptic and intrinsic conductances were left intact, the retina was stimulated with light, and single electrode recordings of RBs and AIIs were performed. These experiments represent the best to date with regards to understanding the true physiology of the RB pathway; however, ascertaining a mechanistic understanding of RB-AII contributions is difficult due to the uncontrolled nature of the experimental protocol. In a second set of experiments (Singer and Diamond, 2003, 2006; Singer et al., 2004), both the RB and the AII recorded were recorded simultaneously in voltage-clamp with many synaptic and intrinsic conductances blocked. These experiments are crucial to constrain the properties of the synapse,

but the voltage commands used to drive the RB were unlikely to be encountered in a physiological setting.

The work presented here represents an intermediate between the two previous strategies, directly investigating transmission at the RB-AII synapse while using relatively physiological stimuli (Jarsky et al., 2011). To study signaling at this synapse, we employ a hybrid of theoretical and experimental techniques. First, using experimental data from the Singer Laboratory, we use LN cascade modeling to construct an RB-AII transfer function; this provides a quantitative assessment of gain changes when either the mean or the standard deviation (SD) of the RB command potential is varied. Second, we construct a model of vesicle cycling to clarify the mechanisms underlying gain changes at this synapse. This model suggests that adaptation emerges through variable contributions from vesicle depletion, Ca inactivation, and uncorrelated release.

1.3. The AII amacrine cell

As in the previous section, here we provide a summary of the intrinsic and network properties of the AII interneuron. We initially summarize previous work in both of these areas (Sects. 1.3.1-1.3.3), and subsequently provide background relevant to our study of the atypical spiking seen in the AII (Sect. 1.3.4).

1.3.1. Role of the AII in visual processing

Like RBs, AIIs have been traditionally studied for the role they play within the RB pathway (Dacheux and Raviola, 1986; Strettoi et al., 1992). Within this circuit, the gap junction-coupled AII network is believed to be critical for preserving weak signals in the presence of neuronal noise, as disruption of AII coupling eliminates responses in high-sensitivity ganglion cells (Deans et al., 2002; Volgyi et al., 2004). AIIs themselves have been shown to have a very high sensitivity, which is believed to emerge from the convergence of upstream cells: AIIs pool from ~200 rods directly and ~300 indirectly via gap junction coupling (Sterling et al., 1988). This convergence enables dark-adapted AIIs to have several log units more sensitivity than upstream rods and RBs (Dunn and Rieke, 2006; Pang et al., 2004). Correspondingly, AIIs saturate at lower light intensities than upstream circuitry (but see Xin and Bloomfield, 1999).

The light responses of AIIs are markedly briefer than those of presynaptic RBs (Nelson, 1982; Trexler et al., 2005). It is has been suggested that both depletion (Singer and Diamond, 2006; Singer et al., 2004) and adaptation from a Ca sensor (Hsu et al., 1996; Snellman et al., 2009) could underlie this signal "sharpening". This sharpening has been proposed to enable downstream ganglion cells to fire reproducible spike trains (within milliseconds) to repeated

stimuli (Murphy and Rieke, 2006) despite the sluggish response (hundreds of milliseconds) of both rods and RBs.

It has been demonstrated that signals propagate more effectively from AIIs to ON CBs than in the opposite direction, a property attributable to the AII-ON CB impedance mismatch (Pang et al., 2004; Veruki and Hartveit, 2002b). This finding had motivated previous notions that the AII might play a minimal role in cone-based vision. However, two recent studies have illustrated that AIIs are important in driving daylight vision in the light-adapted retina (Manookin et al., 2008; Munch et al., 2009; Oesch and Diamond, 2009). In both of these studies, disinhibition arising from the cone→ ON CB → AII → OFF GC circuit was shown to play an important role in driving OFF GC responses. Thus, the AII plays multiple roles within the mammalian retina.

1.3.2. Intrinsic properties of the AII

AIIs have been suggested to contain Nav1.1 subunits (Kaneko and Watanabe, 2007), although studies have reached different conclusions about whether AIIs act as spiking (Bloomfield and Xin, 2000; Boos et al., 1993; Tamalu and Watanabe, 2007; Tian et al., 2010; Veruki and Hartveit, 2002a, b) or nonspiking (Bloomfield, 1992; Nelson, 1982) neurons. The reasons for this discrepancy are unknown; in other retinal cells, Na channel-mediated spiking has been shown to be sensitive to factors like age (Zhou and Fain, 1996) and dopamine levels (Ichinose and Lukasiewicz, 2007).

The mechanisms involved in this firing, too, are unclear: many features of the AII somatic spike waveform are profoundly different than in conventional neurons. AII spikes, as recorded at the soma, are small (<10 mV), broad (>5 ms half-width), lack after-

hyperpolarizations, and can exhibit superposition. Despite these atypical features, it is interesting to note that AIIs do bear several similarities with classical fast-spiking interneurons: they are parvalbumin-positive (Casini et al., 1995; Wassle et al., 1993), likely contain Nav1.1 subunits, and can spike at rates up to hundreds of Hz.

To date, only one study has investigated voltage-gated Ca channels in AIIs. In this work, L-type Ca channels were shown to be localized to lobules presynaptic to OFF CBs and GCs (Habermann et al., 2003). These channels are believed to exclusively mediate chemical synaptic release to OFF CBs and OFF GCs, as no other types of voltage-gated Ca conductances were found in the AII.

Several studies have investigated K channels present within the AII. Two complementary studies have demonstrated the presence of a high voltage-activated A-type K channel; interestingly, one study demonstrated that this conductance was almost entirely 4-aminopyridine (4-AP) insensitive (Boos et al., 1993) whereas another showed near-complete block at lower concentrations (Tian et al., 2010). In addition, one study has suggested the presence of Ca-activated K conductances in the AII, as voltage-clamp protocols showed outward currents sensitive to antagonists of BK channels (Grimes et al., 2009). Finally, immunohistochemical results indicate AIIs may contain a delayed rectifier channel (Klumpp et al., 1995b), although this has yet to be directly verified.

1.3.3. Gap junction coupling and network properties

AIIs are coupled via gap junctions both homotypically to other AIIs (Veruki and Hartveit, 2002a), as well heterotypically to ON CBs (Veruki and Hartveit, 2002b). At a molecular level, AII-AII gap junction coupling is formed by connexin 36 (CX36) at both hemichannels

(Feigenspan et al., 2001), whereas AII-ON CB gap junctions occur through CX36 expression in AIIs and CX45 in ON CBs (Li et al., 2008; Maxeiner et al., 2005). Correspondingly, many physiological properties of these two types of gap junctions differ (Mills and Massey, 1995). Notably, the strength of gap junction coupling between AIIs is modulated by ambient illumination, a feature that is not found in AII-ON CB gap junctions (Bloomfield et al., 1997; Petrides and Trexler, 2008). This plasticity causes the AII network to be relatively uncoupled in the dark- and light-adapted retina, with stronger coupling emerging at intermediate illuminations.

Several different computational studies have investigated the role that gap junction coupling might play in rod-driven vision (Publio et al., 2009; Smith and Vardi, 1995; Vardi and Smith, 1996). The gap junction coupling itself has been suggested to enable amplified responses to correlated upstream signals while discarding uncorrelated noise (Smith and Vardi, 1995). This gap junction coupling may then produce correlations in downstream ganglion cells (Vardi and Smith, 1996). Other simulations have suggested the adaptation in gap junction conductance may modestly increase the dynamic range of rod-based vision (Publio et al., 2009).

1.3.4. Work presented: spiking in the AII amacrine interneuron

Many intrinsic features of the AII have not been well characterized. A striking example of this is AII spiking: it is unclear why the AII exhibits many physiological features similar to conventional fast spiking interneurons, yet produces spike waveforms unlike these classical cells. As the AII has recently been shown to be involved in multiple modes of vision, clarifying the intrinsic properties of this interneuron is an important goal for understanding signal processing within the retina.

The work presented here seeks to clarify the intrinsic properties of the AII interneuron by constructing multicompartmental models in conjunction with patch-clamp electrophysiology. We demonstrate that the AII spike waveform, as seen in somatic recordings, likely represents a filtered version of action potential-like dendritic spiking. Importantly, these spikes arise from a single location, as simulations with multiple independent initiation sites create predictions that deviate from experimental data. This distal spiking is modulated via slow negative feedback from a channel exhibiting kinetics, gating properties, and pharmacological sensitivities consistent with an M-type K channel. Our work suggests that the AII amacrine cell has a single, electrically isolated dendritic compartment that bears similarities to an axon initial segment found in traditional neurons.

1.4. Linear-nonlinear modeling

The goal of this section is to provide background and context for the LN modeling technique employed in Section 2.

1.4.1. Motivation for LN modeling

The basis for LN cascade modeling used to study many physiological systems (Marmarelis and Marmarelis, 1978) is built on the conceptual foundation of the Volterra series (Volterra, 1959). In this work, it is demonstrated that an explicit representation of a function (i.e., the output y) can be expressed in terms of a causally-related function (i.e., the input x) according to

$$y\big(x(t)\big) = k_0 + \int_{-\infty}^{\infty} k_1(\tau)x(t-\tau)d\tau + \int_{-\infty}^{\infty}\int_{-\infty}^{\infty} k_2(\tau_1,\tau_2)x(t-\tau_1)x(t-\tau_2)d\tau_1 d\tau_2 + \cdots, \qquad (1.4.1)$$

given that the system is analytic, time-invariant, and has finite memory. Here, k_i, $i = 0,1,2,\ldots$, are referred to as the Volterra kernels of the system and are unique. The Volterra kernels are symmetric functions of their arguments, and due to causality, obey $k_i = 0$ whenever any argument is less than zero.

One drawback to the Volterra series expansion, however, is that the kernels are not independent of one another. If one seeks to approximate a system using a finite number of terms N from (1.4.1), then the k_i $(i = 0,1,2,\ldots,N)$ calculated will depend on, in effect, the number of terms employed in the series expansion. Increasing or decreasing the number of terms in the expansion requires all kernels to be recalculated.

To improve upon this, the Volterra series expansion was later refined to produce an orthogonal basis of functionals, provided that the input x was chosen to be Gaussian white noise (Wiener, 1958). In this so-called Wiener functional expansion,

$$y\big(x(t)\big) = \sum_{i=0}^{\infty} G_i[h_i(\tau_1, \cdots, \tau_m); x(t)]. \tag{1.4.2}$$

Here, G_i are functionals that take as arguments the zero-mean Gaussian white-noise signal $x(t)$ and the unique Wiener kernels of the system h_i. In this expansion, each functional G_i is made orthogonal to all other functionals by subtracting any non-orthogonal components from lower-order terms.

To begin, the first functional $G_0[h_0; x(t)] = h_0$ is taken to be constant. To next order,

$$G_1[h_1; x(t)] = C_1^0 . + \int_{-\infty}^{\infty} h_1(\tau) x(t-\tau) d\tau. \tag{1.4.3}$$

To satisfy orthogonality with the lower order functional G_0,

$$< G_0 G_1 > = < h_0 (C_1^0 . + \int_{-\infty}^{\infty} h_1(\tau) x(t-\tau) d\tau) >, \tag{1.4.4}$$

which is automatically satisfied when $C_1^0 = 0$ (as $< x(t-\tau) > = 0$). Thus,

$$G_1[h_1; x(t)] = \int_{-\infty}^{\infty} h_1(\tau) x(t-\tau) d\tau. \tag{1.4.5}$$

G_2 is expressed as

$$G_2[h_2; x(t)] = C_2^0 . + C_2^1 \int_{-\infty}^{\infty} h_1(\tau) x(t-\tau) d\tau + \int_{-\infty}^{\infty} \int_{-\infty}^{\infty} h_2(\tau_1, \tau_2) x(t-\tau_1) x(t-\tau_2) d\tau_1 d\tau_2. \tag{1.4.6}$$

It can be shown that the expected value of the product of an odd number of zero-mean Gaussian random variables is 0, and therefore $< G_1 G_2 > = 0$ requires $C_2^1 = 0$. Also, for $< G_0 G_2 > = 0$ to hold, $C_2^0 = -P \int_{-\infty}^{\infty} h_2(\tau, \tau) d\tau$, where P is the variance of the Gaussian white noise process. Therefore,

$$G_2[h_2; x(t)] = -P\int_{-\infty}^{\infty} h_2(\tau,\tau)d\tau + \int_{-\infty}^{\infty}\int_{-\infty}^{\infty} h_2(\tau_1,\tau_2)x(t-\tau_1)x(t-\tau_2)d\tau_1 d\tau_2. \quad (1.4.7)$$

The higher-order functionals G_i $(i = 3,4,\cdots)$ can be calculated in an analogous procedure.

One advantage of the orthogonal Wiener series expansion is that it circumvents the interrelatedness of kernels associated with the more general Volterra series. As a consequence of this orthogonality, for a Wiener series expansion using a finite number of terms N, it can be shown that the truncated Wiener expansion $y_N\big(x(t)\big) = \sum_{i=0}^{N} G_i[h_i(\tau_1,\cdots,\tau_m); x(t)]$ gives the best approximation to $y\big(x(t)\big)$ (in the mean squared error sense) out of all possible functional expansions of order N.

One technique for extracting the kernels is via cross-correlation (Lee and Schetzen, 1965). According to this method, the filter h_n $(n = 1,2,\cdots)$ can be obtained after evaluating the n^{th}-order input-output cross-correlation (that is, after solving $< y(x(t))\prod_{i=1}^{n} x(t-\sigma_i) >$); the $n = 0$ case for h_0 can be evaluated simply by noting

$$< y\big(x(t)\big) > = < \sum_{i=0}^{\infty} G_i[h_i(\tau_1,\cdots,\tau_m); x(t)] >, \quad (1.4.8)$$

$$= h_0, \quad (1.4.9)$$

as all higher-order terms vanish due to orthogonality.

For example, to calculate h_1,

$$< x(t-\sigma)y\big(x(t)\big) > = < x(t-\sigma)\sum_{i=0}^{\infty} G_i[h_i(\tau_1,\cdots,\tau_m); x(t)] >, \quad (1.4.10)$$

$$= < x(t-\sigma)[h_0 + \int_{-\infty}^{\infty} h_1(\tau)x(t-\tau)d\tau +$$

$$+ \int_{-\infty}^{\infty}\int_{-\infty}^{\infty} h_2(\tau_1,\tau_2)x(t-\tau_1)x(t-\tau_2)d\tau_1 d\tau_2$$

$$- P\int_{-\infty}^{\infty} h_2(\tau,\tau)d\tau + \cdots] >. \quad (1.4.11)$$

Note

$$< x(t-\sigma)h_0 > = 0, \quad (1.4.12)$$

as x is zero mean Gaussian white noise. Also,

$$< x(t-\sigma) \int_{-\infty}^{\infty} h_1(\tau)x(t-\tau)d\tau > = \int_{-\infty}^{\infty} h_1(\tau) < x(t-\tau)x(t-\sigma) > d\tau \,, \quad (1.4.13)$$

$$= \int_{-\infty}^{\infty} h_1(\tau)P\delta(\sigma-\tau)d\tau \,, \quad (1.4.14)$$

$$= P\, h_1(\sigma). \quad (1.4.15)$$

Again, all the higher-order remaining terms cancel due to orthogonality. Rearranging this gives

$$h_1(\sigma) = P^{-1} < x(t-\sigma)y\big(x(t)\big) >. \quad (1.4.16)$$

The nonlinear filters can be extracted in an analogous procedure by employing higher order cross-correlations of the input with the output.

1.4.2. LN modeling of biological systems

Note that a system driven by Gaussian white noise is completely identified once the kernels h_i have been calculated. In principle, these kernels can be obtained in an experimental setting by analyzing the output of neurons stimulated by white noise. However, in practice the amount of data that can be acquired is limited, which typically causes the nonlinear kernels to be noisy and limits their predictive power (but see, e.g., Juusola et al., 1995; Korenberg et al., 1989). This imposes a severe constraint on the success of Wiener series expansions in describing neurons, as these cells behave in a highly nonlinear fashion and would typically require the accurate calculation of many nonlinear kernels to be modeled effectively.

As a means of circumventing this drawback, one common approach is to use an LN cascade model to predict neuronal responses (Chichilnisky, 2001). In this formalism, a linear filter $f(t)$ is convolved with the white noise stimulus $x(t)$ to produce a linearly-filtered stimulus $L(x(t)) = f(t) * x(t)$ (typically referred to as the "linear prediction" or "generator signal"). A

static nonlinear mapping N is then applied to the linearly-filtered stimulus $L(x(t))$ to give the model output $\hat{y}\big(x(t)\big) = N\big(L(x(t))\big)$. As described below, this technique has an intuitive explanation: LN output can be viewed as a nonlinear mapping of an input filtered by the first order Wiener kernel.

In order to determine the LN output, both the linear filter f and the static nonlinearity N must be assigned. From the theory underlying the Wiener series expansion, the first Wiener kernel $h_1 \propto < y\, x >$ gives the optimal linear filter for a system driven by Gaussian white noise. Within the LN model, choosing $f = h_1$ endows the model with this optimality and ensures that model and experimental linear filters are equivalent: $< \hat{y}\, x > \propto h_1$ is guaranteed, regardless of nonlinearity N, due to following argument (Chichilnisky, 2001).

First,

$$< \hat{y}\, x > = \sum_i \sum_j x_i\, \hat{y}_j\, p(x_i, \hat{y}_j), \tag{1.4.17}$$

$$= \sum_i \sum_j x_i\, \hat{y}_j\, p\big(\hat{y}_j | x_i\big) p(x_i), \tag{1.4.18}$$

$$= \sum_i x_i\, p(x_i) \sum_j\, \hat{y}_j\, p(\hat{y}_j | x_i). \tag{1.4.19}$$

$$= \sum_i x_i\, p(x_i)\, \hat{y}(x_i), \tag{1.4.20}$$

$$= \sum_i x_i\, p(x_i) N(h_1\, x_i), \tag{1.4.21}$$

Note that in (1.4.19), we used the fact that $\sum_j\, \hat{y}_j\, p(\hat{y}_j | x_i)$ is simply the LN output given the stimulus x_i. Next, due to the symmetry of the Gaussian white noise stimuli, for any stimulus x_i there is another stimulus $\tilde{x}_i$ symmetric about h_1 that occurs with equal probability; that is, $h_1\, x_i = h_1\, \tilde{x}_i$, $p(x_i) = p(\tilde{x}_i)$, and $x_i + \tilde{x}_i \propto h_1$. The sum (1.4.21) can thus be written

$$< \hat{y}\, x > = \frac{1}{2} [2\, \sum_i x_i\, p(x_i) N(h_1\, x_i)], \tag{1.4.22}$$

$$= \frac{1}{2} [\, \sum_i x_i\, p(x_i) N(h_1\, x_i) + \sum_i \tilde{x}_i\, p(\tilde{x}_i) N(h_1\, \tilde{x}_i)\,], \tag{1.4.23}$$

$$= \frac{1}{2}[\sum_i x_i\, p(x_i) N(h_1\, x_i) + \sum_i \tilde{x}_i\, p(x_i) N(h_1\, x_i)\,]. \quad (1.4.24)$$

$$= \frac{1}{2}\sum_i (x_i + \tilde{x}_i) p(x_i) N(h_1\, x_i). \quad (1.4.25)$$

$$\propto \sum_i h_1\, p(x_i)\, N(h_1\, x_i). \quad (1.4.26)$$

$$= h_1 \sum_i\, p(x_i)\, N(h_1\, x_i). \quad (1.4.27)$$

$$\propto h_1, \quad (1.4.28)$$

which is the relation we sought to demonstrate.

As choosing the linear filter $f = h_1$ determines the internal signal $L(x(t))$, to produce $\hat{y}$ it remains only to choose the static nonlinearity N. In practice, this is usually done by assigning a functional form to N and fitting N by regressing the output of the system $y\big(x(t)\big)$ against the linearly-filtered stimulus $L(x(t))$.

This LN cascade modeling has been particularly successfully in capturing responses in a variety of retinal cell types (Baccus and Meister, 2002; Kim and Rieke, 2001; Liang and Freed, 2010; Rieke, 2001; Wang et al., 2011; Zaghloul et al., 2003), and has also performed well in predicting spike trains in higher brain areas (reviewed in Carandini et al., 2005).

1.4.3. Adjusting for stimulus correlations

In practice, white noise stimuli used in experiments deviates from the mathematically-idealized process employed in the Wiener series approach. In part, this is attributable to unavoidable physical constraints: requirements like infinite record length and infinite stimulus bandwidth cannot be realized in an experimental setting. In addition to these inevitable deviations, other optional departures are sometimes employed by the experimentalist.

In the study of neurobiological systems in particular, one frequent deviation used in practice is the use of band-limited Gaussian noise. In this procedure, realizations of Gaussian white noise are low-pass filtered offline prior to being used as stimuli. This causes the expression $< x(t-\tau)x(t-\sigma) > = P\delta(\sigma-\tau)$ to no longer be valid. These correlations can be adjusted for, however, by first applying the Fourier transform F to the first-order cross-correlation:

$$F\left\{< x(t-\sigma)\, y\big(x(t)\big) >\right\} = F\left\{< x(t-\sigma) \int_{-\infty}^{\infty} h_1(\tau)\, x(t-\tau)\, d\tau >\right\}. \quad (1.4.29)$$

Writing $F\{y\} = Y(k)$ and $F\{x\} = X(k)$, this can be written (via the Fourier transform of a cross-correlation) according to

$$X^*(k)\, Y(k) = X^*(k) F\Big\{ \int_{-\infty}^{\infty} h_1(\tau)\, x(t-\tau)\, d\tau\Big\}. \quad (1.4.30)$$

Next, using the Fourier transform of a convolution and writing $F\{h_1\} = H_1(k)$, the above can be expressed as

$$X^*(k)\, Y(k) = X^*(k) H_1(k) X(k), \quad (1.4.31)$$

and rearranging to solve for $H_1(k)$ yields

$$H_1(k) = \frac{Y(k)X^*(k)}{X(k)X^*(k)}. \quad (1.4.32)$$

Finally, the corrected linear filter can be ascertained by inverting $H_1(k)$.

Note that the denominator $X(k)X^*(k)$ is the power spectrum of the input. Thus, for the case of unfiltered Gaussian white noise, Eqn. 1.4.15 can be captured by noting that the denominator reduces to P and that the numerator is the Fourier transform of $< x(t-\sigma)\, y\big(x(t)\big) >$.

1.5. Evaluating the cable equation

This section provides a brief summary on the equations, as well as the associated numerical methods, used in the simulations of Section 3.

1.5.1. The cable equation

From the principle of conservation of charge, it can be shown that the voltage $V(t)$ of an isopotential cell is governed by

$$c_m \frac{dV}{dt} = -i_m + i_e, \tag{1.5.1}$$

where c_m is the specific capacitance of the membrane, i_m is the sum of membrane currents (per unit area; defined as positive-outward), and i_e is current injected via the electrode into the membrane (per unit area; defined as positive-inward).

Although small neurons (such as the AII) are sometimes assumed to be isopotential on account of their size, care needs to be taken with this interpretation for at least three reasons. First, the attenuation of signals across the cell may depend on the location of input, as spatial propagation can be sensitive to local input impedances and branching (Rall and Rinzel, 1973). Second, the frequency content of signals will influence the extent of propagation, as the passive properties of neurons constitute a spatially-extended low-pass filter (Zador et al., 1995). Third, factors not strictly related to neuronal size or branching (e.g., axial resistivity, conductance densities) influence the propagation of signals in space (Stuart et al., 1999).

Thus, the realistic simulation of neurons may require the membrane potential to be nonuniform in space as well as time. In this case, the longitudinal variation of membrane

potential across the dendrite is modeled. It can be shown (Rall, 1977) that the membrane potential $V(x,t)$ for this dendrite (or "cable") is governed by

$$c_m \frac{\partial V}{\partial t} = (2ar_L)^{-1} \frac{\partial}{\partial x}\left(a^2 \frac{\partial V}{\partial x}\right) - i_m + i_e, \tag{1.5.2}$$

where a is the cross-sectional area of the dendrite and r_L is the longitudinal resistivity. After supplementing this equation with appropriate initial and boundary conditions, the membrane potential of the cell can be evaluated.

1.5.2. Solving the cable equation with finite difference methods

When applied in a realistic setting, the physiology and anatomy of neurons makes the behavior of (1.5.2) typically quite complicated. At a biophysical level, neurons often behave nonlinearly as a result of voltage- and ligand-gated ion channels (captured within the i_m term) (Hodgkin and Huxley, 1952). At a geometrical level, using realistic neuronal morphologies typically requires (1.5.2) to be solved on a highly branched topology with spatially-variable cross-sectional areas. Due to these complications, numerical techniques are commonly used when employing the cable equation to study neuronal dynamics.

One technique that can be used in this respect is to employ a finite difference scheme in both space and time. In this approach, (1.5.2) can discretized according to

$$c_m \left(\frac{V_k^{n+1} - V_k^n}{\Delta t}\right) =$$

$$\frac{a}{2r_L}\frac{1}{\Delta x^2}\left(\alpha(V_{k+1}^{n+1} - 2V_k^{n+1} + V_{k-1}^{n+1}) + (1-\alpha)(V_{k+1}^{n} - 2V_k^{n} + V_{k-1}^{n})\right) - i_m + i_e. \tag{1.5.3}$$

Here, the cross-sectional area a is taken to be constant for simplicity. In Eqn. 1.5.3, different values of α correspond to different integration methods; for example, setting $\alpha = 1/2$ employs the Crank-Nicolson scheme, whereas $\alpha = 1$ uses the Backward Euler scheme. The $\alpha = 0$ case

corresponds to the Forward Euler scheme and is typically not used, as a restrictively small timestep is required for stability when evaluating (1.5.3) with an explicit scheme. The membrane and injected currents i_m and i_e can act as reaction terms and do not need to be integrated with the same method as the diffusive term (indeed, they are often evaluated explicitly).

The particular choice of implicit method (Crank-Nicolson vs. Backward Euler) depends on the precise goal of the simulation, as each implementation has an advantage over the other. On one hand, Crank-Nicolson is more accurate: it is second order in both space and time, whereas Backward Euler is second order in space but only first order in time. On the other hand, Backward Euler is more stable: Crank-Nicolson can produce numerical oscillations for large timesteps, a phenomenon which does not occur in the dissipative Backward Euler scheme.

Finally, although both Backward Euler and Crank-Nicolson methods are implicit schemes, it can be shown that the tree-like morphological structure of neurons allows these equations to be evaluated with $O(N)$ efficiency (where N is the total number of compartments and is independent of branching topology) (Hines, 1984).

1.5.3. Evaluating the cable equation in the NEURON simulation environment

The NEURON simulation environment is a program that provides a simplified approach to studying the behavior of multicompartmental neuronal models (Hines and Carnevale, 1997). In this environment, neuronal morphologies are represented by branched cables and augmented with biophysical properties. NEURON has a variety of integration techniques used to evaluate the equations associated with each cable, including the Backward Euler and Crank-Nicolson methods discussed above. To close the system, these equations are supplemented by two types

of boundary conditions: continuity of voltage is imposed at the sites of coupling between cables, and Neumann boundary conditions are used at the (uncoupled) termini of cables.

1.6. Using models to study the RB-AII microcircuit

In a variety of settings, the pairing of modeling and experimental techniques has provided keen insight into the functionality of the nervous system (e.g., see Jennings and Aamodt, 2000 and associated supplement). Although modeling can provide many distinct advantages when applied closely with experimental data, often one of the primary benefits is the ability to explore all the variables of a simulated system. This allows one to study how the simulated "internal" variables (i.e., those not accessible via experiments) interact with variables that can be measured experimentally. Modeling, when used in a realistic fashion, therefore can provide comprehensive insight into the mechanisms underlying experimental results.

Both the models presented in this thesis illustrate this advantage. In the context of modeling the RB-AII synapse, our computational work enabled a means to study many aspects of vesicle cycling that could not be assessed experimentally. Within the AII model, a critical step to understanding spiking was to be able to investigate the interplay of membrane potential and voltage-gated channels across the extent of the cell membrane; the relatively thin geometry of the AII prevents similar work being tractable in an experimental setting.

The models presented here, which have served to elucidate aspects of the RB-AII microcircuit, will hopefully continue to find use in future experiments and simulations. In their current form, the models are a readily-accessible tool to simulate neuronal behavior and suggest additional lines of inquiry. The models may also be extended to incorporate additional features of the RB pathway, thereby providing an existing foundation for more complex modeling endeavors.

CHAPTER 2

A synaptic mechanism for retinal adaptation to luminance and contrast

2.1. Abstract

The signaling gain in primary sensory circuits is matched to the stimulus intensity by the process of adaptation. In the retina, changes in visual scene statistics induce adaptive mechanisms that adjust sensitivity to mean luminance (background) and temporal variance (contrast). The intrinsic properties of retinal bipolar cells and synapses contribute to background and contrast adaptation, but it is unclear whether both forms of adaptation depend on the same cellular mechanisms. Studies of neurotransmission at bipolar cell synapses identified synaptic mechanisms of gain control, but the relevance of these mechanisms to visual processing is uncertain owing to the historical focus on fast, phasic transmission rather than the tonic transmission evoked by ambient light. Here, we studied use-dependent regulation of bipolar cell synaptic transmission evoked by small, ongoing modulations of membrane potential (V_M) in the physiological range. In collaboration with the Singer Laboratory, we analyze results of paired whole-cell recordings from rod bipolar (RB) and AII amacrine cells, wherein quasi-white noise voltage commands modulated RB V_M and evoked excitatory postsynaptic currents (EPSCs) in the AII. Within these experiments, changes in background luminance or contrast were mimicked, respectively, by depolarizing V_M or increasing its variance. A linear systems analysis of synaptic transmission showed that increasing either the mean or the variance of the presynaptic V_M reduced gain. Further electrophysiological and computational analyses demonstrated that adaptation to mean potential resulted from both Ca channel inactivation and vesicle depletion, whereas adaptation to variance resulted from vesicle depletion alone. Thus, background and contrast adaptation apparently depend in part on a common synaptic mechanism.

2.2. Introduction

Naturally encountered light intensities vary far more than the dynamic ranges of retinal neurons. Consequently, retinal circuits adjust their gains to the statistical features of the visual input; gain controls include 'background adaptation' to changes in mean intensity and 'contrast adaptation' to changes in the variability about the mean (Demb, 2008; Gollisch and Meister, 2010; Shapley, 1997; Shapley and Enroth-Cugell, 1984; Walraven et al., 1990). Both forms of adaptation are apparent in bipolar cell outputs to retinal ganglion and amacrine cells, and both are observed under conditions in which photoreceptors do not adapt and synaptic inhibition is blocked; thus, both forms of adaptation depend, at least in part, on mechanisms intrinsic to bipolar cells and / or their synapses (Beaudoin et al., 2007; Beaudoin et al., 2008; Dunn et al., 2006; Dunn and Rieke, 2008; Kim and Rieke, 2001).

Background adaptation in both rod and cone pathways was absent in bipolar cell voltage responses but present in bipolar cell outputs to postsynaptic neurons, suggesting that adaptation emerges in the process of synaptic transmission (Dunn et al., 2006; Dunn et al., 2007; Dunn and Rieke, 2008). Adaptation to contrast, however, may involve a different mechanism: contrast adaptation in salamander bipolar cell responses was apparent following integration of photoreceptor inputs (Rieke, 2001), although an additional component of contrast adaptation was implemented at the synaptic output to ganglion cells (Baccus and Meister, 2002; Kim and Rieke, 2001).

Biophysical studies of bipolar cell synapses suggested that two presynaptic mechanisms may influence adaptation of bipolar cell output: vesicle depletion and Ca channel inactivation (Mennerick and Matthews, 1996; Singer and Diamond, 2006; von Gersdorff and Matthews,

1996, 1997). Because these studies focused on phasic transmission from otherwise quiescent synapses, it is difficult to extend their results to tonically active synapses operating in a narrow physiological voltage range (~10-20 mV). Furthermore, these studies offer no insight into whether background and contrast adaptation might depend at least in part on a common mechanism.

Here, we investigated synaptic mechanisms for background and contrast adaptation with physiologically realistic presynaptic stimulation of the mouse RB-AII synapse. Transmission at this synapse can be assessed readily (Jarsky et al., 2010; Tian et al., 2010) and this synapse is a known site of retinal gain control (Dunn et al., 2006; Dunn and Rieke, 2008). In collaboration with the Singer Laboratory, we report experimental results that demonstrate synaptic gain is reduced by increasing the mean or variance of the RB V_M. Adaptation to the mean depended on both vesicle depletion and Ca channel inactivation, whereas adaptation to variance depended on vesicle depletion alone. Thus, the background and contrast adaptation observed in retinal responses to light depend in part on a common mechanism arising from the intrinsic dynamics of transmission at bipolar cell synapses.

2.3. Methods

Here, methods are included for both the LN modeling and computational modeling; the associated experimental methods can be found in the corresponding manuscript (Jarsky et al., 2011). All experimental recordings were performed by members of the Singer Laboratory: Tim Jarsky conducted paired recordings (with the exception of Figure 2.11; Jiangbin Ke) and Stephen Logan performed single recordings. The LN modeling (with the exception of Fig. 2.6A-D) and computational modeling were performed by the author.

2.3.1. Linear-nonlinear cascade analysis

We used a linear-nonlinear (LN) cascade analysis to describe the transfer function at the RB-AII synapse. The LN analysis is a modification of the Wiener kernel analysis applied to linear systems (Marmarelis and Naka, 1973; Wiener, 1949). Neural systems are inherently nonlinear, and therefore classical systems analysis typically requires the extraction of high-order kernels (or 'filters') to describe the transformation from stimulus to response. Such calculations are complex and lack an intuitive relationship to underlying cellular processes, but the analysis can be simplified by including a static nonlinearity that scales the system response predicted by the first-order Wiener kernel by the intrinsic nonlinearities of the component neurons (Chichilnisky, 2001). Our analysis is conceptually similar to the LN analysis applied routinely to describe the transfer function between light stimuli and intracellular or firing responses in retinal neurons (Baccus and Meister, 2002; Chichilnisky, 2001; Kim and Rieke, 2001; Zaghloul et al., 2003).

Here, we analyze the results of paired voltage-clamp recordings from synaptically-coupled

RBs and AIIs. Within these recordings, conducted by the Singer Laboratory, the 'stimulus' was a quasi-white noise voltage command applied to the presynaptic RB: Gaussian white noise limited to a 0-250 Hz bandwidth. The 'response' was the postsynaptic current in the AII. The presynaptic voltage command bandwidth was limited to avoid complicating analysis of the synaptic filter with electrotonic filtering by the RB axon, which acts as a low-pass filter with a minimum cut-off frequency of ~300 Hz (Oltedal et al., 2009). Synaptic release can follow signals in the 0-250 Hz range because of the fast kinetics of the presynaptic Ca channels (see Fig. 2.6B, C) and the dynamics of the release machinery (Singer et al., 2004). Stimuli were presented during 12 s trials that were separated by at least 20 s. The time between trials allowed data to be written to the computer hard drive and permitted the recording of stable synaptic responses for at least several minutes. Each trial consisted of repeated and unique stimuli. The unique stimuli were different on each trial and were used to construct the LN model; whereas the repeated stimuli were used to test the model's prediction (see Fig. 2.3B).

The linear filter F was taken to be the cross-correlation of the response with the stimulus. In principle, the band-limited nature of the stimulus can be compensated for by dividing this cross-correlation with the stimulus autocorrelation in the frequency domain. However, we found that fluctuations present in the stimulus power spectrum tended to corrupt the linear filter and reduce the predictive power of the LN model. Thus, we elected to generate F via the response-stimulus cross-correlation only. All analyses were performed in MATLAB (Mathworks; Natick, MA).

In theory, the filter should be non-zero only for positive time points. However, the measured filter typically showed a peak negative response at +2-3 ms with 'ripples' extending on either side of the peak, including non-zero values at negative time points. Further analysis

suggested that the measured filter shape reflected a fast underlying filter whose shape was affected by the 0-250 Hz bandwidth of the analysis (Fig. 2.3). We found that the underlying filter could be modeled as a delayed difference-of-exponentials (DOE) function, $d(t)$, that is zero up to a short delay (t_d) and then described as follows:

$$d(t+t_d) = \kappa_1 \exp(-t/\sigma_1) - \kappa_2 \exp(-t/\sigma_2), \tag{2.1}$$

where each exponential has an amplitude (κ_1 and κ_2) and a time constant (σ_1 and σ_2). When the DOE function was limited to the 0-250 Hz bandwidth of the analysis, it closely approximated the measured filter, including the ripples that extend to negative time points (see Fig. 2.3C). Thus, the measured filter apparently represented a band-limited version of an underlying filter that was too fast to measure with high accuracy. In the analysis that follows, we used the measured filter between t = -25 and +75 msec.

A linear prediction of the synaptic response, $r_L(t)$, was generated by convolving the filter with the stimulus:

$$r_L(t) = \int F(\tau) s(t-\tau) d\tau. \tag{2.2}$$

This linear prediction was plotted against the measured response, at each time point, to generate the static nonlinearity of the synapse, which typically showed inward rectification. We binned the data along the x-axis (200 bins) and fit the data with a smooth curve:

$$f(x) = \alpha C(\beta x + \gamma) + \delta, \tag{2.3}$$

where C is the cumulative Gaussian; that is, $C(a) = (1 + \mathrm{erf}\,(a/\sqrt{2}))/2$. The parameters inherent to this fit corresponded to a maximum response (α), response gain (β), response threshold (γ) and an offset (δ) (Chander and Chichilnisky, 2001; Zaghloul et al., 2005). This nonlinear (N) function served as the "input-output" relationship that transformed the L prediction

into the LN prediction (r_{LN}):

$$r_{LN}(t) = N[r_L(t)]. \quad (2.4)$$

We used the LN description to compare the effect of changing either the mean (-51 vs. -45 ± 3 mV) or the standard deviation (SD) (-48 ± 1.5 vs. 4.5 mV) of the RB command potential. To make this comparison, we generated an individual filter for each condition, and then fit the two nonlinearities simultaneously with three shared parameters (α, γ, δ) and one unique parameter for each N function (β_1 and β_2). The two N functions then could be aligned by 'stretching' one along the x-axis by the factor β_1/β_2 (Chander and Chichilnisky, 2001; Zaghloul et al., 2005). To maintain a constant output of the LN model, the filter had to be scaled by the same factor. Thus, the change between two conditions could be described as a difference in the filter amplitudes followed by a common N function. In one case (comparing conditions with different means), we subtracted a vertical offset in the N function before performing the alignment procedure so that the two nonlinearities were matched at $f(x=0)$. In this case, we could interpret the offset (i.e., tonic inward current at x=0) as an unmodulated increase in release independent of the modulated release.

To quantify the predictive ability of the LN model, we computed the squared correlation (r^2) between the LN prediction and the average response to the repeated stimulus (5-8 trials for each paired recording). In all cases, r^2 likely underestimates the model's predictive power, because noise remained after averaging ~5-8 responses. This was particularly evident in the most depolarized (V_M = -45 ± 3 mV; see Figs. 2.4 and 2.10c*iv*) and lowest SD (V_M = -48 ± 1.5 mV; see Figs. 2.5 and 2.10e*iv*) conditions. To derive a quantitative measure of the noise, we divided the repeated responses recorded in each cell into two groups and calculated the r^2 between the averages of each group (i.e., we sought to determine how well each response represented the

group). In all cases the correlation between the LN prediction and the averaged response was very close to the correlation between the averages of different subsets (model vs. subsets; r^2 = mean ± SD): in the case of changing the mean RB command potential, the r^2 was 0.68 ± 0.06 vs. 0.70 ± 0.16 for -51 mV and 0.12 ± 0.14 vs. 0.20 ± 0.16 for -45 mV. In the case of changing the SD of the RB command potential, the r^2 was 0.68 ± 0.09 vs 0.72 ± 0.17 for SD = 4.5 mV and 0.14 ± 0.08 vs 0.11 ± 0.08 for SD = 1.5 mV.

Given the noise arising from tonic exocytosis (i.e., uncorrelated release) under some experimental conditions (see Fig. 2.4D), we believe that the LN model performs as well as can be expected of any model. Its predictive ability would be improved, and it could be tested more rigorously, were larger data sets available. Because the Singer Laboratory could not obtain paired recordings lasting long enough to create larger data sets for individual RB-AII pairs, we approximated such sets by pooling the data from individual paired recordings. We did this by grouping all experimental recordings into one ensemble set and analyzing the pooled data in the same way as individual pairs: the linear filters and nonlinearities were extracted after concatenating all of the unique responses recorded, and the LN prediction was compared to the responses to repeated stimuli averaged across all recorded pairs. After doing this, the predictive power of the model was enhanced considerably, as expected: (individual vs. pooled; r^2 = mean): in the case of changing the mean RB command potential, the r^2 was 0.68 vs. 0.86 for -51 mV and 0.12 vs. 0.72 for -45 mV. In the case of changing the SD of the RB command potential, the r^2 was 0.68 vs 0.88 for SD = 4.5 mV and 0.14 vs. 0.70 for SD = 1.5 mV. Thus, we conclude that the transfer function at the RB-AII synapse is well-described by our LN model.

2.3.2. Model of synapse

Transmission at the RB-AII synapse was modeled by tracking the cycling of a presynaptic readily-release pool (RRP) in response to altered presynaptic potential. The RRP was the mean number N of vesicles that were available for release at any point in time [maximum size N_{MAX} = 80 vesicles (Jarsky et al., 2010; Oltedal and Hartveit, 2010; Singer and Diamond, 2006; Zhou et al., 2006)]. Its evolution was modeled by a differential equation as

$$\frac{dN}{dt} = -r(V(t))N(t) + \alpha(N_\infty(h) - N(t)). \tag{2.5}$$

The first term described the mean rate of exocytosis, with $r(V(t))$ being the rate of release as a function of the command voltage $V(t)$ (illustrated in Figs. 2.1-2.2). The second term captured the recycling of vesicles back into the RRP, with the recycling rate given by α and the effective size of the RRP given by $N_\infty(h)$.

The release rate $r(V(t))$ depended both on the varying instantaneous voltage and on the time-averaged voltage:

$$r(V(t)) = r_V(V) + r_U. \tag{2.6}$$

$r_V(V)$ captured the rapid modulation of release by fluctuations in the presynaptic stimulus [i.e., rapid changes in the number of open channels at each active zone (AZ)], and r_U described release that depended on the mean voltage only (reflecting the mean number of open channels at each AZ and perhaps processes like slow changes in intraterminal [Ca^{2+}]). This scheme reflects the finding that the opening of individual Ca channels controls exocytosis from RB AZs (Jarsky et al., 2010).

The voltage dependence of $r_V(V)$ was described as the sigmoid:

$$r_V(V) = A\,h\,(1 + \exp\,(-(V - V_{1/2})/k)^{-1}. \quad (2.7)$$

$V_{1/2}$ and k were chosen to yield a curve that resembled the G-V relationship of the presynaptic Ca conductance, h captured Ca channel inactivation, and A was a fit parameter chosen to provide good agreement between instantaneous voltage and release. Again, this description relies on the observed close coupling between Ca channels and release sites at the RB AZ. A and k were constants (equal to 0.3 msec^{-1} and 2.25 mV, respectively), but $V_{1/2}$ and h varied with the mean membrane potential to approximate depolarization-induced modulation of Ca currents: namely, shifts of the activation curve to higher voltages and increases in the extent of inactivation. The evolution of $V_{1/2}$ and h were described as follows:

$$\tau_{1/2}\,dV_{1/2}/dt \;=\; V_{1/2\infty} - V_{1/2}, \quad (2.8)$$

$$\tau_h dh/dt \;= h_\infty - h, \quad (2.9)$$

The time constants of $\tau_h = \tau_{v_{1/2}}$ = 400 ms and were derived from recorded Ca currents (Jarsky et al., 2011). Based on recorded Ca currents (Jarsky et al., 2011), $V_{1/2\infty}$ was made a piece-wise linear function of the mean membrane potential (Table 2.1). From Ca current recordings and from changes in release rate assessed by the quasi-white noise experiments, we assigned h_∞ (see Table 2.1). $V_{1/2}$ and h were initialized at their respective steady-state levels at V = -60 mV (the RB's holding potential).

Uncorrelated release was described as:

$$r_U = B(V_{Mean})\,h, \quad (2.10)$$

with $B(V_{Mean})$ given in Table 2.1. With the exception of $B(-42)$, these values were determined empirically to approximate experimentally-observed tonic inward currents during

hyperpolarizing white noise stimuli. It should be noted that $B(-42)$ and $h_\infty(-42)$ could not be constrained by the quasi-white noise experiments (e.g., see Fig. 2.10) because only voltage-step experiments (see Fig. 2.11) were performed at this potential. Thus, these parameters are relatively unconstrained. B and h_∞, however, were used only for the RRP simulation (see Fig. 2.10C-E), and over a range of parameters our simulations fell within 1 SD of the experimental data.

Because individual release sites are controlled by the openings of individual Ca channels (Jarsky et al., 2010), vesicles near inactivated Ca channels are not likely to undergo exocytosis, effectively reducing the RRP. Therefore, we took the effective size of the RRP to be $N_\infty = h\,N_{Max}$. Recycling of vesicles into the available pool occurred with a time constant α^{-1}= 130 ms to approximate the steady-state rate of exocytosis that follows complete release of the RRP (Singer and Diamond, 2006).

The EPSC was determined by convolving the mean number of vesicles released in unit time $r(V(t))N(t)$ with the experimentally-measured mEPSC waveform (Jarsky et al., 2010). The mEPSC waveform was modeled as a difference of exponentials with a τ_{Fast} = 0.4 and τ_{Slow} = 0.54 and a peak amplitude of -25 pA. Additionally, the variability of release occurring experimentally was captured by convolving the released vesicles with a Gaussian distribution of mean = 1.5 ms and SD = 0.5 ms, with negative values set to zero and the Gaussian renormalized to have an area equal to one.

Table 2.1. Parameter values for various mean potentials (mV)

	V_{Mean} <= 54	V_{Mean} = -51	V_{Mean} = -48	V_{Mean} = -45	V_{Mean} = -42
$V_{1/2\infty}(V_{Mean})$	-41	-39.5	-38	-36.5	-35
$h_{\infty}(V_{Mean})$	1	1	0.87	0.48	0.18
$B(V_{Mean})$	0	0	0.003	0.055	0.25

To compare the model to the experiment, we grouped all experimental recordings into one ensemble set and analyzed the pooled data in the same way that individual pairs were analyzed, as described above for the LN analysis.

We took care to constrain the model parameters by experimental measurements to avoid over-fitting. The only parameters used in the white noise experiments that were not strongly constrained by experimental data were those associated with the sigmoid function describing r_V: A, k, and baseline $V_{1/2\infty}$ (i.e., $V_{1/2\infty}$ for mean V <=-54mV). To assign values to these variables, r_V first was fit by eye to produce simulations consistent with experiments. Afterwards, a least-squares fitting procedure (constructed by using the *fminsearch* unconstrained nonlinear optimization tool from Matlab) was used to verify that the chosen values for the free parameters approximated the optimal ones by minimizing the error associated with the repeated -51 ± 3 mV and -48 ± 4.5 mV stimuli (for which experimentally-recorded responses were relatively noiseless). Over a wide range of initial values for A, k, and $V_{1/2_\infty}$, *fminsearch* tended to converge on values very close to those used in the illustrated simulations. The specific values used in these simulations were chosen because they generally agreed well with all protocols simultaneously, including the voltage step experiments and the white noise experiments using a command voltage of -48 ± 3 mV (Figs. 2.10,2.11).

Unless indicated otherwise, all values below are presented as mean +/- standard error of the mean (SEM).

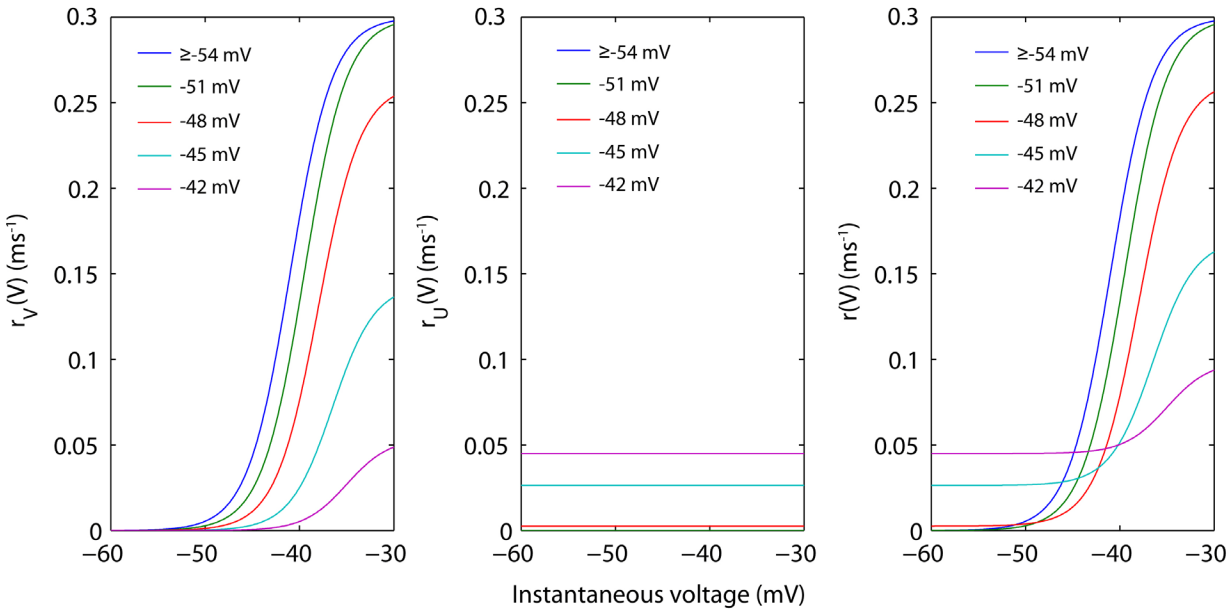

Figure 2.1. Release curves used in the synapse model.
Release rates r_V (left; steady-state), r_U (middle), and $r = r_V + r_U$ (right) are illustrated, in msec, as a function of instantaneous voltage. Individual curves correspond to different mean potentials, given within the legend.

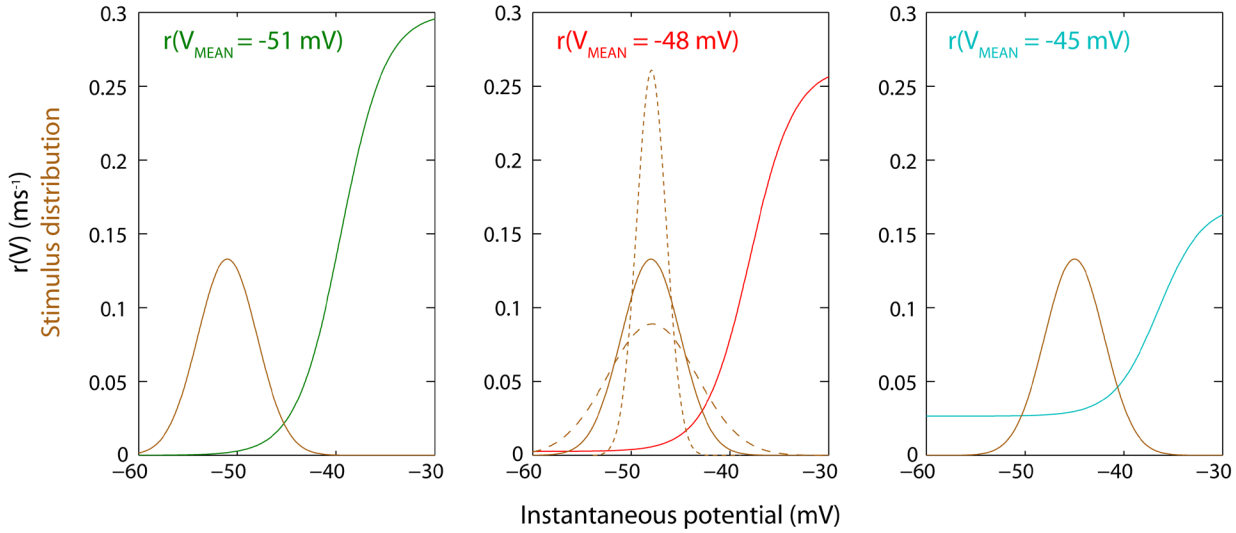

Figure 2.2. Release curves used in white noise simulations. The release curves used in white noise simulations from Fig. 2.1 are illustrated individually. For comparison, release curves are displayed along with normal distributions (gold) corresponding to the respective stimuli used in white noise simulations and experiments. Left and right: distributions are given for a 3 mV SD. Middle: stimulus distributions are given for a 1.5 mV (fine dashed line), 3 mV (filled), and 4.5 mV (coarse dashed line) SD.

2.4. Results

2.4.1. A linear-nonlinear model describes the RB-AII synaptic transfer function

First, we sought to implement a transfer function for the RB-AII synapse so that we could quantify presynaptic membrane potential-dependent changes in synaptic gain. To do this, we applied a linear-nonlinear (LN) cascade analysis to synaptic transfer (see Sect. 2.3.1). This approach has a number of advantages over the more conventional analysis. First, the LN analysis uses a stimulus that spans a wide range of temporal frequencies so that any temporal filtering by the synapse can be characterized and compared between conditions. Second, the LN analysis characterizes the full input-output function of the synapse because the stimulus spanning a wide range of presynaptic V_M. Whereas estimating synaptic gain from a single test pulse can yield divergent estimates of the gain change depending on the degree of nonlinearity at the synapse, we can use the LN analysis to measure accurately a gain change between two conditions by characterizing the full synaptic transfer function (Fig. 2.3A). Furthermore, the LN analysis used here is identical to the analysis used to characterize gain changes during visual stimulation of retinal neurons. Thus, the LN analysis facilitates comparison between our study of a bipolar synapse and many previous studies of light-dependent changes in response gain (Chichilnisky, 2001; Demb and von Gersdorff, 2008; Wang et al., 2011).

First, we used data where the RB was stimulated with a randomly fluctuating voltage command of -48 ± 3 mV (mean ± SD; Gaussian white noise with 0-250 Hz bandwidth; see Sect. 2.3.1) to modulate the presynaptic Ca current, in turn modulating exocytosis that gave rise to EPSCs recorded in the AII. We generated a linear filter by cross-correlating the presynaptic voltage command and the evoked postsynaptic current (Fig. 2.3B; see Sect. 2.3.1). Convolving

the measured filter with the bipolar cell voltage command created the linear prediction of the postsynaptic response, which was plotted against the recorded postsynaptic currents to generate the nonlinear component of the synaptic transfer function. Data were binned and fit with a smooth function (Fig. 2.3B; see Sect. 2.3.1). This nonlinearity captures the strong inward rectification of the synapse: the release rate can be increased substantially by depolarizing the presynaptic membrane, but the release rate cannot be decreased below zero.

In this LN analysis, the linear filter reflects the frequency response of the synapse. The filters we calculated showed negative peaks at ~2-3 ms, reflecting the brief synaptic delay. Further, we observed minor 'ripples' on either side of the peaks, and additional analysis revealed that the shape of the measured filters resulted from the limited bandwidth of the stimulus (0-250 Hz; see Sect. 2.3.1): a fast filter, such as a delayed difference of exponentials (DOE), yielded a filter time course that, when limited by the 250-Hz cut-off, resembled closely the measured filters (Fig. 2.3C). This finding suggested that the true biophysical linear filter likely resembles a difference of exponentials for frequencies up to 250 Hz. Because our analysis is limited by the stimulus bandwidth (0-250 Hz), the true underlying filter (e.g., a DOE) and the measured filter will yield the same linear prediction (because their frequency components are identical across the 0-250 Hz bandwidth; see Sect. 2.3.1). The implications of the filter shape are discussed later in more detail.

Scaling the linear prediction by the nonlinearity generated a predicted output (the LN prediction). As illustrated in Fig. 2.3B, the LN prediction corresponded well to the recorded data. We assessed the predictive power of the LN model by comparing the LN prediction to the averaged response to a repeated stimulus (4 – 11 repeats to reduce noise). The LN model explained 57% of the variance in the averaged response ($r^2 = 0.57 \pm 0.07$; n = 5 recorded pairs).

The r^2 value underestimates the predictive value of the LN model when it is applied to individual paired recordings because the number of repeats was limited by the recording duration; the LN prediction's fit to the data was enhanced considerably after pooling data from all recorded cell pairs in a given condition (see Sect. 2.3.2). On a single trial, the EPSCs reflect a combination of exocytosis modulated by the presynaptic voltage command and tonic un-modulated exocytosis (i.e., uncorrelated release). The total response in a given condition, then, represents a ratio between these two components of release. Conditions that decreased the ratio between modulated and uncorrelated release degraded the r^2 value calculated for individual cell paired recordings; however, the r^2 values increased considerably (to 0.7 – 0.9; see Sect. 2.3.2) when predicting the response averaged across cell pairs. Thus, the LN model could be used under experimental conditions with relatively low signal-to-noise.

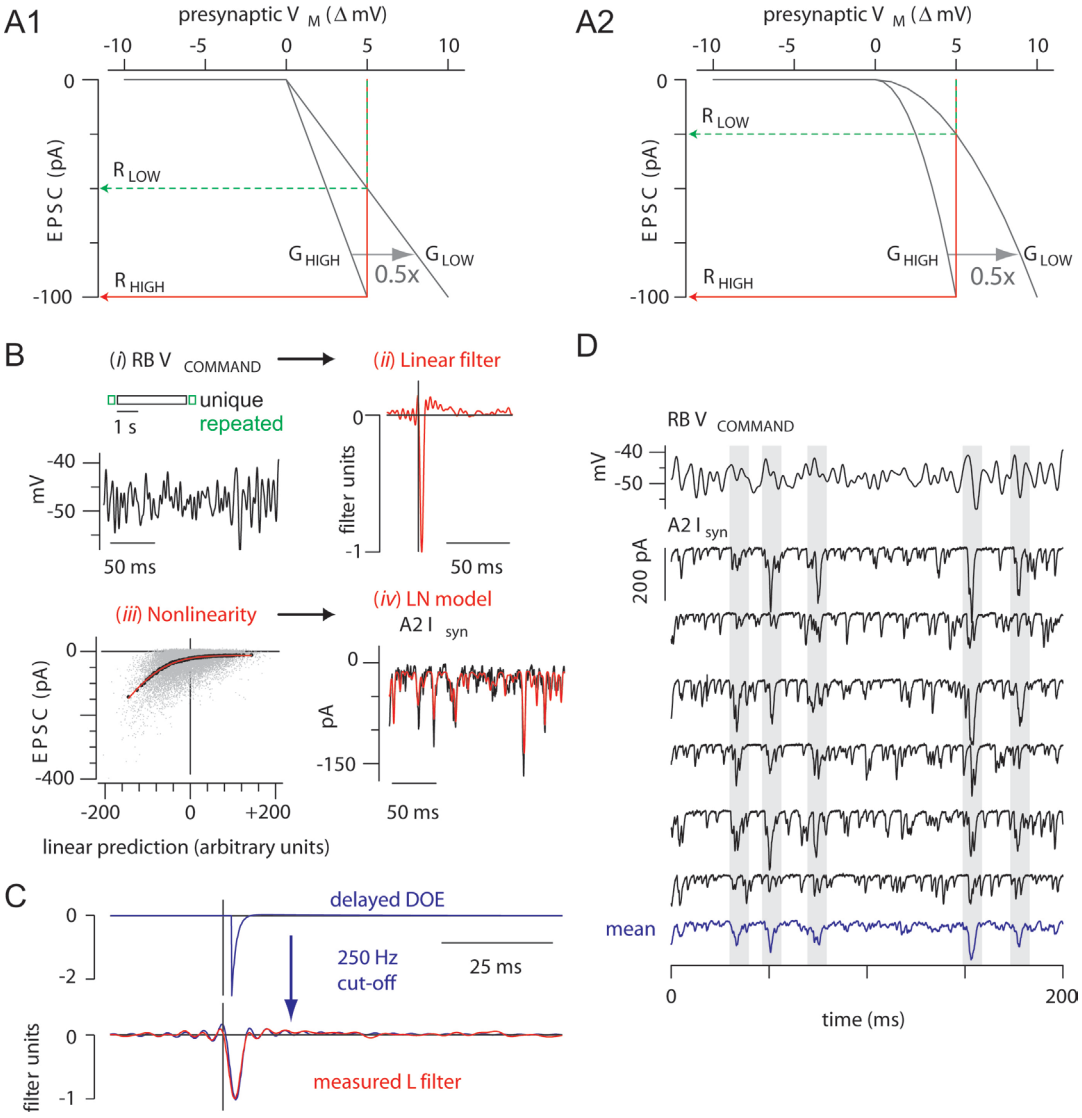

Figure 2.3. Linear-nonlinear model for characterizing the RB-AII synapse

A. Schematic representation of the synaptic transfer function between presynaptic membrane potential and postsynaptic current. In both cases, synapse is partially rectifying (zero for potentials negative to rest) and otherwise linear (left) or nonlinear (right). Both a high-gain (G_{HIGH}) and low-gain (G_{LOW}) condition are shown; gain in the G_{LOW} condition was scaled by 0.5 (i.e., ordinate values are plotted against abscissa values multiplied by 2). Response to a +5 mV test pulse from baseline (0 mV) in the low-gain (R_{LOW}) and high-gain (R_{HIGH}) conditions are shown. Measuring gain by the ratio R_{LOW}/R_{HIGH} yields a correct 0.5 change in the linear case (A1) but an incorrect 0.25 change in the nonlinear case (A2); measuring the complete input-output function using the LN analysis enables a scaling procedure to reveal the correct gain change in both cases (see Sect. 2.3.1). B. The RB was stimulated with a voltage-command (48 ± 3 mV) that included both repeated sequences (350 ms) and a unique sequence (4 s). A single trial is represented schematically, and a representative sample of the repeated stimulus is illustrated blow. Trials were separated by 20 s. The LN model was generated from the unique sequences and tested on the repeat sequences (i). The unique response is convolved with a linear filter (ii) to generate a linear prediction of the AII output (given in arbitrary units). This prediction is passed through a static nonlinearity (iii), characterized by strong inward rectification, to generate the LN model of AII output. The predicted LN output (iv) resembles the measured synaptic current (AII I_{syn}; averaged across six repeats; $r^2 = 0.57 \pm 0.07$ for n=5 recorded pairs). The nonlinearity shows the raw data (gray points, downsampled to 1 kHz), the binned data (black points, 200 bins), and the fit compared with the averaged response to the repeated stimulus filter (red line). C. The measured filter is approximated by a delayed DOE after applying a 250 Hz cutoff (fitted parameters: $t_d = 2.0$ ms; $\kappa_1 = 2.6$; $\sigma_1 = 1.0$ ms; $\kappa_2 = 0.05$; $\sigma_2 = 26.6$ ms). The entire LN analysis was restricted to frequencies <250 Hz, and the measured filter was used to generate the linear prediction in B. D. Six responses to the repeated stimulus are shown to illustrate the variability of the synaptic responses. This variability gives rise to the scatter evident in the raw data (gray points) binned to generate the nonlinearity in B. The gray bars highlight responses to relatively large depolarizations, these are reproduced with considerable variability from trial to trial.

2.4.2. Synaptic gain is altered by changes in the statistics of presynaptic membrane potential

Changes in the local statistics in a visual scene alter the stimulus-response relationships of retinal neurons (Dunn and Rieke, 2006). Consequently, we wished to determine how the transfer function of the RB-AII synapse varied with the mean and variance of the presynaptic membrane potential. To do this, we used the LN model to quantify the effect of changing RB V_M on the gain of synaptic transmission.

First, we analyzed data from the Singer Laboratory when the mean V_M was modulated (SD = 3 mV) about means of -51 and -45 mV. These mean potentials represent the approximate RB V_M at backgrounds of 1 and 30 R*/rod/sec, respectively (Jarsky et al., 2011). Both conditions showed similar linear filters and rectifying nonlinearities, although the synaptic output of the RB was strongly suppressed at the depolarized mean potential (Fig. 2.4A, B: insets, and Fig. 2.4C). Additionally, a negative vertical shift (-5.5 ± 2.4 pA; mean ± SEM; n = 5) in the zero-crossing point of the nonlinearity was observed following depolarization (Fig. 2.4B, C). This -5.5 pA is the average amplitude of a tonic inward current arising from a small burst of delayed exocytosis that began ~100 ms following the membrane depolarization to -45 mV and that decayed with a time constant of ~1.3 s. This delayed exocytosis, which was not present at -51 mV, is likely equivalent to the uncorrelated release that has been described in an earlier study of this synapse (Singer and Diamond, 2003). Delayed exocytosis was not modulated by the quasi-white noise stimulus, and its presence did not alter our ability to estimate the synaptic transfer function with LN analysis. Consequently, the difference in the zero-crossing point was subtracted from the nonlinearity before further analysis (Fig. 2.4B; see Sect. 2.3.1).

The suppression of RB output reflects a reduction in synaptic gain. We quantified the gain change by fitting the two nonlinearities with a function that included a scaling factor. Altering the scaling factor “compressed” the nonlinearity for the depolarized condition along the

x-axis. This compression reflects a change in the linear prediction and therefore must be accompanied by an identical scaling of the linear filter's amplitude (to keep the LN model's output constant; see Sect. 2.3.1). Following the scaling procedure (Fig. 2.4C), the nonlinearity was identical in the two conditions, and the gain change was reflected by the ratio of filter amplitudes. On average, the gain in the depolarized condition was 32 ± 4% (mean ± SEM; n = 5) of the gain in the hyperpolarized condition: i.e., the 6-mV depolarization reduced gain of synaptic transmission by ~68%.

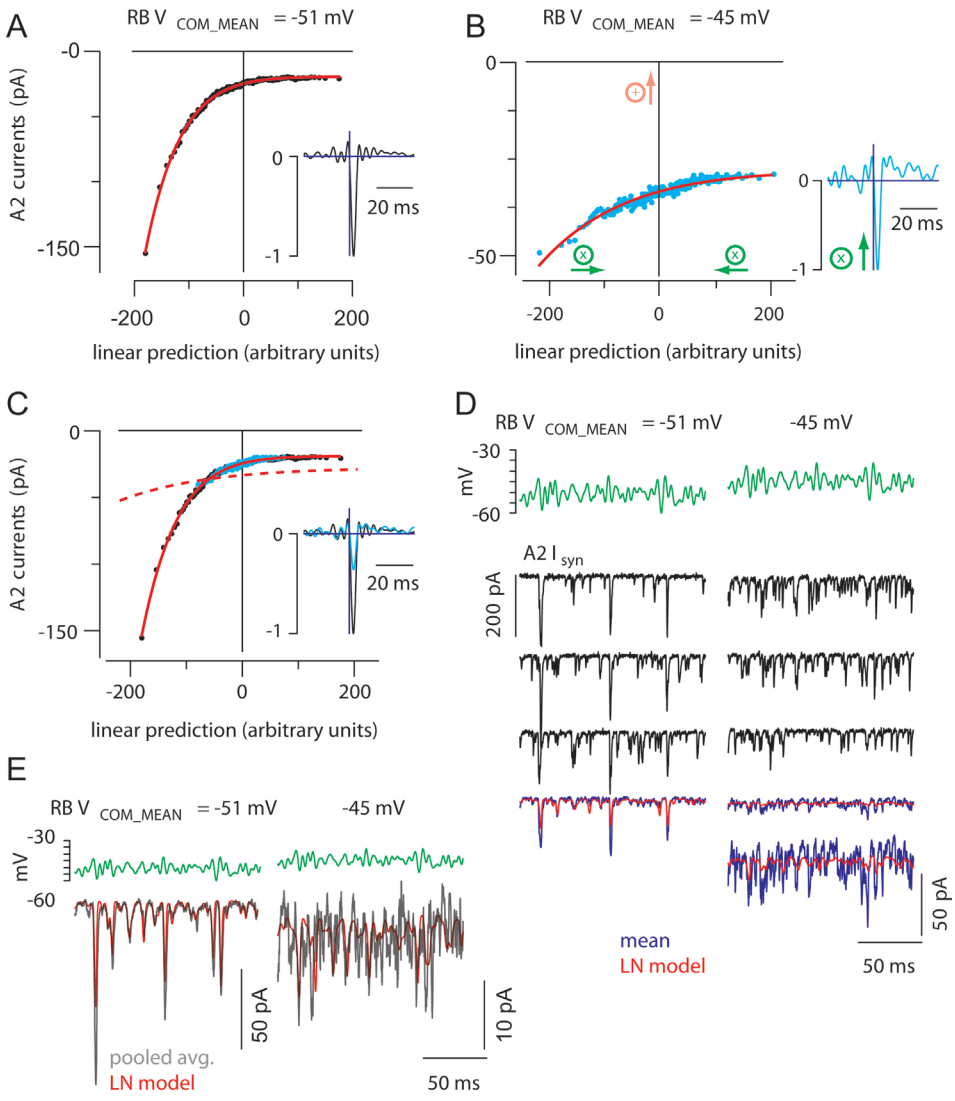

Figure 2.4. Depolarizing the rod bipolar cell membrane potential reduced synaptic gain
A,B. The static nonlinearity and linear filter (insets) are shown for conditions in which the mean rod bipolar command potential (V_{com_mean}) was either -51 (A) or -45 mV (B); in both cases, the SD of the white noise input was 3 mV. The nonlinearities were fit (red line) simultaneously by allowing a scale factor to different between conditions. C. The nonlinearity of the depolarized mean condition could be aligned with the nonlinearity of the hyperpolarized mean condition by adding a constant (9.3 pA for the this recording and 5.5 ± 2.4 pA for n=5 paired recordings; B, orange arrow) and scaling the x-axis (by 0.36 for this recording and 0.32 ± 0.04 for n=5 paired recordings; B, green arrows). To maintain a constant LN model output, the filter was multiplied by the same scaling factor (inset). Depolarizing the RB reduced output gain to 36% of the gain in the hyperpolarized condition (32 ± 4% for the population of n=5 paired recordings). The red dashed line shows the unscaled fit in the depolarized condition in B. Depolarizing the RB reduced synaptic gain. D. Three responses to repeated stimuli with means of -51 mV (left) and -45 (right) illustrate the variability inherent in the data. The LN prediction is better correlated with the averaged response at -51 mV than with the averaged response at -45 mV because of the increased amount of uncorrelated release at depolarized potentials as well as the reduction in the size of the responses correlated with the stimulus. The average response in the -45 mV condition is shown both at the same scale as the -51 mV condition and on an expanded time scale. E. Pooling data from n=5 recorded pairs improves the predictive power of the LN model. Gray trace, response to repeated stimulus average across all recorded pairs; red trace, LN prediction derived from model constructed with pooled data. r^2 = 0.86 and 0.72 for -51 and -45 mV, respectively.

Next, we quantified the effects of changing the temporal variance of the RB voltage on synaptic gain. In collaboration with the Singer Laboratory, we obtained data and analyzed two quasi-white noise stimuli with the same mean (-48 mV) but different standard deviations (1.5 or 4.5 mV) (Fig. 2.5). Increasing the SD did not alter significantly the zero-crossing of the nonlinearity (difference of -0.58 ± 0.71 pA; mean ± SEM, n=5), suggesting that increased SD was not accompanied by an increase in asynchronous release. Increasing the SD, however,

reduced the gain of synaptic transmission to 82 ± 1% of the gain in the low SD condition (mean ± SEM, n = 4; one outlier removed. 87 ± 10% with outlier included) (Fig. 2.5C). Thus, tripling the SD of the RB V_M reduced the gain of synaptic transmission by ~18%.

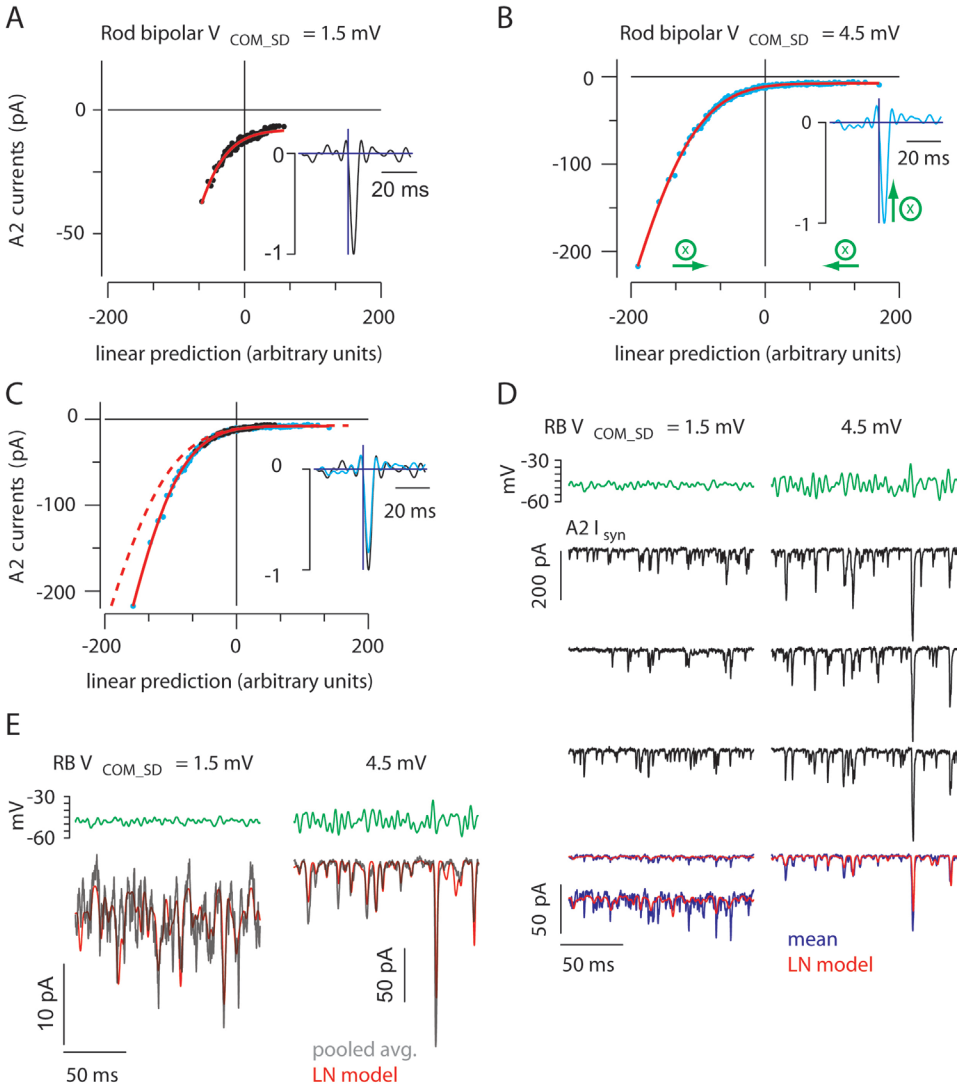

Figure 2.5. Increasing SD of the rod bipolar cell membrane potential reduces synaptic gain
A,B. The static nonlinearity and linear filter (insets) are shown for conditions in which the mean RB command potential was -48 mV, and the SD of the command potential (V_{com_SD}) was either 1.5 (A) or 4.5 mV (B). The nonlinearities were fit (red line) simultaneously by allowing a scale factor to differ between conditions. C. The nonliearity of the high SD condition could be aligned with the nonliearity of the low SD condition by scaling the x-axis (by 0.83; B, green arrows). To maintain a constant LN model output, the filter is multiplied by the same scaling factor (inset). Increasing the SD of the rod bipolar reduced output gain to 83% of the gain in the low SD condition. The red dashed line shows the unscaled fit in the high SD condition in B. D. Three responses to repeated stimuli with SD of 1.5 mV (left) and 4.5 mV (right) illustrate the variability inherent in the data. The LN prediction is better correlated with the averaged response when the modulated voltage is larger (i.e., when the proportion of release events correlated with the stimulus is higher). The average response in the low SD condition is shown both at the same scale as the high SD condition and on an expanded scale. E. Pooling data from n=5 recorded pairs improves the predictive power of the LN model. Gray trace, response to repeated stimulus averaged across all recorded pairs; red trace, LN prediction derived from model constructed with pooled data. r^2 = 0.70 and 0.88 for SD of 1.5 and 4.5 mV, respectively.

2.4.3. Biophysical basis of the LN model

The close correspondence between the predictions of the LN model (which does not identify explicitly any biological mechanisms) and the phenomenological model (which reproduces the recorded data with only a few parameters) allows us to describe the cellular mechanisms that dominate the transfer function of the RB-AII synapse. In the LN analysis, the linear filter can resemble the system's impulse response provided that the diagonal components of all higher-order kernels are sufficiently small. We found that the linear filter was consistent with a filtered, delayed DOE (Fig. 2.3C). In previous studies of this synapse, the Singer Laboratory has evoked large, fast EPSCs in an AII using a Ca tail current in the presynaptic RB,

which approximates an impulse response (e.g., Singer 2003, Jarsky, 2010). Though fast, these EPSCs are slower than the DOE probably owing to the asynchrony inherent in the release process (Fig. 2.6A). The DOE, however, resembles the time course of a quantal miniature EPSC: the postsynaptic response to a single vesicle. Thus, the temporal filtering at this synapse reflects the time required to transform a change in synaptic glutamate concentration into a postsynaptic conductance change. The slightly biphasic shape of the DOE suggests that the release process shows attenuated sensitivity to low temporal frequencies.

To examine the biophysical basis for the delay of the DOE, the LN analysis was used to study the transfer between RB membrane potential and the Cd^{2+}-sensitive Ca^{2+} current evoked by modulating the RB command potential (-48 ± 3 mV) (Fig. 2.6B). The RB-AII synapse followed stimulation at high frequencies suggesting that the RB Ca channels that control exocytosis have high temporal resolution. The linear filter derived from the stimulus and response showed a peak at 0.8 ms with 'ripples' on either side peak (Fig. 2.6C). Further, the liner filter resembled very strongly the delayed autocorrelation of the stimulus, indicating that, when limited by the 0-250 Hz bandwidth of the stimulus and analysis, the transformation from presynaptic voltage to presynaptic Ca^{2+} influx is well-represented as a 0.8 ms delay. Thus, the total delay reflected in the linear filter describing synaptic transfer combines Ca channel activation (~0.8 ms; Fig. 2.6B) and the synaptic delay following Ca^{2+} entry into the presynaptic terminal [~ 1.5 ms; Fig. 2.6A; see (Jarsky et al., 2010)].

The nonlinear stage between RB voltage and Ca^{2+} current was nearly linear over the voltage range tested (-58 to -38 mV; Fig. 2.6D). To compare this nonlinearity to the current-voltage (I-V) relationship of synaptic release, we generated a second LN model of the synapse. The delayed DOE approximation of the linear filter, in the standard analysis above, showed that

the filter at the synapse is very fast and that filtering in the 0-250 Hz range is minimal. The filter was therefore approximated as a simple Dirac delta function shifted 2-3 ms time (matching the peak of the standard filter measured by cross-correlation; see Sect. 2.3.1). In this case, the nonlinearity plots the time-shifted RB command potential versus the postsynaptic current, yielding a current-voltage (I-V) relationship for the synapse; the predictive ability of this model ($r^2 = 0.55 \pm 0.06$; prediction vs. data; n = 5 recorded pairs) was nearly the same as the standard model ($r^2 = 0.57 \pm 0.07$). The synapse's I-V relationship is clearly more strongly rectifying than the Ca current's measured over the same voltage range (Fig. 2.6D, E).

We conclude that multiple mechanisms likely underlie the nonlinearity at the RB synapse derived from our analysis. Though we cannot assess the individual contributions of the many nonlinear processes involved in synaptic transmission (e.g., the Ca^{2+}-dependence of exocytosis), we can exclude the voltage-dependence of Ca channel opening as accounting for the nonlinearity. The fact that the nonlinearities at the synapse maintain their shapes when the synaptic gain changes dramatically (Fig. 2.4, 2.5) indicates that the gain change occurs before the nonlinearity. In other words, because nonlinearities recorded in two conditions can be scaled to overlie each other, the cellular processes underlying the nonlinearity are not altered by the gain change. To a first approximation, this excludes changes to highly nonlinear processes (e.g., the Ca^{2+}-dependent steps in exocytosis) from participating in the gain change and supports our assertion that a reduction in the number of release sites available to participate in exocytosis, arising from a diminution in the number of available vesicles and Ca channels, lowers synaptic gain.

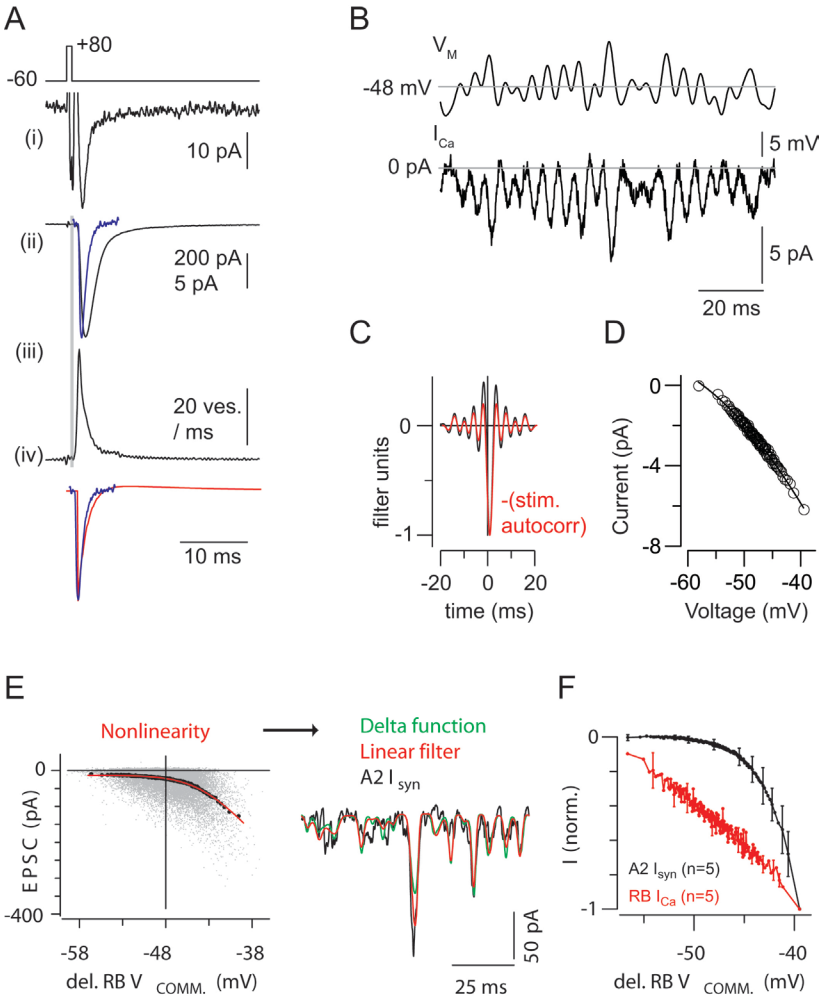

Figure 2.6. Biophysical basis of the LN model

A. A Ca tail current (i) evoked by a 1 ms step from -60 to +80 mV evokes a large, fast EPSC (ii, black trace) that is slower than a quantal miniature EPSC (ii, blue trace) because of the asynchrony inherent in the release process. The extended time course of release is illustrated by deconvolving the miniature EPSC from the evoked response (iii). The gray area highlights the synaptic delay. The waveform of the quantal miniature EPSC (blue) resembles strongly the DOE (black) approximating the true linear filter of the synapse (iv). B. The Ca current elicited by the quasi-white noise stimulus. C. The linear filter exhibits a delay of ~0.8 ms because of the time required for channel activation (black). In red, the autocorrelation of the stimulus, shifted by + 0.8 ms. D. For the recording illustrated, the relationship between Ca current (delayed by 0.8 ms) was relatively linear. E. The linear prediction is generated by convolving the stimulus with a delayed Dirac delta function, in effect time-shirting (delaying) the stimulus by a constant value. The nonlinearity is represented as a function of the delayed stimulus, and the predicted output generate here (green) is almost identical with that derived from the conventional LN analysis (B) (red; $r^2 = 0.55 \pm 0.06$; n = 5 recorded pairs). F. A comparison of the Ca current and postsynaptic current nonlinearities averaged from n = 5 recordings in each case. Error bars are ± SD.

2.4.4. Modeling the RB-AII synapse

Consolidating the previous results, release from RBs adapts to changes in both the mean and the standard deviation of the RB command voltage. To gain insight into the mechanisms underlying these two types of adaptation, we constructed a computational model of the RB-AII synapse and sought to recapitulate the experimental data.

Here, we will focus on illustrating the refinement of the model in order to capture the gain change found when varying mean V_M. We choose to illustrate the development of the model in this set of experiments, rather than when varying the SD, for the following reason. When using realistic rates for recycling, the simulated gain change within the latter set of

experiments was captured simply by vesicle depletion and was robust over a wide range of other parameters. Accordingly, capturing these data did not require extensive refinement of the model. Conversely, capturing the gain change arising from varying mean V_M required several biophysically-motivated extensions to a model solely incorporating depletion. These refinements have generated model predictions that have since been verified experimentally and have clarified the encoding properties of the RB-AII synapse.

To describe the evolution of the model, we will begin with a model incorporating only depletion and present models that successively increase in complexity; for each version, we illustrate how it fails to capture experimental data until we arrive at a model that is successful. In presenting the model in this way, we wish to illustrate not only the ability of the final model to recapitulate the experimental results, but to also rule out other simpler mechanisms underlying adaptation at the RB-AII synapse.

2.4.5. A model incorporating only depletion fails to capture the experimental gain change

First, we constructed a model that incorporated only depletion; that is, $h_\infty = 1$ and $B = 0$ for all mean V_M (see Sect. 2.3.2: Equations 2.9, 2.10 and Table 2.1). Over a range of parameters inherent to the release rate $r(V)$, such that $r(V)$ approximated presynaptic Ca currents, experimental data could not be reproduced. For example, neither the averaged responses to repeated stimuli (Fig. 2.7A) nor the nonlinearity (Fig. 2.7B) could be recapitulated. This failure of the model occurred due to the steepness of $r(V)$ emerging at potentials beyond -45 mV (Fig. 2.7): if the pool was not sufficiently depleted at -45 mV, this steepness caused release to be strongly driven at more depolarized potentials. This produced inward currents for large depolarizations that were similar between V_M = -51 mV and V_M = -45 mV (e.g., Fig. 2.7B). This

feature was never observed in experiments (c.f. Fig. 2.4). Of course, these pronounced currents could be reduced by defining $r(V)$ such that the RRP was almost completely depleted at V_M = -45 mV, and therefore typically unable to follow further depolarizations. However, this manipulation would cause the nonlinearity at V_M = -51 mV to saturate for large negative linear predictions. Again, this was a property never observed in experimental data (c.f. Fig. 2.5).

As it appeared that a model with a homogeneous vesicle pool and a fixed recycling rate was unable to capture the observed gain change, we next examined whether a pure depletion mechanism was supported by experimental data. We hypothesized that if depletion could completely mediate the gain change observed experimentally while employing a single homogeneous pool and fixed recycling rate, it would be necessary that release at V_M = -45 mV would greatly exceed release at V_M = -51 mV in order to deplete the available pool.

Upon examining the experimental recordings, we found that release at -45 mV exhibited a profound asynchronous component: following the initial voltage step, a slow mode of release was observed that peaked ~0.5 sec after the step and subsequently decayed with a timescale of ~1.3 sec (Fig. 2.7C; see Sect. 2.3.2). To examine whether this release mode was driven by white noise stimuli, we partitioned the unique white noise sequences into ~0.8 sec long segments and performed an LN analysis on the initial and terminal segments. This analysis revealed that although asynchronous release decayed between these two segments, the shape of the nonlinearity remained similar (i.e., only the vertical offset was changed; Fig. 2.7D). Thus, this asynchronous mode of release seemed to be uncorrelated with the stimulus, and instead increased overall release for transiently following the initial voltage step.

As calculating the gain change at the RB-AII synapse involved removing the vertical offset between nonlinearities at high and low V_M (see Sect. 2.3.1), this release mode did not

contribute to the gain change. Consequently, we opted to construct a model that captured experimental release at steady-state by restricting comparisons to the last ~1 sec of experimental data only (comprising ~0.8 s of unique stimuli and ~0.3 s of repeated stimuli). Within the context of our model, therefore, the surge of asynchronous release was viewed as release from a secondary pool that superposed on normal, RRP-mediated release. We did not attempt to investigate this asynchronous release mode further either through modeling or experiments.

Notably, for this terminal subset of data, the total amount of release was actually greater at V_M = -51 mV than at V_M = -45 mV (ratio of charge transfers, -51 V_M / -45 V_M = 1.2 ± 0.2). Despite less release at the depolarized potential, the gain change from this subset of data was similar to that found in the full response (Fig. 2.7C), indicating that depletion was not the sole mechanism underlying the gain change. As this finding was consistent with the results from our model, we were next motivated to extend this model to capture the experimentally-observed reduction in release at mean V_M = -45 mV.

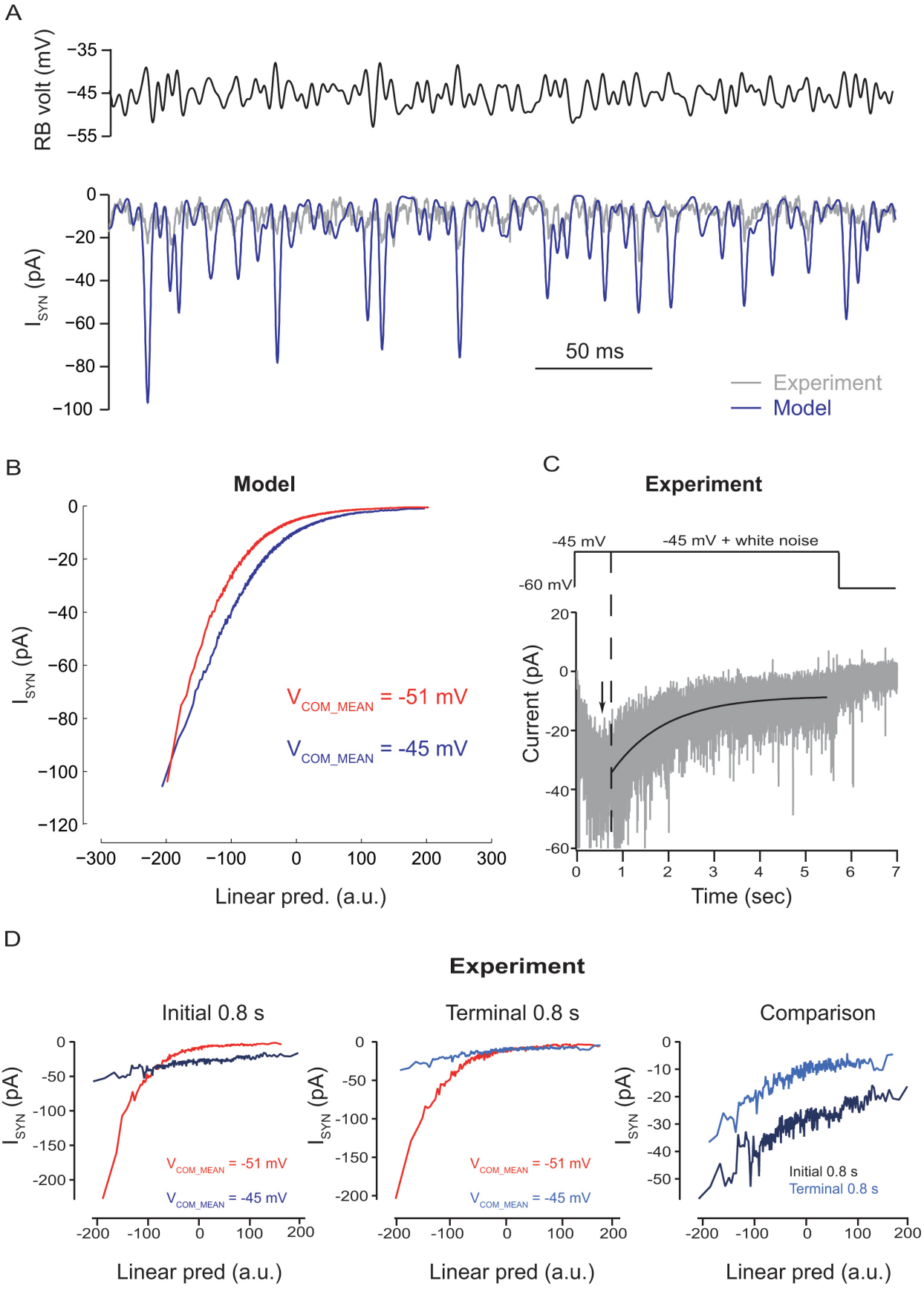
A
RB volt (mV)
−35
−45
−55
0
−20
−40
−60
−80
−100
I_SYN (pA)
50 ms
Experiment
Model
B
Model
I_SYN (pA)
V_COM_MEAN = -51 mV
V_COM_MEAN = -45 mV
Linear pred. (a.u.)
C
Experiment
-45 mV
-45 mV + white noise
-60 mV
Current (pA)
Time (sec)
D
Experiment
Initial 0.8 s
Terminal 0.8 s
Comparison
I_SYN (pA)
V_COM_MEAN = -51 mV
V_COM_MEAN = -45 mV
Initial 0.8 s
Terminal 0.8 s
Linear pred (a.u.)

Figure 2.7. Depletion cannot account for the experimentally-observed gain change.
A. Averaged responses are illustrated in response to repeated stimuli (top, black), both in experiments (bottom, grey) as well as for a model incorporating depletion (bottom, blue). Model responses were much larger than that seen experimentally. B. Example nonlinearities from a model incorporating depletion. The structure of the nonlinearity at the depolarized mean potential was comparable to that at the hyperpolarized mean potential, deviating from experimental results. C. Release at -45 mV showed an asynchronous component that peaked ~0.5 sec after the initiation step, and decayed with an exponential timescale of ~1.3 sec. The grey trace is an average across all pairs and all realizations of white noise; each realization began ~0.8 sec after the initial voltage step (dotted black line). D. Nonlinearities are shown for the first (left) and last (middle) ~0.8 sec of white noise for one pair. The nonlinearity at the hyperpolarized potential remained relatively fixed, whereas the nonlinearity at the depolarized potential showed an offset of ~20 pA without a change in the overall structure (right).

2.4.6. A model incorporating depletion and Ca inactivation fails to capture the experimental gain change

The previous version of the model would not be expected to produce less release at mean V_M = -45 mV than mean V_M = -51 mV, as switching from mean V_M = -51 mV to mean V_M = -45mV increased release rates while the recycling rate remained fixed. We therefore sought to extend our model to capture the reduction in release. In order to inform our model, we first sought to identify a biophysical mechanism that could produce this effect.

Recycling rates are generally believed to increase with increased intracellular Ca concentrations (Babai et al., 2010; Singer and Diamond, 2006), which in turn increase with depolarization. Thus, it is unlikely that a decrease in recycling rate would mediate the reduction in release seen in experimental recordings.

As an alternative, a reduction in overall release might emerge from the recycling rate remaining fixed while the release rate itself decreases. A potential candidate for this would be Ca inactivation. We observed inactivation to be pronounced at -45 mV but almost entirely absent at -51 mV (Jarsky et al., 2011), in agreement with the voltage range where release was reduced. This inactivation might restrict exocytosis by potentially operating in two different ways: first, inactivation might reduce Ca influx at active zones and lower release probability; second, inactivation might affect all Ca channels at an active zone, effectively reducing the size of the RRP by making any associated vesicles unavailable for exocytosis.

To implement an inactivation-like reduction in release within the synapse model, we extended the previous model by reducing the total size of the RRP and the probability of release equally by a factor h at -45 mV (see Sect. 2.3.2: Equation 2.9 and Table 2.1). This factor was chosen to produce the ratio of release between -51 and -45 mV seen experimentally, and was implemented in a time-dependent fashion to mimic the effects of Ca inactivation following the initial voltage step.

Incorporating this feature into the model was effective in limiting the overall currents (Fig. 2.8A) and increasing the corresponding gain change (Fig. 2.8B), as expected. Importantly, provided that the total amount of release at mean V_M = -45 mV was adjusted to produce the correct ratio of release relative to mean V_M = -51 mV seen experimentally, adjusting either the size of the RRP or the release probability alone also produced almost identical nonlinearities (Fig. 2.8C). Thus, our particular choice of scaling the RRP and the release probability equally by h was not critical for capturing experimental data.

Despite this improvement after incorporating Ca inactivation-like effects, two features of the model still profoundly differed from experimental data (Fig. 2.8D). First, despite being

reduced, model currents at large negative linear predictions were still markedly larger than experimental currents. Second, release was almost completely absent for large positive linear predictions. Indeed, incorporating Ca inactivation served to slightly exacerbate this problem from the previous model (Figs. 2.8A,B) and emphasized an important shortcoming of this version: although the gain change seen experimentally could be captured by overemphasizing the role of inactivation (that is, by making h smaller still), this would only serve to make the model output deviate further from experimental results for large positive linear predictions. Thus, we were motivated to next extend our model to increase tonic release.

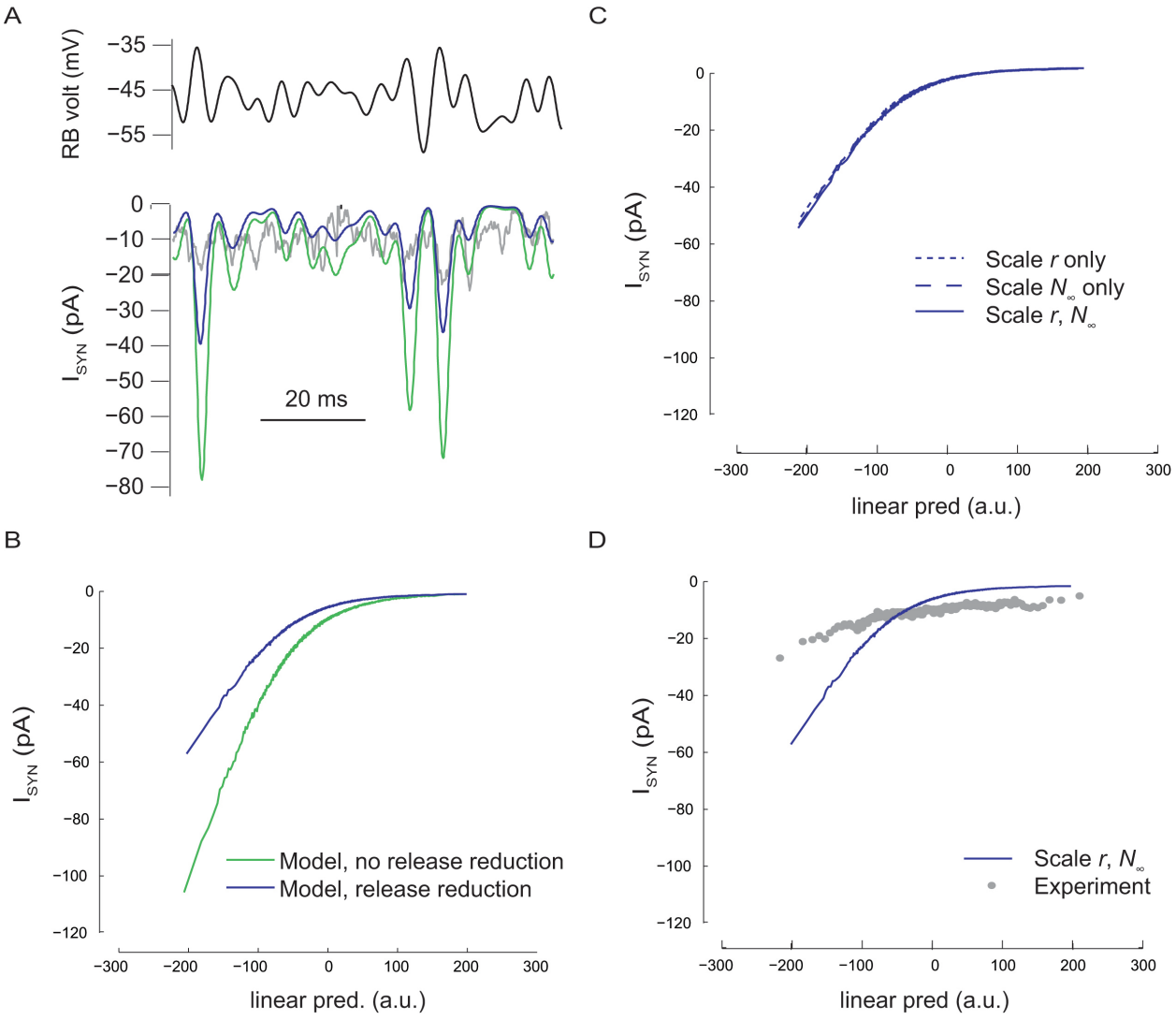
A
RB volt (mV)
−35
−45
−55
0
−10
−20
−30
−40
−50
−60
−70
−80
I_SYN (pA)
20 ms
B
I_SYN (pA)
0
−20
−40
−60
−80
−100
−120
−300
−200
−100
0
100
200
300
linear pred. (a.u.)
Model, no release reduction
Model, release reduction
C
I_SYN (pA)
0
−20
−40
−60
−80
−100
−120
−300
−200
−100
0
100
200
300
linear pred (a.u.)
Scale r only
Scale N∞ only
Scale r, N∞
D
I_SYN (pA)
0
−20
−40
−60
−80
−100
−120
−300
−200
−100
0
100
200
300
linear pred (a.u.)
Scale r, N∞
Experiment

Figure 2.8. Reducing release through Ca inactivation improves gain change, but does not capture experimental data. A. Responses are illustrated for averaged experimental data (grey), as well as for versions of the synapse model without (green) and with (blue) reductions in release. B. Example nonlinearities from a model incorporating only depletion (green) and a model incorporating both depletion and reduced release (blue). C. When the total release was restricted to the ratio observed in experiments, similar nonlinearities emerged whether either the release rate or size of the RRP were scaled individually (fine or coarse dashed lines, respectively) or adjusted equally (filled line). At this scale, responses almost completely overlay. D. The nonlinearity extracted from this model exhibited too much release for large negative projections and too little release for large positive projections.

2.4.7. A model incorporating depletion, Ca inactivation, and uncorrelated release captures the experimental gain change

In the previous version of the model, release at large positive linear predictions for V_M = -45 mV failed to capture the prominent tonic release seen in experiments. As the release rate in this prior model was determined solely by the instantaneous membrane potential, this might suggest that release in an experimental setting becomes progressively uncorrelated with increasing mean depolarizations. This hypothesis is consistent with the pronounced Ca channel inactivation occurring between mean V_M = -51 and mean V_M = -45 mV: L-type Ca channels typically undergo Ca-induced Ca inactivation (Imredy and Yue, 1994), and the finding that inactivation sets in sharply within this voltage range is suggestive of elevated terminal Ca at depolarized potentials (Jarsky et al., 2011). This in turn may indicate that release, which is driven by terminal Ca concentration, may be influenced more by residual terminal Ca than by influx through voltage-gated Ca channels at mean V_M = -45 mV.

To capture this uncorrelated release within the computational model, we introduced a term B that drove release solely according to the mean voltage only; that is, release that was uncorrelated with the white noise modulation (see Sect. 2.3.2: Equation 2.10 and Table.2.1). The value of this term was adjusted to match the tonic release seen at large positive linear predictions. Interestingly, after incorporating this release term and readjusting the amount of release to match the ratio of release at mean V_M = -51 vs. V_M = -45, model currents improved (Fig. 2.9A) and the nonlinearity emerging from the model matched the experimentally-obtained nonlinearity across the entire range of linear predictions (Fig. 2.9B). This behavior emerged due to the tonic release limiting the total size of the available pool; thus, large presynaptic voltage excursions produced less release when uncorrelated release was included.

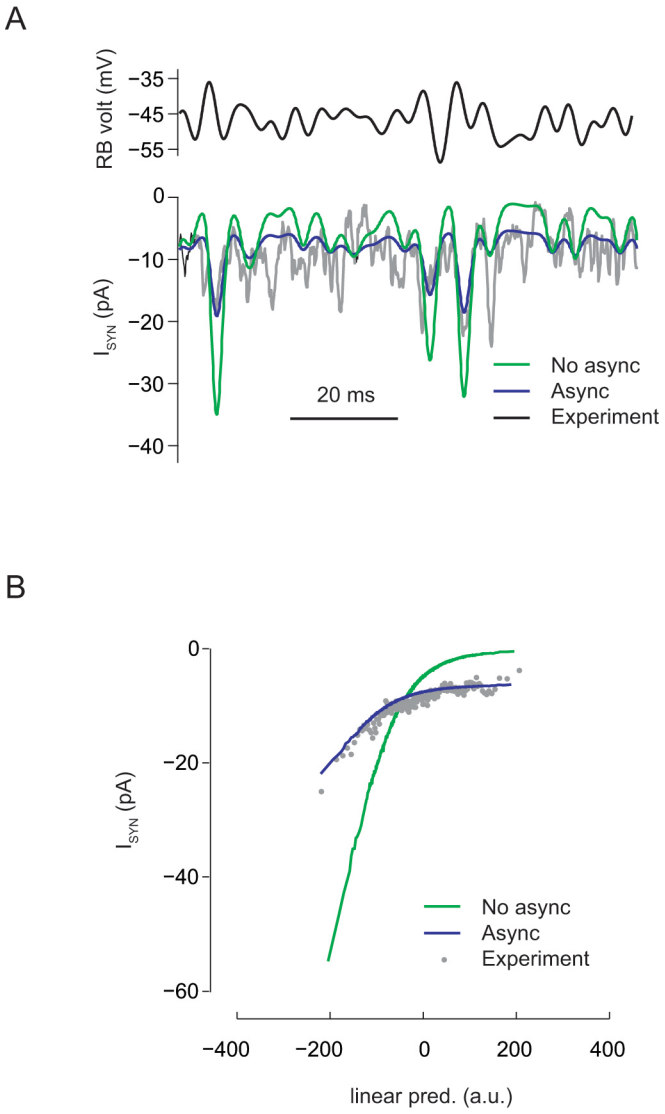

Figure 2.9. The experimental nonlinearity is captured by a model containing depletion, reduction of release, and uncorrelated release.

A. Responses are illustrated for the previous version of the synapse model (green), as well as after uncorrelated release is incorporated (blue). Experimental data is overlaid in grey. B. Adding uncorrelated release to the previous model served to both reduce currents for large positive linear predictions and increase currents for large negative current injections, which produced a model nonlinearity consistent with experimental results.

At this potential, the value of the uncorrelated release term ($r_U = 0.026$ ms^{-1}) was found to be almost an order of magnitude greater than the correlated release term ($r_V = 0.0032$ ms^{-1} at steady state when $V = -45$ mV). This suggested that, in order to recapitulate the experimental data, release needed to be almost entirely uncorrelated with the white noise stimulus at mean V_M = -45 mV; this finding was striking considering that the experimental data at mean V_M = -51 mV could be captured well without requiring any uncorrelated release. Thus, a prediction that emerged from this model was that the RB-AII synapse transitions from correlated to almost completely uncorrelated release over a narrow 6 mV voltage range, a point to which we return to later.

2.4.8. The synapse model captures experimental responses to white noise protocols

Having illustrate the refinement of the synapse model in order to capture the nonlinearity at mean V_M = -45 mV, we next demonstrate the ability of the final version of the model to capture the three experimental protocols; namely, the initial recordings involving -48 ± 3 SD, as well as the experiments where either the mean or variance was altered.

First, we simulated the response to steady-state depolarization to -48 ± 3 SD. As illustrated by Figure 2.10, the model generated a prediction that matched quite closely the experimental data (assessed by comparing the model to the response averaged across RB-AII pairs; r^2 = 0.93). Subjecting the simulated postsynaptic current to the LN analysis generated a linear filter and a static nonlinearity almost identical to those arising from recorded postsynaptic currents (Fig. 2.10B).

Next, we simulated responses to stimuli in which either the mean or variance was altered (e.g., Fig. 2.4 and 2.5). Again, the model was able to reproduce accurately the postsynaptic

current recorded in response to these stimuli (r^2 = 0.94 and 0.53 for the hyperpolarized and depolarized mean V_M experiments; r^2 = 0.92 and 0.70 for the high- and low SD experiments) (Fig. 2.10C, E). The static nonlinearities calculated from these simulated data sets strongly resembled those derived from experiments (Fig. 2.5D, F). Scaling these nonlinearities (e.g., Figs. 2.4 and 2.5; see Sect. 2.3.1) allowed us to quantify the gain changes arising from each manipulation of the stimulus. Gain was reduced by 64% by depolarizing the mean from -51 to -45 mV, and it was reduced by 15% by increasing the stimulus SD from 1.5 to 4.5 mV (compared to 68% and 18% for the experimental responses to the same manipulations).

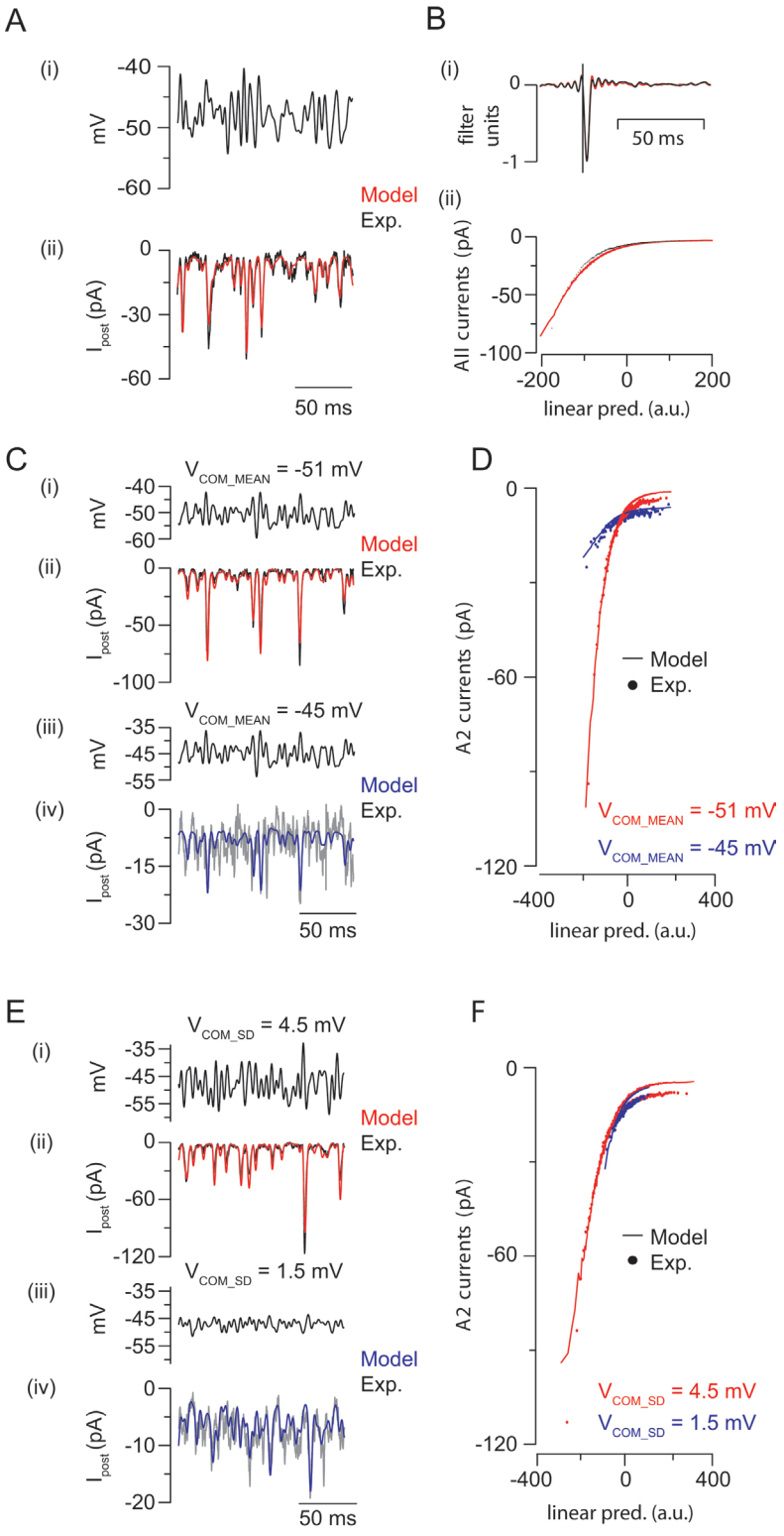
A
(i)
mV
-40
-50
-60
Model
Exp.
(ii)
I_{post} (pA)
0
-30
-60
50 ms
B
(i)
filter units
0
-1
50 ms
(ii)
All currents (pA)
0
-50
-100
-200
0
200
linear pred. (a.u.)
C
(i)
V_{COM_MEAN} = -51 mV
mV
-40
-50
-60
Model
Exp.
(ii)
I_{post} (pA)
0
-50
-100
(iii)
V_{COM_MEAN} = -45 mV
mV
-35
-45
-55
Model
Exp.
(iv)
I_{post} (pA)
0
-15
-30
50 ms
D
A2 currents (pA)
0
-60
-120
Model
Exp.
V_{COM_MEAN} = -51 mV
V_{COM_MEAN} = -45 mV
-400
0
400
linear pred. (a.u.)
E
(i)
V_{COM_SD} = 4.5 mV
mV
-35
-45
-55
Model
Exp.
(ii)
I_{post} (pA)
0
-60
-120
(iii)
V_{COM_SD} = 1.5 mV
mV
-35
-45
-55
Model
Exp.
(iv)
I_{post} (pA)
0
-10
-20
50 ms
F
A2 currents (pA)
0
-60
-120
Model
Exp.
V_{COM_SD} = 4.5 mV
V_{COM_SD} = 1.5 mV
-400
0
400
linear pred. (a.u.)

Figure 2.10. A phenomenological model of the RB-AII synapse
A. A presynaptic voltage command (top) is applied to the model to generate a simulated synaptic response (red trace, bottom). The simulated response (red) resembles the experimentally observed postsynaptic response to the same presynaptic stimulus (black; response averaged from n = 5 recorded RB-AII pairs). B. The linear filter (i) and static nonlinearity (ii) extracted from LN analysis of the simulated output of the synapse (red) matches closely the linear filter and static nonlinearity describing the experimentally measured input-output relationship (black). C,E. The phenomenological model of the RB-AII synapse reproduces experimentally-observed adaptation to stimulus mean and variance. Stimuli (I,iii) and responses (ii,iv) (black, experiment; red and blue, model) for each condition are illustrated. Experimental responses are averages from n = 5 paired recordings for each condition. D,F. Static nonlinearities derived for experimental (dots) and simulated (lines) conditions. Increasing stimulus mean from -51 to -45 mV reduced gain by 63%; raising stimulus SD from 1.5 to 4.5 mV reduced gain by 15%. For simplicity, the scaled nonlinearities are not illustrated (see Sect. 2.3.1).

We wished to assess the accuracy with which the model predicted the size of the cycling RRP. To do this, we compared model output to release evoked experimentally (in collaboration with the Singer Laboratory) with a 5 ms step to -10 mV [sufficient to elicit release of the entire RRP (Jarsky et al., 2010; Singer and Diamond, 2006)] following 700 ms prepulses to potentials between -60 and -42 mV (Fig. 2.11A). With increasingly depolarizing prepulses, the quantal content of the evoked EPSC was reduced substantially (to approximately 20% of control; Fig. 2.11C). It is notable that the cell-pair to cell-pair variability in the EPSCs elicited following the depolarized prepulses was large, and the recording illustrated in Fig. 2.11B showed the least depression (note the error bars in Fig. 2.11F). Significantly, RRP was not depleted completely by this stimulus: vesicles were available after 700 ms of sustained release to encode additional depolarization. The model reproduced accurately the recorded EPSCs (Fig. 2.11D-F). Notably,

the model's initial responses were transient in nature even though they did not reflect the release of the entire RRP. Rather, the postsynaptic response decayed rapidly after vesicle release was initiated because the rate of vesicle replenishment is much slower than that of exocytosis. This observation suggests that the transient nature of transmission at the RB – AII synapse arises from the dynamics of vesicle recycling, i.e., EPSCs always exhibit a transient component, even when the RRP has not been depleted completely; see (Snellman et al., 2009). It is worth noting that in this respect, EPSCs recorded from mouse AIIs at physiological temperatures differ from those recorded in rat AIIs at room temperature [see (Singer and Diamond, 2003)].

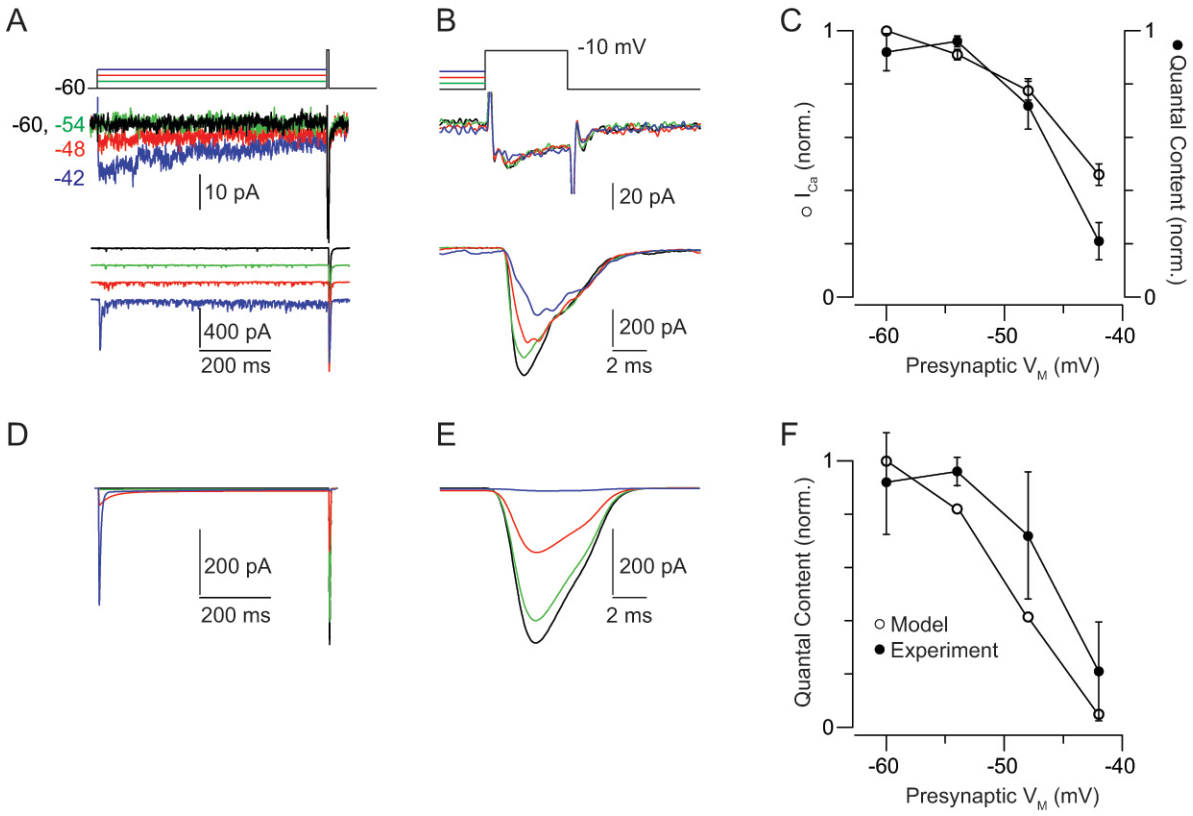

Figure 2.11. The RRP at the RB-AII synapse is reduced by tonic presynaptic depolarization
A. The presynaptic RB is stepped to prepulse potentials between -60 and -42 mV for 700 ms before a 5ms step to -10 mV. Presynaptic Ca currents (middle) and evoked EPSCs (bottom) are illustrated. EPSCs have been separated by a vertical offset. B. Ca currents and EPSCs are illustrated at higher temporal resolution. EPSCs are not offset. C. Summary of n = 7 experiments. Ca currents (integrated) and EPSCs (quantal contents) recorded during the test pulse from each RB-AII pair were normalized to the largest currents recorded in that pair. D. Simulated synaptic currents generated by our phenomenological model (stimulus as in A). The inset illustrates a small, steady-state component of release at depolarized potentials. E. Simulated responses to depolarization to -10 mV at higher temporal resolution. F. Comparison of the output of the model to the experimentally measured responses. Here, the error bars on the experimental data points are ± SD.

2.4.9. The synapse model correctly predicts the rapid transition from correlated to uncorrelated release

Within the synapse model, a critical feature to capture the gain change in the vary mean V_M protocol was the incorporation of uncorrelated release. Incorporating this extension at mean V_M = -45 mV caused the model to exhibit a relatively flat nonlinearity, while simultaneously not restricting the total amount of release to unphysiologically low levels. However, the amount of uncorrelated release required to recapitulate the experimental data was striking: the model predicted a transition from completely correlated release at mean V_M = -51 mV to almost completely uncorrelated release at mean V_M = -45 mV. As the previous white noise experiments were limited in the total amount of data (only four repeats per pair after excluding the initial surge of release), we sought to investigate this model prediction through further experiments.

To this end, paired RB-AII voltage-clamp recordings were performed by the Singer Laboratory with the aim of examining the reproducibility of release as a function of mean

potential (Fig. 2.12). For a given pair, the presynaptic RB was stimulated with twenty repeats of a brief (~250 ms) white noise waveform (SD = 6 mV); this was performed as a single trial at three mean membrane potentials (Fig. 2.12A,C; each pair tested at either V_M = -57/-51/-45 mV or -54/-48/-42 mV). In order to avoid contributions from the asynchronous surge of release seen in the previous experiments, the first repeated stimulus occurred ~2 sec after the initial voltage step (Fig. 2.12A,C).

To assess the reproducibility of release, the postsynaptic responses at a given mean potential were partitioned into two distinct sets (odd vs. even repeats) and each set was averaged. The R^2 value was then calculated between the two averaged sets of data. It was found that the experimental data showed a sharp transition from reproducibility at mean V_M = -51 mV to nearly random release at mean V_M = -45 mV (Fig. 2.12E; R^2 changed from 0.82 ± 0.02 at mean V_M = -51 mV to = 0.01 ± 0.01 at mean V_M = -45 mV; n=5); this rapid drop in reliability occurred across the voltage range that was predicted by the synapse model. On either side of this voltage neighborhood, the R^2 value remained relatively fixed (R^2 for other mean V_M: 0.88 ± 0.04 / 0.79 ± 0.10, 0.51 ± 0.12 / 0.01 ± 0.01/ 0.02 ± 0.01 for mean V_M = -57 / -54 / -48 / -42 mV; n=5 for mean V_M = -57 mV, n=6 otherwise). Importantly, this finding underscored the ability of the synapse model to generalize, as it captured the behavior of new pairs of cells driven with different sets of stimuli protocols.

To conclude, both computational and experimental lines of inquiry support the counterintuitive notion that the RB-AII is able to reliably encode RB membrane potential fluctuations at mean V_M = -51 mV but fails to encode this modulation at mean V_M = -45 mV.

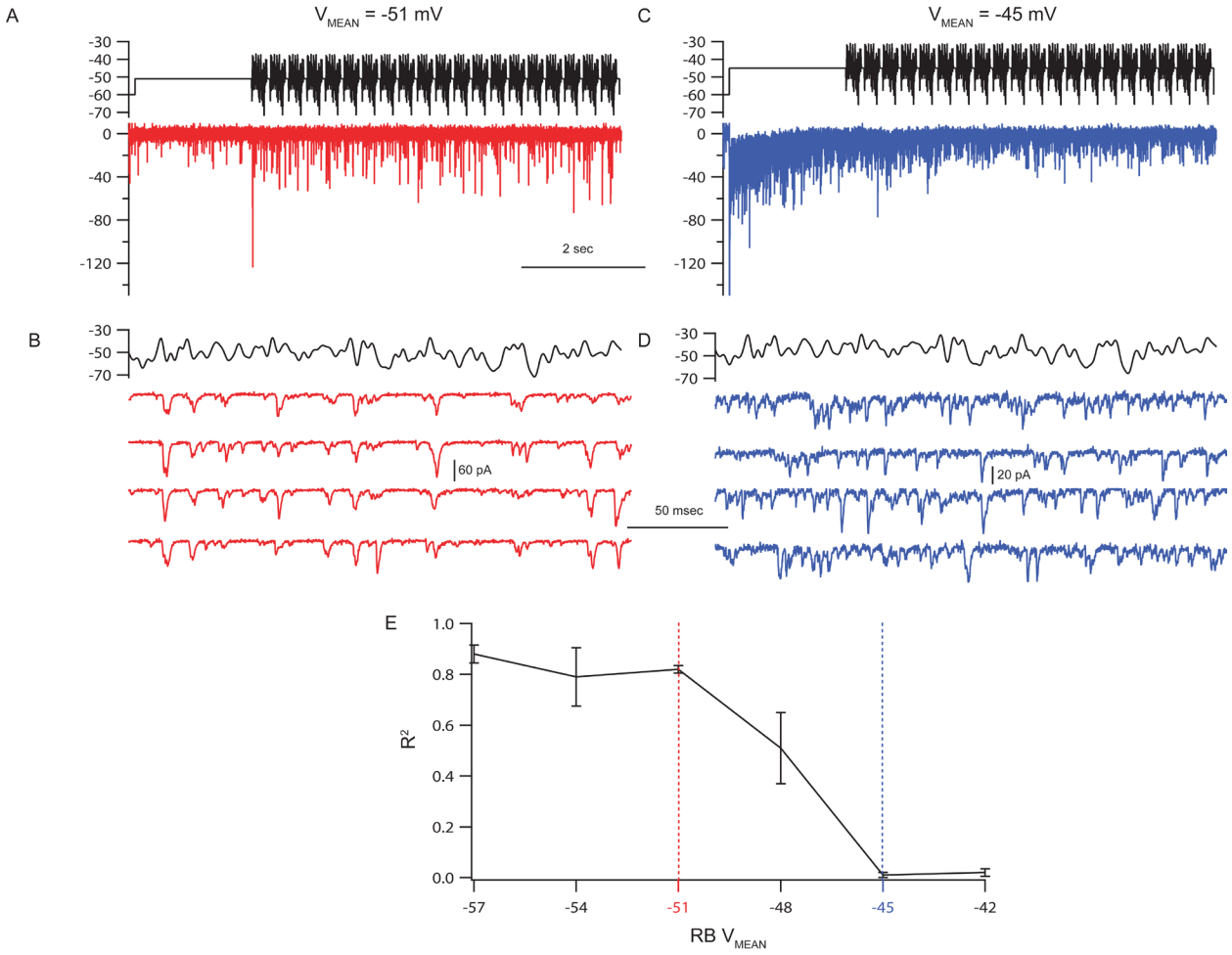

Figure 2.12. The RB-AII synapse becomes uncorrelated between -51 mV and -45 mV.
A. The RB was driven with 20 repeats of the same white noise stimulus (V_M = -51 ± 6 mV, black). Responses were recorded in the postsynaptic AII (red). B. Example responses (red) to repeats of the stimulus waveform (black) from A. C,D. As in A,B, but with V_M = -45 ± 6 mV. In C, the EPSC evoked by the initial DC voltage step is truncated to facilitate comparison with A. E. The R^2 value between two averaged distinct sets of repeats (2 sets of 10 responses) shows a sharp transition from reproducible release (at mean V_M = -51 mV) to uncorrelated release (at mean V_M = -45 mV) over a 6 mV range, as predicted by the synapse model.

2.5. Discussion

The time-varying distribution of retinal bipolar cell V_M changes with the visual scene, thereby altering transmission from bipolar cells and inducing the adaptations to background and contrast measured in postsynaptic neurons (Beaudoin et al., 2007; Dunn et al., 2007; Dunn and Rieke, 2008; Manookin and Demb, 2006). Here, we examined the mechanisms underlying adaptation at the RB-AII synapse when varying the mean or variance of presynaptic V_M. A 6 mV depolarization within the RB's physiological operating range reduced synaptic gain by ~65% as a result of RRP depletion and Ca channel inactivation. Increasing the time-varying SD of V_M three-fold reduced synaptic gain by ~18%; this reduction was explained by RRP depletion alone. Our study elucidates how simple presynaptic mechanisms adjust the gain of transmission at retinal synapses on a rapid time scale to match the statistics of a changing visual scene.

2.5.1. A biophysical mechanism for synaptic gain control

Synaptic transmission at bipolar cell synapses has been studied extensively [reviewed by (Matthews, 1999; Matthews and Fuchs, 2010; Sterling and Matthews, 2005; von Gersdorff and Matthews, 1999)]. Studies that characterized phasic release described fundamental properties of the synapses (e.g., RRP sizes). In these studies, exocytosis was evoked using brief voltage steps to potentials more depolarized than those experienced during visual stimulation, and tonic exocytosis was suppressed by hyperpolarizing the neurons between steps. Although these studies demonstrated that RB and other bipolar cell synapses exhibit profound paired-pulse depression that arises primarily from RRP depletion (Mennerick and Matthews, 1996; Singer and Diamond, 2006; von Gersdorff and Matthews, 1997), it is difficult to extend these results and make

quantitative predictions about the degree of RRP depletion during physiological function, in which V_M is modulated in a narrow range (~10 – 20 mV) around the resting potential, and Ca channel gating and exocytosis occur tonically.

Therefore, we quantified synaptic gain changes at the RB synapse elicited by tonic presynaptic depolarizations comparable to those evoked by visual stimulation. We complemented this analysis with a realistic model of the presynaptic AZ. To estimate the relative contributions of Ca channel inactivation and RRP depletion to the gain changes observed, we predicted synaptic output when inactivation was included or excluded as a feature of the model (i.e., variable $h = 1$ for all mean V_M; see Sect. 2.3.2). Postsynaptic contributions to synaptic gain changes were not included in the model because AMPARs on the AII are neither saturated nor desensitized by ongoing synaptic transmission (Jarsky et al., 2010; Singer, 2007; Singer and Diamond, 2006; Singer et al., 2004).

Our model attributes gain changes observed following changes in the mean or variance of V_M, in part, to a common mechanism: a reduction in the RRP available to participate in exocytosis (Fig. 2.10). Thus, vesicle recycling rate limits the number of available vesicles during periods with depolarization: as the presynaptic membrane spends more time at depolarized potentials (owing either to a depolarized mean potential or to frequent large, transient depolarizations), the RRP shrinks and synaptic gain is reduced [also see (Jackman et al., 2009)].

Adaptation to variance was attributable to RRP depletion alone: the gain change observed in the simulated response to increased stimulus SD was unaffected by removing the inactivation parameter from the model (gain change = 15% in both cases). This finding is consistent with the experimental observation that Ca currents show little inactivation at -48 mV (Jarsky et al., 2011). Furthermore, transient ($<<$100 ms) voltage excursions from -48 mV should not cause substantial

Ca channel inactivation because the time constant for inactivation is slow (~400 ms). Accordingly, previous studies demonstrated that Ca channel inactivation did not contribute to synaptic depression at RB synapses when depolarizing stimuli were relatively brief (<100 ms) (Singer and Diamond, 2006; Singer et al., 2004).

Ca channel inactivation contributed to adaptation to the mean. At mean V_M positive to -48 mV, inactivation of recorded presynaptic Ca currents was evident (steady-state / peak = 0.34 at -42 mV; see Jarsky et al., 2011). Consequently, removing the model's inactivation feature altered both the simulated responses and the gain change arising from depolarizing mean V_M from -51 to -45 mV: the gain change was 64% with inactivation present (resembling the experimental effect) but only 37% with inactivation absent. Further, the simulated response to a quasi-white noise stimulus of mean V_M = -45 mV failed to reproduce the experimental response without inactivation present: large stimulus fluctuations evoked large postsynaptic responses, and these responses became better correlated with the stimulus than were the experimental ones (i.e., more vesicles were available for correlated release; see Sect. 2.3.2).

Simplistically, the model's reduced gain at the depolarized V_M (0.36) is a function of two factors: RRP depletion (0.62; taken from the simulation with Ca channel inactivation absent) and Ca channel inactivation (0.36/0.62 = 0.58). Thus, Ca channel inactivation and RRP depletion may affect gain similarly. The relative contribution of Ca channel inactivation to gain control is not unexpected. At RB synapses, exocytosis varies linearly with the number of open channels owing to the close coupling between channels and release sites (Jarsky et al., 2010). Consequently, lowering Ca current amplitude will generate a proportional reduction in synaptic release (Jarsky et al., 2010). This differs from observations of conventional synapses like the calyx of Held, at which coupling between Ca channels and release sites is looser, and a small

change in Ca channel availability generates large changes in the number of vesicles released (Xu and Wu, 2005).

2.5.2. Relevance to visual processing

Here, we quantified the effect of 'pure' changes in either the mean or SD of RB membrane potential on synaptic gain (Figs. 2.4 and 2.5). The RB voltage was not taken to be a specific reproduction of a particular visual scene; rather, we used our analytical approach to assess how well-defined changes in presynaptic V_M affected the synaptic transfer function. In reality, the mean and SD of V_M change simultaneously, especially at scotopic intensities [reviewed by (Dunn et al., 2007)]. For example, when only one of the ~20 rods presynaptic to a RB (Tsukamoto et al., 2001) absorbs a single photon within the rods' integration time (~100 ms), contrast is almost impossible to define (i.e., it is either 0% or 100%). Increasing the mean intensity, then, will depolarize the RB and increase fluctuations in V_M. Under these conditions, changes in the mean and SD of RB V_M will combine to generate synaptic gain control.

Our study suggests that the ability to adapt to contrast is an intrinsic property of RB–and by extension, all bipolar cell–synapses. Under conditions in which bipolar cells can detect contrast [>10 R*/rod/sec; (Beaudoin et al., 2008)], their individual synapses should adapt at high contrast, without requiring network interactions, and generate adaptive responses in postsynaptic neurons (Beaudoin et al., 2007; Brown and Masland, 2001; Manookin and Demb, 2006). The simulations presented here, however, do not preclude contributions from other cellular mechanisms resident to bipolar cells.

In the salamander retina, fast-onset contrast adaptation observed in ganglion cells is proposed to arise from a Ca^{2+}-dependent mechanism that adjusts the presynaptic bipolar cells'

responses to photoreceptor input (Rieke, 2001). This mechanism may be modified further by the bipolar cells' intrinsic membrane properties [see (Mao et al., 1998)]. Thus, in the future it will be important to determine whether gain control mechanisms exist in mammalian bipolar cell somata and dendrites and how they interact with the synaptic mechanism described here. Furthermore, it is notable that the mechanisms underlying background adaptation in (ON-type) RBs may not contribute to adaptation in OFF cone bipolar cells, because elevated background luminance should hyperpolarize OFF cells.

Previous recordings of gain control at RB-AII synapses were observed with small increases in background luminance (1 R*/rod/s) that evoked only ~2 mV depolarizations of RBs [to a V_M ~ -52 mV; see Fig. 2.3; (Dunn and Rieke, 2008)]. Under these conditions, synaptic gain was reduced by ~45%. This gain change likely depended primarily on RRP depletion, as we observed very little Ca channel inactivation at V_M = -54 to -51 mV. Ca channel inactivation became evident only during tonic depolarization to more positive potentials (Jarsky et al, 2011; corresponding to a background of ~10 R* / rod / sec), suggesting that Ca channel inactivation may broaden the operating range of the RB synapse by limiting RRP depletion during tonic depolarization elicited by backgrounds of 10 – 100 R* / rod / s (in the range of -51 mV < V_M < -45 mV examined here; Fig. 2.4, 2.11).

CHAPTER 3

An axonless retinal interneuron with action potential-like spiking

3.1. Summary

In typical neurons, action potentials are generated at the axon initial segment. Several types of retinal interneurons, however, exhibit spikes but lack axons. One such neuron is the AII amacrine cell, in which spikes recorded at the soma exhibit small amplitudes (<10 mV) and broad time courses (>5 ms). Here, we used electrophysiological recordings and computational modeling to examine the mechanisms underlying this atypical spiking. We found that the small, slow events recorded in the soma represent filtered versions of large, brief action potential-like spikes initiated at a single, electrotonically-distal dendritic compartment. In this same distal compartment, spiking undergoes slow modulation, likely by an M-type K conductance. Thus, the physiology of the axonless AII is much more complex than would be anticipated from morphological descriptions and somatic recordings; in particular, the AII possesses a distal dendritic structure that is strikingly similar to the axon initial segment found in typical neurons.

3.2. Introduction

In the mammalian retina, the AII amacrine cell distributes rod-driven synaptic input from the rod bipolar cell to ON and OFF retinal ganglion cells. Often called the rod amacrine cell (Strettoi et al., 1992), recent studies have demonstrated that the AII functions also in cone-mediated vision (Manookin et al., 2008; Munch et al., 2009). Because it operates during both rod- and cone-mediated vision within most of the parallel pathways that generate retinal output, understanding the AII is critical to comprehending signaling within the inner retina.

The AII is an unconventional neuron: it is axonless and has only a soma and an elaborate dendritic tree (Strettoi et al., 1992; Tsukamoto et al., 2001; Veruki et al., 2010). A theoretical study has suggested that the small size of the AII (<100 μm end-to-end distance) makes it electrotonically compact (Vardi and Smith, 1996). Indeed, more recent experimental evidence demonstrated that the AII's dendrites appear to act as a single processing unit: rod-driven synaptic inputs generate synchronous outputs to the ON and OFF pathways despite the fact that the loci of these outputs are on physically separate portions of the dendritic tree (Murphy and Rieke, 2006, 2008; Strettoi et al., 1992; Tian et al., 2010).

Several features of spiking in AIIs, however, are inconsistent with its being electrotonically compact. AIIs spike intrinsically at high rates (up to hundreds of Hz), with somatically-recorded spikes being small (<10 mV), broad (>5 ms), and capable of superposition (Boos et al., 1993; Tamalu and Watanabe, 2007; Tian et al., 2010; Veruki and Hartveit, 2002a, b). It is unclear how an isopotential AII could intrinsically produce such atypical spike waveforms. Moreover, superposing spikes in somatic recordings are typically associated with

spikes arising from multiple dendritic locations, requiring cells to be electrotonically noncompact (Oesch et al., 2005).

Here, we combined computational analyses with electrophysiological recordings to elucidate the unconventional anatomical and electrophysiological characteristics of the AII. We found that the AII membrane is not isopotential, nor do spikes arise from multiple dendritic locations. Rather, spikes appear to originate from a single, electrotonically distal site, indicating that the AII has a dendritic compartment that acts like a conventional axon initial segment. At this location, a slow negative feedback mechanism consistent with an M-type K conductance modulates spiking. Our results clarify previous electrophysiological and theoretical analyses of the AII and describe the unexpected electrotonic structure of the most common inhibitory interneuron in the mammalian retina (Jeon et al., 1998; Strettoi and Masland, 1996): the AII is noncompact despite its being small, and its spikes are initiated at a single location despite its having an elaborate dendritic arbor.

3.3. Methods

Here, methods are included for the computational modeling, as well as for the experimental techniques used by the author. Where indicated, other experimental methods have been omitted but can be found in the corresponding paper (Cembrowski et al., 2011).

3.3.1. Tissue preparation

Experiments were performed on retinae isolated from adult (4-8 weeks old) light-adapted C57BL/6 wild-type and Cx36 (connexin-36) knockout (Deans et al., 2001) mice, as described previously (Tian et al., 2010). The Animal Care and Use Committee of Northwestern University approved all procedures involving animal use. Retinae were isolated into bicarbonate buffered Ames' medium (Sigma) equilibrated with 95% O_2/5% CO_2 (carbogen). Retinae then were embedded in low-melting temperature agarose (Sigma type VIIA, 3% in a HEPES-buffered saline), and slices (200 μm) were cut on a vibrating microtome (Microm). Slices were stored in carbogen-bubbled Ames' medium at room temperature until use.

3.3.2. Data collection

All experiments were performed at near-physiological temperature (~34°C). Retinal slices were superfused with an artificial CSF (ACSF) containing the following (in mM): 119 NaCl, 23 $NaHCO_3$, 10 glucose, 1.25 NaH_2PO_4, 2.5 KCl, 1.15 $CaCl_2$, 1.5 $MgCl_2$, 2 Na-lactate and 2 Na-pyruvate. Picrotoxin (100 μM), strychnine (0.5 μM), and 6,7-dinitroquinoxaline-2,3-dione (DNQX) (10 μM) were added to the ACSF to block $GABA_A$ receptor-activated, glycine receptor-activated, and AMPA/kainite receptor-activated currents, respectively. In experiments

where noted, tetraethylammonium chloride (TEA-Cl; broad-spectrum K channel antagonist) (2 mM), 4-aminopyridine (4-AP; broad-spectrum K channel antagonist) (2 mM), linopirdine dihydrochloride (LP; selective M-type K antagonist) (30 μM), $CdCl_2$ (50 μM; broad spectrum voltage-gated Ca channel antagonist), $BaCl_2$ (250 μM; broad spectrum voltage-gated K channel antagonist), tetrodotoxoin (TTX; voltage-gated Na channel antagonist) (300 nM), riluzole hydrochloride (1 μM; noninactivating Na channel antagonist), CsCl (2 mM; HCN channel antagonist), or L(+)-2-amine-4-phosphonobutyric acid (L-AP-4) (5 μM; metabotropic glutamate receptor antagonist) were added.

Pipettes were filled with the following solution (in mM): 110 K-gluconate, 5 NaCl, 10 HEPES, 0.2 EGTA, 8 Tris-phosphocreatine, 4 MgATP and 0.4 NaGTP. In some experiments, the fluorescent tracers Alexa 488 or 594 (2 μM; Invitrogen) were included in the pipette to permit visualization of the cellular morphology by epifluoresence. Access resistances were typically <25 MΩ; compensation was not used and junction potentials were not corrected.

Drugs were obtained from Sigma or Tocris Bioscience (except for TTX, which was from Alomone Labs). Recordings were made using a MultiClamp 700B amplifier (Molecular Devices). Data were filtered at 2-5 kHz and digitized at 10-20 kHz using an ITC-18 A/D board (Instrutech) controlled by custom routines written in Igor 6.2 (Wavemetrics) running on a personal computer (Apple).

Data analysis was performed using IGOR Pro (Wavemetrics) and Microsoft Excel (Microsoft). Paired, two-tailed *t* tests were used to compare paired datasets, with significance accepted as $p < 0.05$. Data are presented as mean ± SEM. In some figures, symbols are included and denote individual cells.

3.3.3. Analysis of spiking

Spikes were detected by applying a threshold to the derivative of current-clamp recordings. In general, spikes rose much faster than any other membrane potential fluctuations, allowing firing events to be unambiguously resolved. To calculate the number of spikes per burst, current-clamp recordings were converted into rasters and groups of spikes were denoted as bursts whenever sequential firing times occurred <20 ms from each other. As intraburst spiking tended to exhibit interspike intervals <=8 ms and interburst intervals generally were >=40 ms (eg, Fig. 3.3), the choice of a 20 ms window was able to separate periods of bursting from quiescence.

3.3.4. Analysis involving voltage-gated K channel antagonists

To investigate the change in spike height evoked by K channel antagonists in Figure 3.6, we passed hyperpolarizing current to keep AIIs near spike threshold and measured the height of initial spikes in bursts evoked by a small (10 pA) sustained current injection. Restricting analysis to initial spikes circumvented two difficulties that would make comparing all spike heights ambiguous. First, spike heights showed some dependence on their relative timing within a burst; by examining the first spike only, we removed this dependence on the timing of the spike itself. Second, TEA and 4AP (see Sect. 3.3.2) affected repolarization and made it difficult to discern individual events near the midpoint of the burst; considering only the first spike made it unnecessary to assign amplitudes to these later waveforms. The initial spike height was defined as the maximal difference in voltage in the window of time between the onsets of the first and second spikes in a burst (illustrated on representative bursts in Fig. 3.6Ai).

To calculate the input resistance during an injected current ramp in Fig. 3.8, voltage responses were divided into 5 mV intervals from -70 mV to -40 mV. For each voltage interval, we calculated the best fit line to the data and defined input resistance as the voltage change of the best fit line divided by the current required to produce this change.

Additionally, we observed that application of $BaCl_2$ alone induced large amplitude (>20 mV) spontaneous membrane potential oscillations that were abolished in the presence of Cd^{2+}. These oscillations likely arose from Ba^{2+} flux through voltage-gated Ca channels. Generally, then, Ba^{2+} and Cd^{2+} were coapplied (with one exception; see Fig. 3.9D-F); in separate control experiments, we confirmed that Cd^{2+} did not change the observed behavior.

3.3.5. Simulations involving the "stylized model"

All numerical simulations were performed with the computational software NEURON (Hines and Carnevale, 1997) using the variable timestep (CVODE) method.

For the "stylized" cell, the three-compartment morphology consisted of the following: a large cylinder (the "soma"; length = 25 μm, diameter = 25 μm, 1 segment) connecting to a thin cable (the "cable"; length = 32 μm, diameter = 0.3 μm, 11 segments) terminating in a varicosity (the "initiation site"; length = 2 μm, diameter = 2 μm, 1 segment). The large model soma was taken to represent the electrical equivalent of the soma and arboreal dendrite of the AII. The cable and initiation site were taken to represent the long neurite and terminal varicosity branching asymmetrically from the AII primary dendrite, with respective lengths and diameters taken from measurements obtained through confocal reconstruction (LSM 510; Carl Zeiss) of an individual AII filled with Alexa 594. The morphologies, as depicted in Figure 3.10, have had the cables and initiation sites enlarged only for purposes of illustration. In all sections, the specific

membrane capacitance was 1 μF cm^{-2}, axial resistivity was 150Ω cm, membrane resistivity was 10,000 Ω cm^2, and the leak reversal potential was -40 mV. The cable was taken to be passive, and Hodgkin-Huxley-like active conductances were added to the soma and initiation site. An incompletely-inactivating A-type conductance, with parameters constrained by voltage-clamp recordings (Tian et al., 2010), was inserted into both sections. We also verified that inserting this A-type conductance into the cable, with a density equal to that of the soma, did not make a significant difference to the model output (data not shown). The initiation site contained additional fast Na and slow noninactivating K conductances, with parameters tuned to produce spike threshold, spike frequency, and burst duration similar to that recorded experimentally at the soma. The Na and K reversal potentials were taken to be +50mV and -77mV, respectively. Each active conductance is described in detail below. Associated parameters for these conductances are provided in Table 3.1, with voltage-dependent behavior illustrated in Figs. 3.1-3.2.

The A-type K current i_A was given by

$$i_A = \overline{g}_A \, m_A \left(c \, h_A^{(1)} + (1-c) \, h_A^{(2)} \right) (V - E_K) \tag{3.1}$$

where m_A and $h_A^{(j)}$ $(j = 1,2)$ solve

$$\tau_{m_A} \frac{dm_A}{dt} = m_{\infty_A}(V) - m_A, \tag{3.2}$$

$$\tau_{h_A^{(j)}} \frac{dh_A^{(j)}}{dt} = h_{\infty_A}(V) - h_A^{(j)}. \tag{3.3}$$

Here, $h_A^{(1)}$ captures fast inactivation with the timescale

$$\tau_{h_A^{(1)}} = 25 - 20 * [1 + \exp(-(V+35)/6)]^{-1}, \tag{3.4}$$

$h_A^{(2)}$ captures slow inactivation with the timescale

$$\tau_{h_A^{(2)}} = \min\left[(V+17)^2/4 + 26, 100\right], \tag{3.5}$$

and $c = [1 + \exp(-(V+45)/15))]^{-1}$ denotes the proportion of current which is fast-inactivating. Finally,

$$m_{\infty_A}(V) = [1 + \exp(-(V - V_{1/2_{m_A}})/k_{m_A}))]^{-1}, \tag{3.6}$$

$$h_{\infty,A}(V) = f\,[1 + \exp((V - V_{1/2_{h_A}})/k_h))]^{-1} + (1-f). \tag{3.7}$$

with $f = 0.83$ to capture incomplete inactivation.

The slow K current i_S was given by

$$i_S = \overline{g}_S\ m_S\,(V - E_K), \tag{3.8}$$

where

$$\tau_{m_S}\ \frac{dm_S}{dt} = m_{\infty_S}(V) - m_S, \tag{3.9}$$

$$m_{\infty_S}(V) = [1 + \exp(-(V - V_{1/2_{m_S}})/k_{m_S}))]^{-1}. \tag{3.10}$$

The Na current i_{Na} was given by

$$i_{Na} = \overline{g}_{Na}\ m_{Na}^3\ h_{Na}\ (V - E_{Na}), \tag{3.11}$$

where

$$\tau_{m_{Na}}\ \frac{dm_{Na}}{dt} = m_{\infty_{Na}}(V) - m_{Na}, \tag{3.12}$$

$$\tau_{h_{Na}}\ \frac{dh_{Na}}{dt} = h_{\infty_{Na}}(V) - h_{Na}, \tag{3.13}$$

$$m_{\infty_{Na}}(V) = [1 + \exp(-(V - V_{1/2_{m_{Na}}})/k_{m_{Na}}))]^{-1}, \tag{3.14}$$

$$h_{\infty_{Na}}(V) = [1 + \exp((V - V_{1/2_{h_{Na}}})/k_{h_{Na}}))]^{-1}. \tag{3.15}$$

Table 3.1. Parameter values for active conductances

Current		τ_m (ms)	τ_h (ms)	$V_{1/2_m}$ (mV)	k_m (mV)	$V_{1/2_h}$ (mV)	k_h (mV)	$\overline{g}_{SOMA}$ (S/cm^2)	$\overline{g}_{IS}$ (S/cm^2)
A		1	Eqns.3. 4, 3.5	-10	7	-40.5	2	0.004	0.08
S		50	-	-40	4	-	-	0	0.03
Na		0.01	0.5	-48	3	-49.5	2	0	0.2

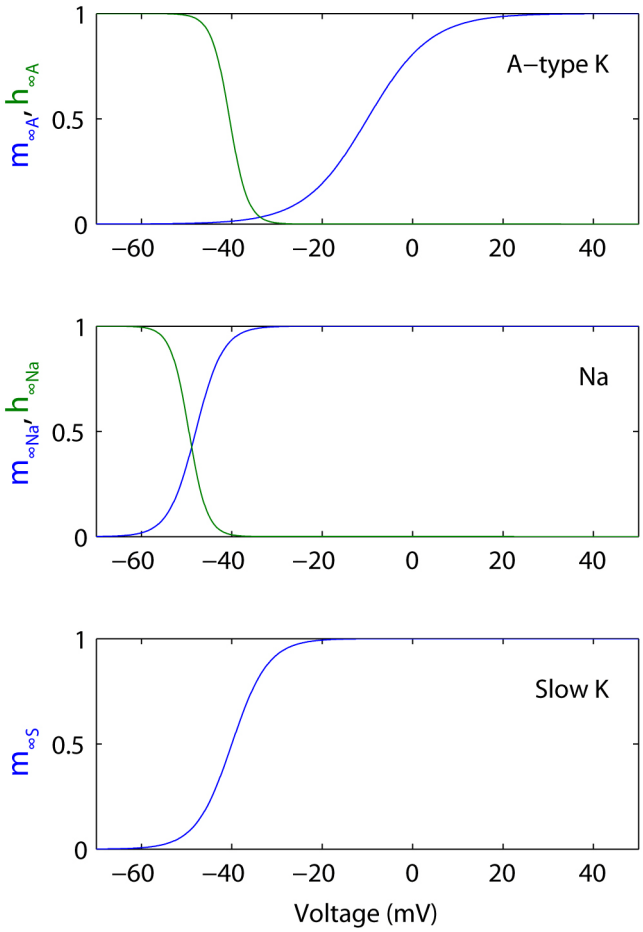

Figure 3.1. Steady-state activation and inactivation in the computational model.
The steady-state activation (blue) and inactivation (green) curves are illustrated for the three active conductances used in the AII model. For the A-type K conductance, for simplicity the noninactivating component (produced by f, Equation 3.7) has not been illustrated.

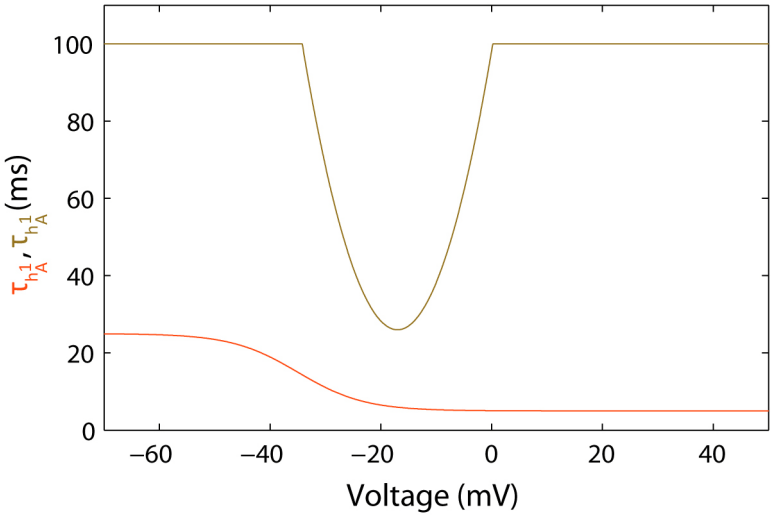

Figure 3.2. Inactivation kinetics of the A-type K channel.
Fast (orange) and slow (gold) inactivation time constants of the A-type K channel are illustrated (Equations 3.4 and 3.5 respectively). The remaining gating variables have voltage-independent time constants and can be found in Table 3.1.

3.3.6. Simulations involving multiple initiation sites in the stylized model

For simulations incorporating two spiking compartments in parallel, a second identical cable and initiation site were included and connected to the soma. Because the two initiation sites had identical geometries and conductances, in a noiseless model the two sites would synchronize. It, however, is extremely unlikely that two such initiation sites would be synchronized in a functioning neuron: such a phenomenon would require the virtual elimination of noise sources (e.g., stochastic channel gating) within the membrane. Therefore, to mimic the

physiological situation, we introduced a small asymmetry into the model: we increased the excitability of one site by simulating the injection of a small bias current (5 pA). Incorporating slight differences in the model AII's active or passive properties could also make the excitability of the two sites different.

For the simulation incorporating three spiking compartments in parallel, a second and third identical initiation site were included and connected to the soma. We increased the excitability of one site by injection of a small depolarizing bias current (5 pA) and decreased the excitability of a second site by injection of a small hyperpolarizing bias current (5 pA).

For simulations incorporating two spiking compartments in series, a second cable and initiation site were included and connected to the first initiation site. Anatomically, the second cable had a variable diameter (as described in Results), whereas the first and second initiation sites were geometrically equivalent. Biophysically, the second cable was passive; the second initiation site had A- and M-type K as at the first initiation site, and in some simulations, also included Na (as described in Results).

3.3.7. Simulations involving the "complete model"

For simulations of a morphologically realistic AII (the "complete model"), we recapitulated an AII filled with a fluorescent tracer. This model contained a soma connected to a primary dendrite, which in turn was coupled to three structures. First, branching midway from the primary dendrite was the cable and initiation site as used in the simplified AII model. Second, 7 small branches emerged from the distal primary dendrite, each of which terminated in a lobular appendage. Third, the primary dendrite gave way to a dendritic arbor: the primary dendrite bifurcated into 2 secondary dendrites; each secondary dendrite branched into 2 tertiary

dendrites; and each tertiary dendrite branched into 5 quaternary dendrites. The geometrical parameters of these compartments are given in Table 3.2; the structures of the cable and initiation site were identical to the simplified model and have been omitted from the table.

As in the three-compartment model, active conductances were inserted into the initiation site whereas the associated cable was passive. The soma was also taken to be passive, as has been demonstrated experimentally (Tian et al., 2010). A-type K was distributed uniformly across the remaining structures, with the density employed in the three-compartment model. All parameters associated with the active and passive conductances were identical to those used in the three-compartment model.

Table 3.2. Geometric parameters for detailed morphology

Compartment		nseg	Length (μm)	Diam (μm)
Soma		1	14	12
1° dendrite		3	18	2
2° dendrite		5	25	1
3° dendrite		5	10	0.75
4° dendrite		7	25	0.5
Lobule branch		1	4	1
Lobule		1	4	4

3.3.8. Simulations involving the "Na/K_A model"

For simulations using the initial model with only Na and K active conductances (the "Na/K_A model"), the morphology employed a branched structure similar to that used in the complete morphological model, except for decreases in both the amount of branching and the diameter of arboreal processes. In total, this produced a surface area in the Na/K_A AII of about half that of the complete model. A-type K and Na conductances were similar to those used in the stylized and complete models, with two exceptions. First, the Na/K_A model employed Na activation and inactivation time constants approximately one order of magnitude slower than the other models. Second, the Na/K_A model included a spatially-variable A-type K density fit to voltage-clamp data (Tian et al., 2010) by NEURON's MultiRunFitter routine. Finally, the Na/K_A model also inserted noisy fluctuating point conductances at the site(s) of spike initiation as well as the soma (Destexhe et al., 2001).

3.3.9. Experiments verifying the existence of a single dendritic initiation site

The experimental methods used to confirm AIIs have a single dendritic initiation site, as performed by Stephen Logan of the Singer Laboratory (patch-clamp recording) and Li Jia of the Li Laboratory (immunohistochemistry), will appear in a manuscript currently under review (Cembrowski et al., 2011).

3.3.10. Adding simulated RB events to the AII

To simulate RB-mediated mini excitatory postsynaptic potentials (mEPSPs), we play in one or more quantal events via NEURON's Exp2Syn, NetCon, and NetStim classes. The current associated with a mini i_M was given by

$$i_M = g_M \; c \left[\exp\left(-\frac{t}{\tau_2}\right) - \exp\left(-\frac{t}{\tau_1}\right)\right] (V - E_{AMPA}), \tag{3.16}$$

where g_M = 0.3 nS, τ_1 = 0.25 ms, τ_2 = 0.6 ms, and E_{AMPA} = 0 mV; $c = \left[\max_t \left\{\exp\left(-\frac{t}{\tau_2}\right) - \exp\left(-\frac{t}{\tau_1}\right)\right\}\right]^{-1} = \left[\left(\frac{\tau_1}{\tau_2}\right)^{\frac{\tau_1}{\tau_2-\tau_1}} - \left(\frac{\tau_1}{\tau_2}\right)^{\frac{\tau_2}{\tau_2-\tau_1}}\right]^{-1}$ acted to normalize the difference of exponentials. The parameters of this current were chosen to produce a simulated mEPSC (delivered at the soma in voltage-clamp; -80 mV holding potential) that resembled the average mEPSC recorded experimentally (Jarsky et al., 2010).

3.3.11. Simulations involving stochastic RB input

To implement a stochastic version of the RB-AII synapse model of Chapter 2, we employed simulations with a discrete pool of available vesicles N with a maximum available pool N_∞ = 80. This available pool obeyed the initial condition $N^0 = N_\infty$. On each timestep $t^k = k\,\Delta t$, the probability of release p_{REL} for each available vesicle was given by

$$p_{REL}(V(t^k)) = r(V(t^k))\,\Delta t, \tag{3.17}$$

and the probability of recycling p_{REC} for each unavailable vesicle was given by

$$p_{REC} = \alpha\,\Delta t, \tag{3.18}$$

for $r(V)$ and α defined in the previous chapter. The step size Δt = 0.025 ms was chosen to match the sampling rate used in experiments. The RB command voltage $V(t)$ was assigned according to the flash response found experimentally (A. Sampath, personal communication); multiple realizations (see below) were conducted for each flash strength (Fig. 3.19). After calculating the vesicles to be released N_{REL}^k and the vesicles to recycled N_{REC}^k on the k^{th} timestep, the available vesicles at the next timestep N^{k+1} was updated according to

$$N^{k+1} = N^k - N^k_{REL} + N^k_{REC}. \quad (3.19)$$

After calculating all release events for a given realization, a delay for each event was assigned by drawing from the corresponding Gaussian distribution of Chapter 2.

In total, 100 realizations of synaptic release were simulated for each flash waveform.

For each realization, the timing of release events was then used to drive corresponding RB mEPSPs in the stylized AII model. Each RB event was a uniquantal, identical mEPSP delivered to the soma (as described in the previous section). Each realization of release events was delivered in four different AII regimes: simulations were run at both at rest and at hyperpolarized potentials, each of which was also done both with and without Na channels (as described in the Results section). To cause the AII to be hyperpolarized, -30 pA of DC bias current was injected. In each of the four conditions (rest vs. hyperpolarized & with vs. without Na channels), responses in the stylized AII were averaged over 100 realizations for each flash strength.

In these stochastic simulations (as well as the mean simulation in Fig. 3.20), we took $r(V)$ as defined for $V_{MEAN} \leq -54$ mV (Table 2.1); that is, neither Ca inactivation nor asynchronous release were present. For most flash strengths, RB responses to flashes were briefer and more hyperpolarized than that needed for pronounced Ca channel inactivation (and presumably, uncorrelated release). For the brighter flashes where these two features might play roles, it is unlikely that they would shape transient responses in the AII: depletion of the pool occurred much faster than Ca inactivation (Figs. 3.19,3.20).

3.3.12. Simulations involving a gap junction-coupled AII network

When using the stylized AII in a gap junction-coupled network, individual AIIs were arranged on a rectangular lattice and were coupled to their four nearest neighbours at the soma (with the exception of AIIs at the edges and corners of the lattice, which coupled to their three and two nearest neigbhours, respectively). The current induced by gap junction coupling i_{GJ} was given by

$$i_{GJ} = -g_{GJ}(V_1 - V_2), \tag{3.20}$$

with g_{GJ} = 400 pS (constrained by experiments; data not shown). In (3.20), V_1 was the voltage in the first ("presynaptic") compartment and V_2 was the voltage in the second ("postsynaptic") compartment; using the convention of positive-outward synaptic current, i_{GJ} was therefore the current flowing into the postsynaptic compartment from the presynaptic compartment.

Introduction of gap junction coupling in the AII network would naturally lead to a decrease in the input resistance of an individual AII. To correct for this, the membrane resistivity was increased from 10,000 Ω cm^2 to 40,000 Ω cm^2, giving a whole-cell reduction in leak conductance nearly equivalent to the point source increase introduced by the gap junctions. Without compensation, in turn this reduction in leak conductance would hyperpolarize the AII slightly (E_{LEAK} = -40 mV $> V_{REST}$ ~ -50 mV baseline); to avoid this, we increased E_{LEAK} modestly (to E_{LEAK} = -30 mV). This produced a baseline membrane potential for the gap junction-coupled AII that was similar to the individual stylized AII. Note, in Figure 3.21, the subthreshold AII network was obtained by setting E_{LEAK} = -61 mV.

All network simulations employed a 15 x 16 array of AIIs, with the stimulated cell being in the fifth row and sixth column.

3.4. Results

3.4.1. AIIs exhibit small amplitude tonic and burst firing

We first recorded spiking in AIIs in the light-adapted retina. In accord with previous studies, spikelets exhibited stereotyped waveforms that lacked afterhyperpolarizations (Boos et al., 1993; Tian et al., 2010; Veruki and Hartveit, 2002a, b) (Fig. 3.3A). Additionally, when hyperpolarized to threshold (V_{THRES} ~-60 mV; achieved by injections of hyperpolarizing sub-threshold currents or "STCs" of 30 - 80 pA), small depolarizations evoked burst firing (Fig. 3.3B). During bursts, high-frequency spikes superposed. When larger current steps were superposed on the STC, bursting behavior was eliminated, and AIIs spiked tonically.

Thus, AIIs can exhibit both tonic and burst firing, and the mode of firing is voltage-dependent. This finding provides a useful experimental paradigm to assess the conductances involved in spiking in the AII.

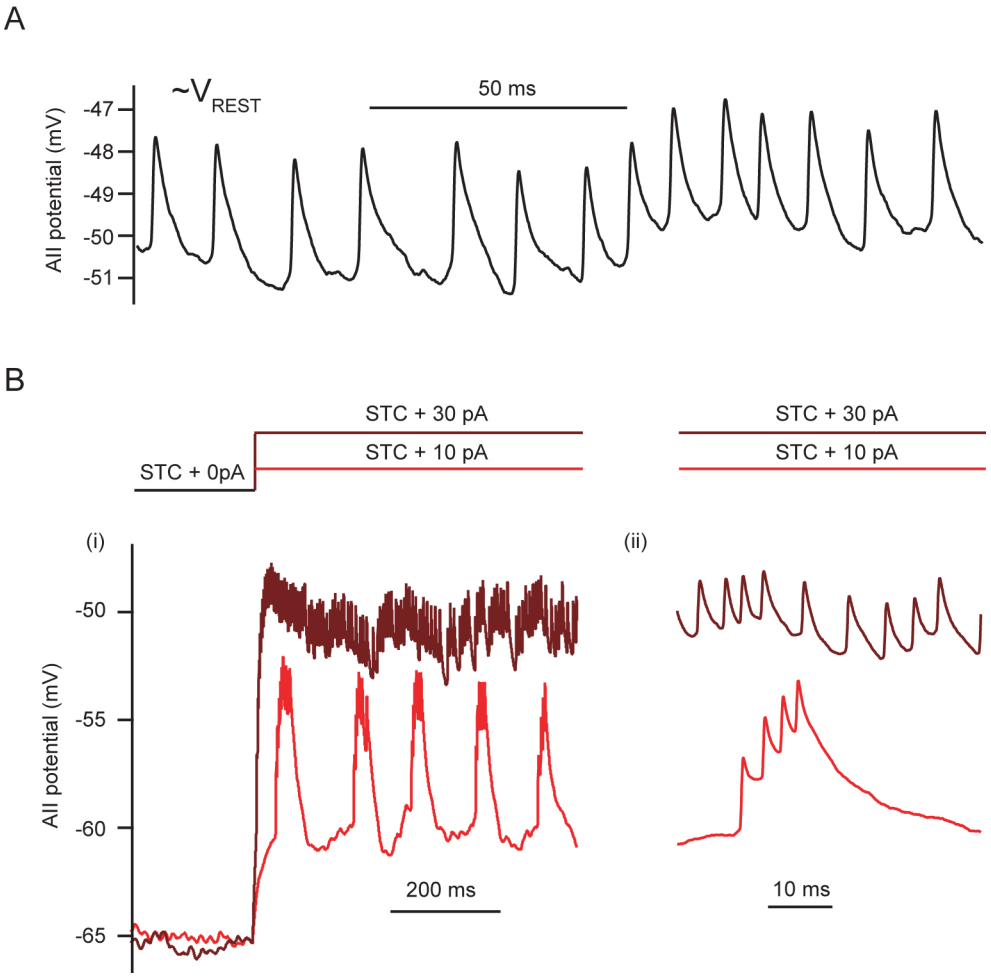

Figure 3.3. Somatically-recorded spiking in AIIs
A. Spontaneously-occurring spikes at rest exhibited small amplitudes and stereotyped waveforms. B. (*i*) When the AII was initially held below spike threshold by STC, small suprathreshold current steps induced bursts of superposing spikes. Larger current steps elicited tonic firing. (*ii*) Expanded view of bursting and tonic spiking.

3.4.2. The Na/K_A AII model suggests spikes are initiated electronically distal to the soma

To gain insight into the mechanisms underlying firing in the AII, we began by constructing a simple computational model that contained only two voltage-gated conductances; namely, Na and A-type K (the "Na/K_A AII"; see Sect. 3.3.8). This model contained the smallest number of active conductances needed to study regenerative spiking, providing a straightforward

approach to initially investigate AII firing. We sought to use this simplified AII model to clarify the distributions of Na channels, as well as the electrotonic structure of the AII, that could give rise to the unconventional AII somatic spikes. In particular, we wanted our simple model to capture two features of AII responses. One, we required small (~5 mV) spikes to be recorded at the soma; two, we sought to capture superposition of spikes with a refractory period between firing events (Figs. 3.3, 3.4A).

First, we attempted to recapitulate experimental results using a model where the soma was the site of spike initiation (Fig. 3.4B*i*). However, this implementation led to pronounced inconsistencies with experimental data, attributable to the gating properties of the A-type K conductance. When implementing this conductance realistically (as constrained from voltage-clamp recordings; see Sect. 3.3.8), somatically-initiated spikes were generally very large (tens of millivolts; e.g., Fig 3.4B*i*). This action potential-like amplitude was a consequence of the voltage dependence of the A-type K channel, which activated at potentials >-40 mV and did not show a steep dependence on voltage (Fig. 3.1). Both of these properties were in direct opposition to two features needed by the Na/K_A model. First, the model required A-type K activation near -60 mV, in order to counteract spikes occurring near threshold. Second, the model required a very steep activation curve: the A-type K conductance needed to be sufficiently deactivated prior to spiking (in order to allow spike generation), while simultaneously needing to be strongly activated by a small (~5 mV) spikelet to limit spike height.

As this mechanism of spiking seemed inconsistent with experimental data, we next turned to a model where spikes were initiated in the distal dendritic arbor. To this end, one or two initiation sites were added to the arbor (see Sect. 3.3.8; Fig. 3.4B). By virtue of morphologically-distal initiation, both models produced attenuated spikes (Fig. 3.4B*ii,iii)*;

moreover, each model overcame the shortcoming of the somatic initiation model by producing of large distal spikes which activated A-type K channels. However, each version of the model exhibited a new discrepancy with the experimental data. Although the model with one initiation site gave responses similar to what was seen experimentally over most voltages (Fig. 3.4A), it failed to produce spike superposition. Conversely, a model with two initiation sites exhibited this feature, yet deviated from experiments by producing superposing events with arbitrarily short interspike intervals. Importantly, neither model produced the clearly defined burst behavior near spike threshold. Rather, in both models noise present at the initiation site(s) (see Sect. 3.3.8) served to initiate spikes near threshold, a mechanism that would not be expected to produce the pronounced burst firing seen in experiments.

In addition, previous experiments have illustrated that AIIs can exhibit suppression of spiking following depolarization. This, too, was a feature that was not produced by our basic single- and dual initiation site models incorporating two voltage-gated conductances (Fig. 3.5).

Therefore, although the Na/K_A model provided initial insight into spiking, it was clear that this simple model was insufficient to recapitulate multiple properties of AII firing. Before moving to construct a more complete model that expanded on this preliminary insight, however, we thought it important to first perform two sets of experimental inquiries to constrain our next model. First, we wanted to test the Na/K_A prediction of distally-initiated spikes; second, we sought to characterize and identify the source(s) of the slow modulation associated with bursting in the AII.

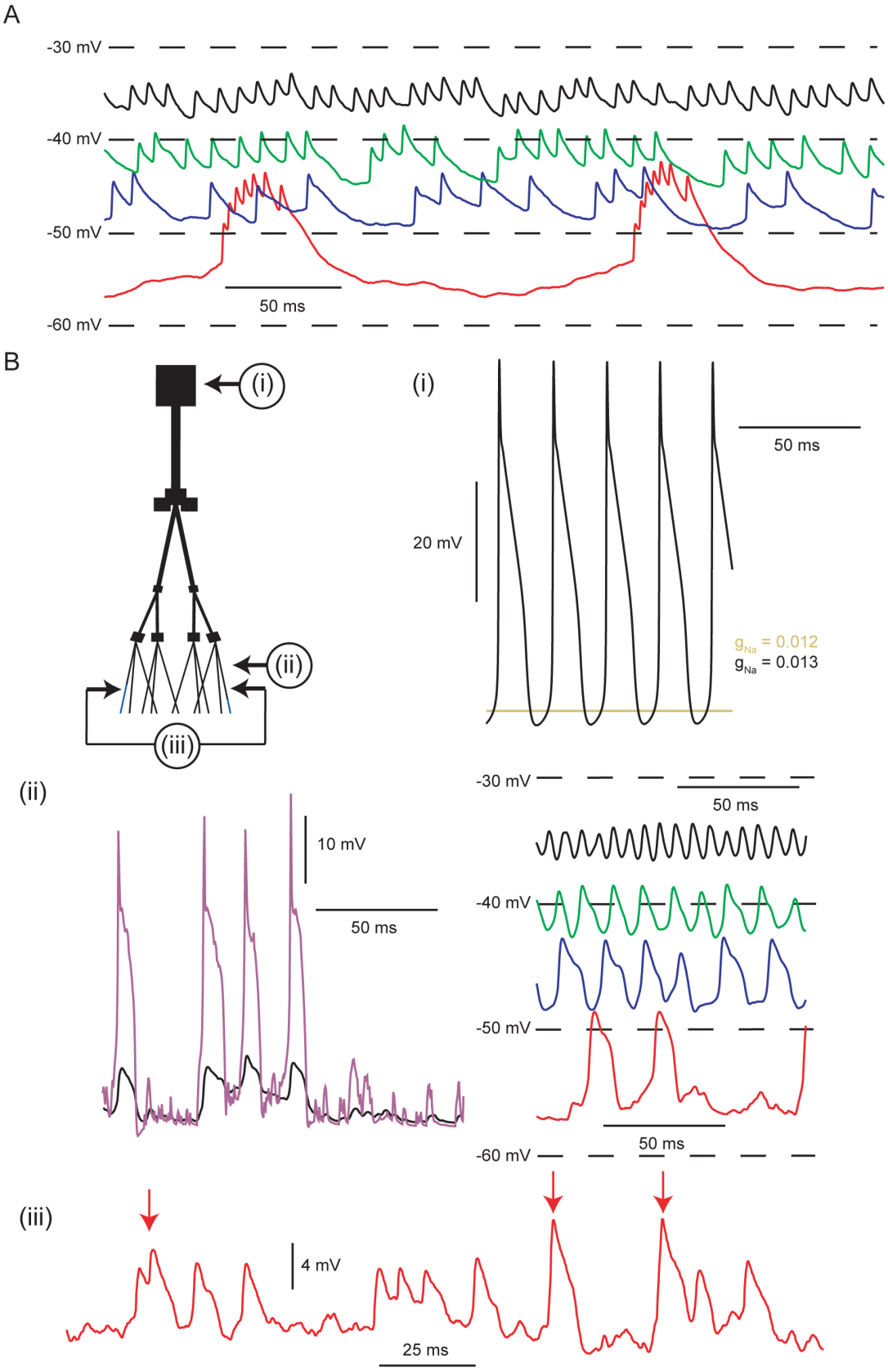
A
-30 mV
-40 mV
-50 mV
50 ms
-60 mV
B
(i)
(ii)
(iii)
(i)
50 ms
20 mV
g_{Na} = 0.012
g_{Na} = 0.013
-30 mV
50 ms
(ii)
10 mV
50 ms
-40 mV
-50 mV
50 ms
-60 mV
(iii)
4 mV
25 ms

Figure 3.4. The Na/K_A model suggests spiking arises distal to the soma.
A. Representative experimental responses in an AII are shown, following a variety of DC current injections to give different baseline voltages. B. Example model responses when the site of spike initiation is varied. The AII morphology is illustrated, with the sites of spike initiation in *i-iii* depicted. *i*. When Na channels were added to the soma, the model produced large action potential-like waveforms for sufficiently high densities of Na channels (black). Reducing Na channel density slightly caused the cell to stop spiking completely (gold), illustrating the difficulty in producing regenerative, small spikes with a somatic initiation site. In these simulations, noise from fluctuating conductances was not used. *ii.* Left: a model with a single initiation site within the dendritic arbor produced large local spikes (purple) which were attenuated at the soma (black). Right: somatic responses are illustrated as in A. *iii.* A model with two initiation sites within the dendritic arbor produced superposing spikes (arrows); however, they could occur without any refractoriness.

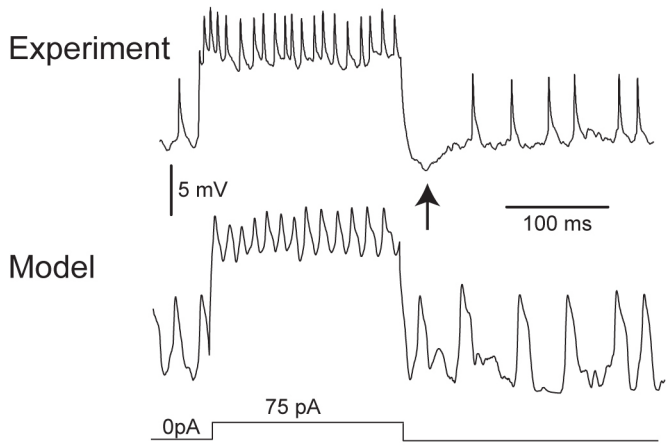

Figure 3.5. Suppression of spiking following return from depolarization is not found in the Na/K_A model
A representative experimental response to a long current step (top) showed a suppression of spiking following current offset (arrow). These responses did not emerge from the simple Na/K_A model (bottom).

3.4.3. Experimental results confirm K conductances do not strongly limit spike height

Within experiments, we sought to determine whether the small, somatically-recorded spikes might reflect a fast K conductance counteracting depolarizations from a voltage-gated Na conductance (Scott et al., 2007). This scheme is plausible, as K currents in AIIs show a prominent A-type component (Boos et al., 1993; Tian et al., 2010). Blocking the A-type K conductance with TEA or 4-AP, however, produced only small increases in the height of the initial spike in a burst (Fig. 3.6Ai,ii; see Sect. 3.3.3 for why initial spike used).

Alternatively, as suggested by the Na/K_A model, spikes could be initiated in one or more dendritic compartments isolated electrotonically from the soma by morphological choke points or by leaky dendrites. The small spikes recorded at the soma might therefore represent attenuated versions of larger, dendritically-initiated spikes.

Here, we provide experimental evidence for this assertion: in voltage-clamp, a step in somatic holding potential from -80 mV to -50 mV evoked regenerative, TTX-sensitive inward action currents (n=4, Fig. 3.6Bi). To exclude the possibility that poor voltage control arose from electrical coupling between AIIs, in collaboration with the Singer Laboratory, identical unclamped action currents were recorded from AIIs in the Cx36-/- mouse in which electrical coupling between AIIs is absent (n=4/4, Fig. 3.6Bii) (Deans et al., 2002). We conclude, then, that the majority of voltage-gated Na channels in the AII must be located at a site (or sites) electrotonically distal to the soma.

To investigate whether these Na currents were the source of spikelets, recorded TTX-sensitive action currents were injected via the recording pipette in the presence of TTX. A single action current waveform elicited a voltage response resembling a spikelet (Fig. 3.6Biii), and the

injection of a train of action currents evoked superposing spikes resembling a burst (Fig. 3.6Biv). These results suggest that the action currents observed in voltage-clamp underlie spiking in current-clamp, and therefore spiking occurs even when somatic voltage is held fixed.

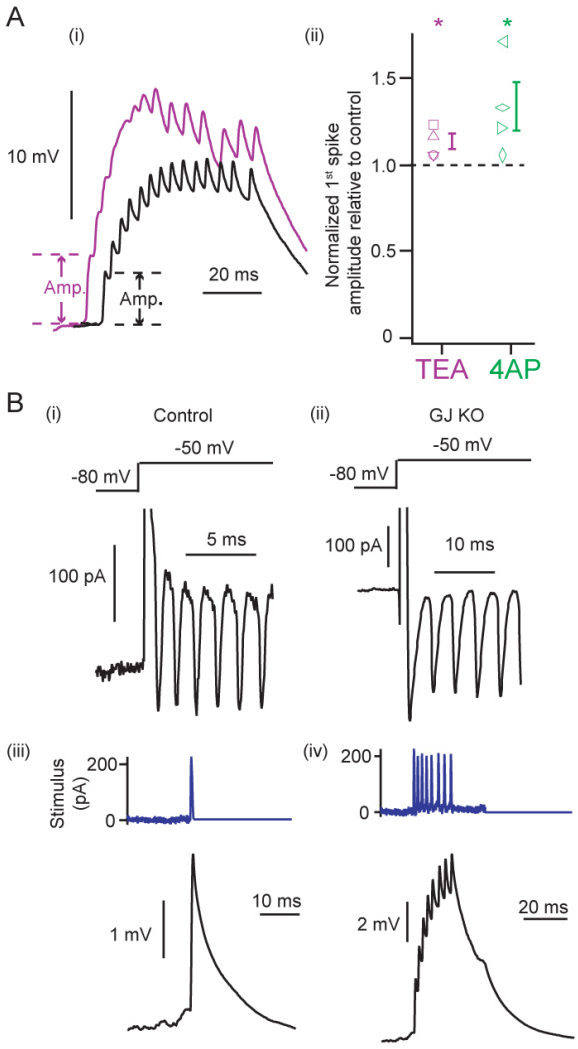

Figure 3.6. Spikes are initiated electrotonically distal to the soma
A. (*i*) A burst is depicted in control conditions (black), as well as after application of TEA (purple). TEA inhibited recovery and modestly increased the initial spike height. Measurement of the initial spike height is illustrated in *i*. (*ii*) TEA and 4AP produced significant but small increases in spike height (TEA: 114 ± 4% relative to control; 4AP: 133 ± 14% relative to control; n=4 cells in each case; $p < 0.05$ in each case). B. In voltage-clamp configuration, a suprathreshold step from -80mV to -50mV evoked regenerative, stereotyped inward events in AIIs from both wild-type (*i*) and gap junction knockout (*ii*) mice. In an AII from a control mouse, injecting a single inward event as depolarizing current in the presence of TTX evoked a waveform similar to a spike in control conditions (*iii*). Injecting a train of regenerative events in TTX elicited superposing spikes resembling a burst waveform (*iv*).

3.4.4. Spiking is modulated bidirectionally on a single timescale

Generally, intrinsic bursting requires regenerative spiking modulated by negative feedback from a slower conductance (Izhikevich, 2007). To begin to characterize the slow conductance operating in AIIs, first we assessed the voltage range over which it was active. We considered two possible scenarios: one, the slow conductance might require hyperpolarization to operate, potentially explaining why cells burst following hyperpolarization (Fig. 3.3). Two, the slow conductance might also be active at more depolarized potentials, and therefore modulate spiking bidirectionally; in particular, returns from depolarization should suppress firing owing to the slow adaptation of this conductance.

To differentiate between these two cases, we examined after-potentials at current offset following large hyperpolarizing or depolarizing current injections. In all AIIs tested (n=6/6), transient bidirectional modulation was observed: rapid superposing bursts of spikes (after-depolarizations) were evoked following returns from hyperpolarization, whereas spiking was

transiently suppressed (after-hyperpolarizations) following depolarization (Fig. 3.7Ai, single trial; Fig. 3.7Aii, averaged response). Importantly, these after-depolarizations and after-hyperpolarizations were comparable in duration, suggesting that they arose from the same conductance. Moreover, their timescales were similar to those of spontaneous, regenerative bursts seen near threshold (Fig. 3.3).

For a subset of cells from the previous protocol (n=3/6), we looked for additional adaptation on longer timescales by tracking voltage responses for ~7 seconds after current offset. For all cells examined (3/3), we saw no evidence for additional adaptation (Fig. 3.7B).

3.4.5. Slow modulation occurs distal to the soma

Where is the site of the slow conductance relative to the soma? If located electrotonically proximal to the soma (and therefore controlled by somatic voltage), application of TTX should eliminate spiking but not the underlying slow after-potentials. Alternatively, if the slow conductance is located distally (eg, close to regenerative conductances), TTX might exert large effects on the after-potentials by blocking the large local voltage spikes driving slow modulation. We found that blocking Na channels with TTX strongly reduced the transient after-depolarizations and after-hyperpolarizations (example trace, Fig. 3.7Ci; averaged response, Fig. 3.7Cii). This finding supports our assertion that the slow conductance is located distal to the soma and likely found at the spike initiation site(s). Importantly, the fact that TTX blocks both after-depolarizations and after-hyperpolarizations again reinforces the assertion that both arise from a single conductance.

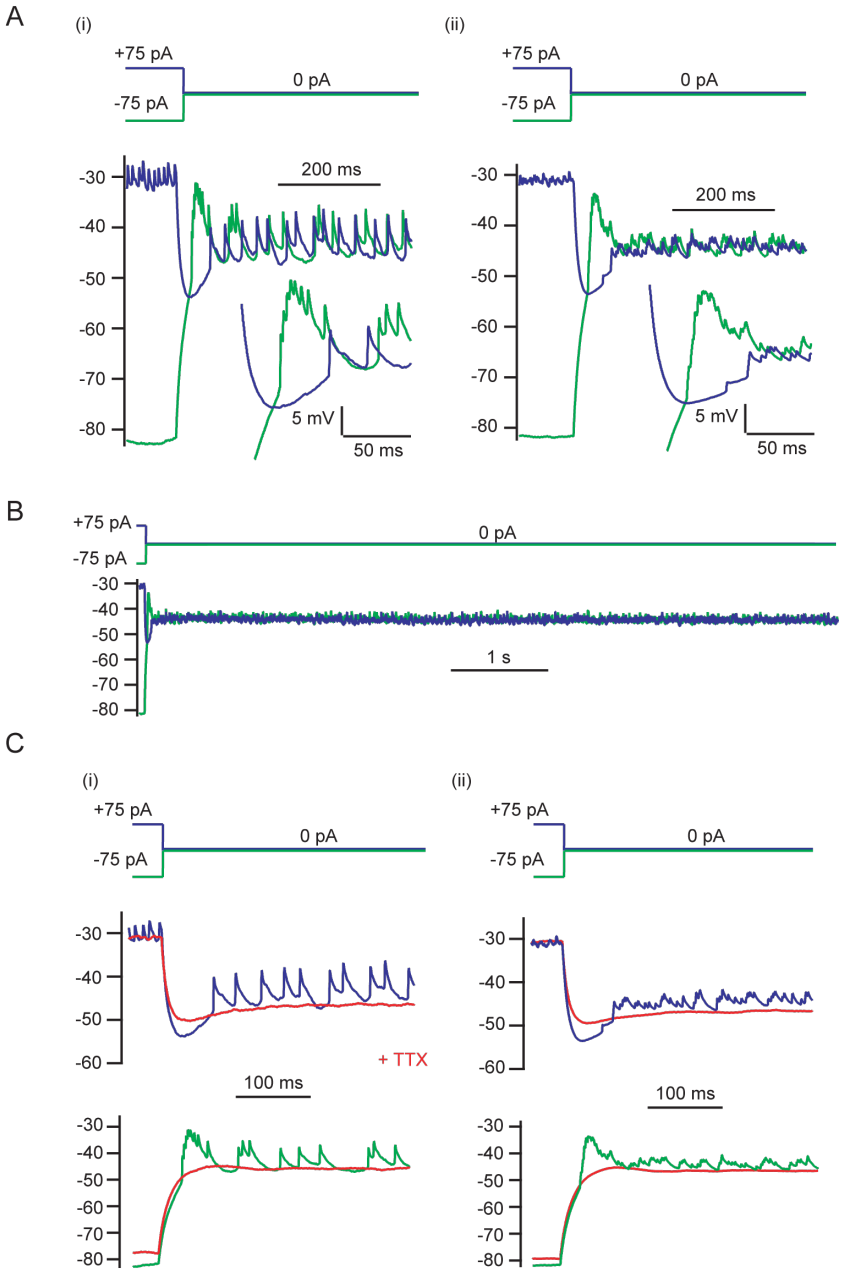
A
(i)
+75 pA
-75 pA
0 pA
200 ms
-30
-40
-50
-60
-70
-80
5 mV
50 ms
(ii)
+75 pA
-75 pA
0 pA
200 ms
-30
-40
-50
-60
-70
-80
5 mV
50 ms
B
+75 pA
-75 pA
0 pA
-30
-40
-50
-60
-70
-80
1 s
C
(i)
+75 pA
-75 pA
0 pA
-30
-40
-50
-60
+ TTX
100 ms
-30
-40
-50
-60
-70
-80
(ii)
+75 pA
-75 pA
0 pA
-30
-40
-50
-60
100 ms
-30
-40
-50
-60
-70
-80

Figure 3.7. Slow modulation is bidirectional, exhibits one timescale, and is distal
A. Repolarization in the AII is illustrated following either a +75 pA (blue) or -75 pA (green) current injection, for a single trial (*i*) and an average across trials (*ii*). Respectively, responses exhibited transient after-hyperpolarizations and after-depolarizations which obeyed a similar time course. B. Responses over a longer time window did not show any further adaptation (averaged response depicted only). C. Application of TTX (red) to either protocol strongly reduced transient behavior following current offset. Both an individual trial (*i*) and an averaged response (*ii*) are shown.

3.4.6. The slow conductance appears to be an M-type K conductance

The slow conductance modulating bursting in AIIs resembled the M-type K conductance for three reasons. One, it was active near spike threshold and modulated spiking bidirectionally; two, the timescales of afterpotentials were on the order of M-type current kinetics observed in other systems; three, no further adaptation occurred following the afterpotentials, in agreement with the noninactivating nature of M channels (Adams et al., 1982a; Robbins et al., 1992). Therefore, we tested the hypothesis that an M-type K conductance interacts with the Na conductance to generate bursting behavior. We blocked the underlying channels with 30 μM LP (Aiken et al., 1995; Schnee and Brown, 1998) and observed the effect on burst duration: if an M-type K conductance is critical for terminating bursts, LP should increase burst duration.

In the presence of LP, the durations of evoked bursts were prolonged (n = 7). In 3/7 AIIs, spikes/burst increased and bursting was maintained (control vs. LP spikes/burst: 3.9 ± 1.1 vs. 15.3 ± 3.0; n=3; $p < 0.05$; Fig. 3.8B). In the remaining 4/7 AIIs, bursting was abolished altogether, and cells exhibited only tonic spiking following depolarization (Fig. 3.8C). LP did not

affect the height of spikes within the bursts, suggesting that it did not block the A-type K conductance to any appreciable extent (Fig. 3.9G).

Separately, we investigated how LP affected input resistance and resting membrane potential by injecting current ramps into recorded AIIs. These recordings were done in the presence of TTX to prevent changes in spiking from confounding these measurements. LP depolarized AIIs and increased Rn at potentials depolarized to -55 mV (Fig. 3.8Di). For recordings in which after-hyperpolarizations were evident following current offset (6/10 AIIs), LP either decreased their amplitudes (n=2/6) or abolished them entirely (n=4/6). These results are consistent with LP blocking an M-type K conductance.

Qualitatively identical results were obtained using Ba^{2+} (250 μM) to block M-type K conductances (Adams et al., 1982b; Kotani et al., 2000) (Fig. 3.9, A-C,G), as well as with the high-affinity antagonist XE-991 (10 μM) (Wang et al., 1998; Zaczek et al., 1998) (Fig. 3.9, D-G). Further, we eliminated contributions to bursting from other, non M-type K conductances (voltage-gated Ca channels, persistent Na channels, HCN channels, and Ca-gated channels; Fig. 3.9, H-I). These findings therefore suggest that spiking undergoes slow modulation from an M-type K conductance exclusively.

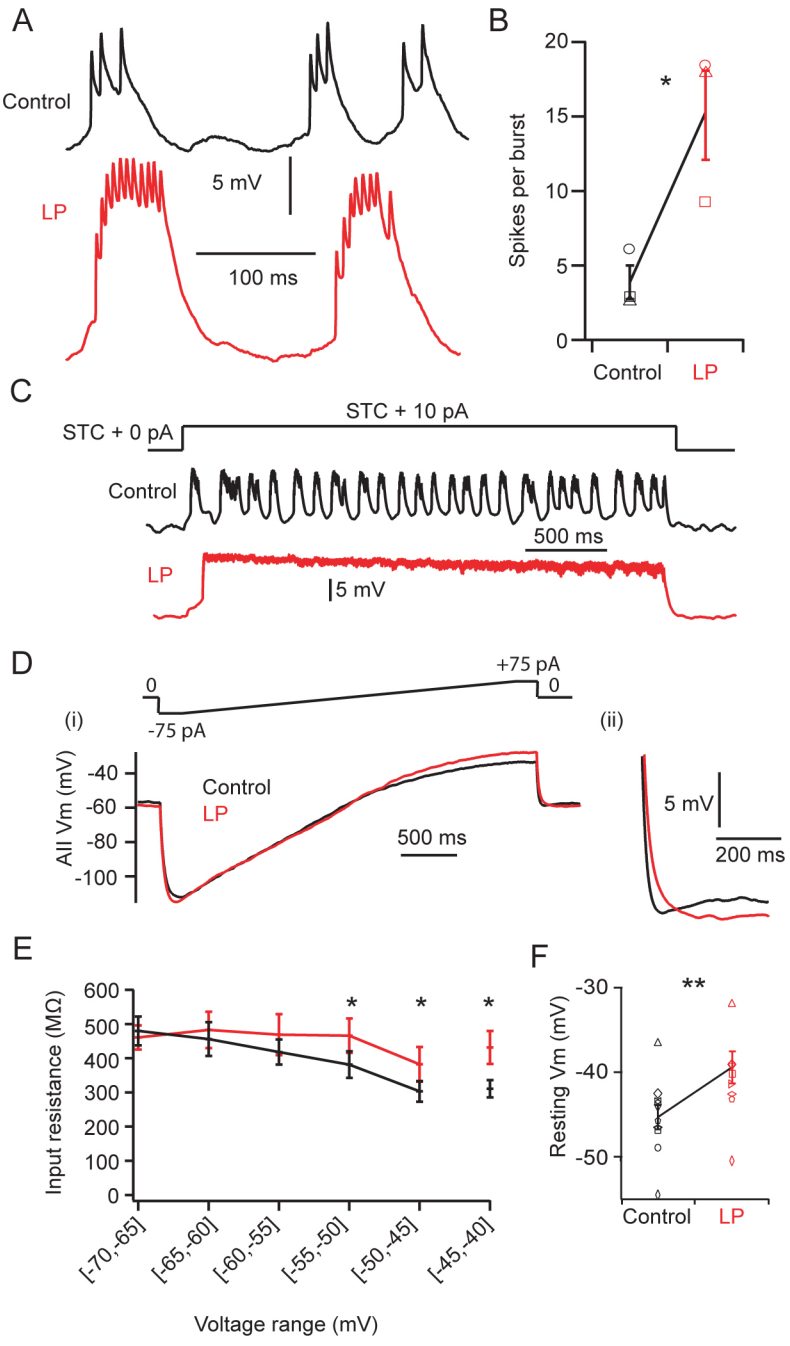
A
Control
LP
5 mV
100 ms
B
Spikes per burst
20
15
10
5
0
*
Control
LP
C
STC + 0 pA
STC + 10 pA
Control
500 ms
LP
5 mV
D
0
+75 pA
0
(i)
-75 pA
(ii)
All Vm (mV)
-40
-60
-80
-100
Control
LP
500 ms
5 mV
200 ms
E
Input resistance (MΩ)
600
500
400
300
200
100
0
*
*
*
[-70,-65]
[-65,-60]
[-60,-55]
[-55,-50]
[-50,-45]
[-45,-40]
Voltage range (mV)
F
Resting Vm (mV)
-30
-40
-50
**
Control
LP

Figure 3.8. Results from pharmacological manipulations are consistent with modulation by an M-type K conductance
A. Application of LP increased spikes/burst in the AII. B. Summary of the increase in spikes/burst in cells not exhibiting complete loss of burst mode (control vs. LP spikes/burst: 3.9 ± 1.1 vs. 15.3 ± 3.0; n=3; $p < 0.05$). C. Example trace from an AII where bursting was abolished (n=4 total). D. In the presence of TTX, an AII was ramped (*i*) from -75pA to +75pA over 2 s in control (black) and after LP was applied (red). Following current offset (*ii*), the small after-hyperpolarization was eliminated in the presence of LP. E. Summary of input resistances, after partitioning the ramp response into 5 mV voltage intervals, in control and LP (see Sect. 3.3.4; $p > 0.05$ for voltages intervals below -55mV, and $p < 0.05$ otherwise; only 5/10 cells reached voltages of at least -40 mV in both control and LP and the [-45 mV,-40 mV] data point represents data from this subset of cells; n=10 for all other intervals;). F. Summary of the change in resting potential following the addition of LP (control: -45.2 ± 1.5 mV, LP: -38.2 ± 2.0 mV; n=10; $p < 0.01$).

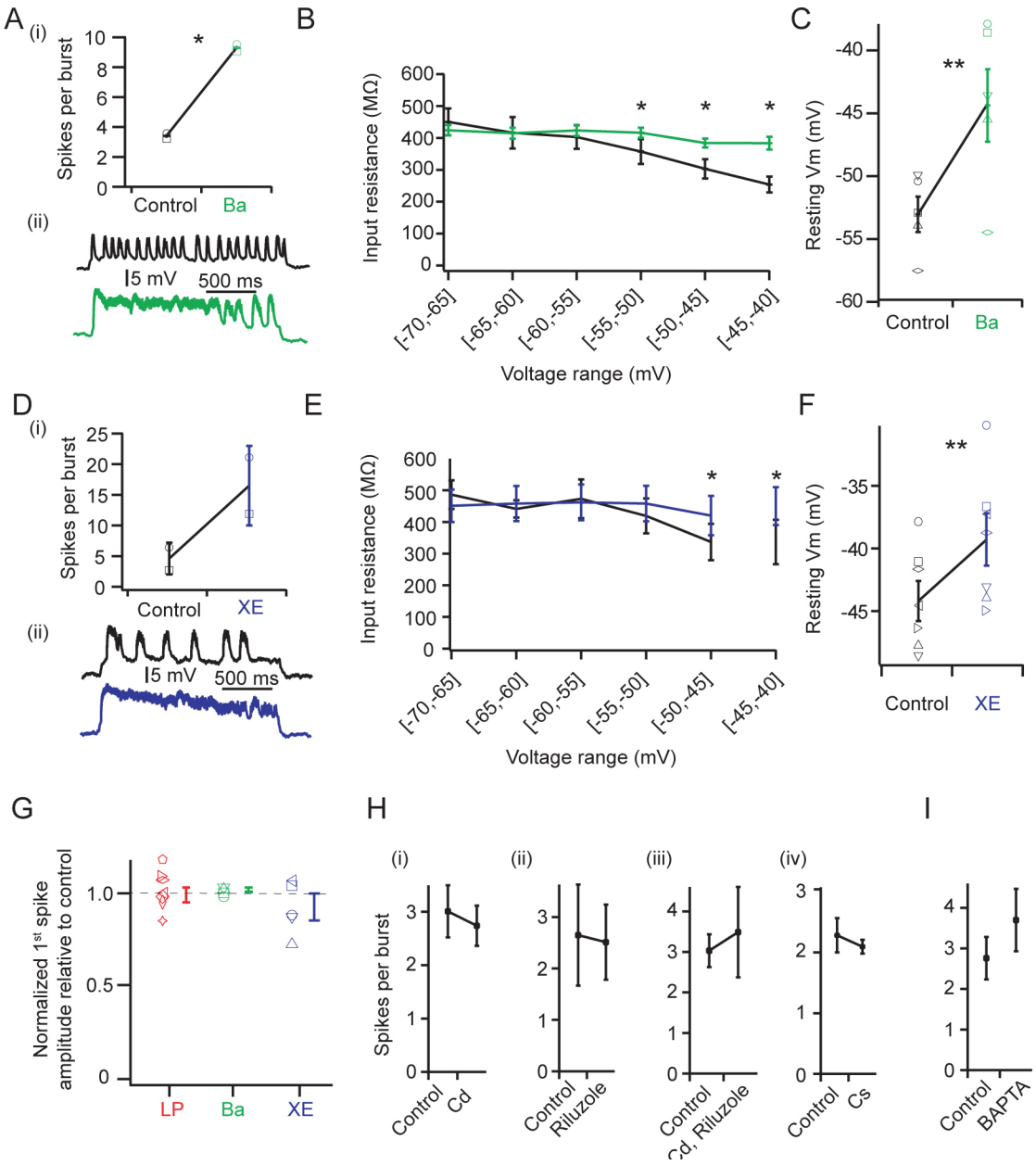
A
(i)
Spikes per burst
Control
Ba
(ii)
5 mV
500 ms
B
Input resistance (MΩ)
Voltage range (mV)
[-70,-65]
[-65,-60]
[-60,-55]
[-55,-50]
[-50,-45]
[-45,-40]
C
Resting Vm (mV)
Control
Ba
D
(i)
Spikes per burst
Control
XE
(ii)
5 mV
500 ms
E
Input resistance (MΩ)
Voltage range (mV)
F
Resting Vm (mV)
Control
XE
G
Normalized 1st spike amplitude relative to control
LP
Ba
XE
H
(i)
Spikes per burst
Control
Cd
(ii)
Control
Riluzole
(iii)
Control
Cd, Riluzole
(iv)
Control
Cs
I
Control
BAPTA

Figure 3.9. Bursting appears to be modulated by an M-type K conductance only

(A-C) Protocols as in Fig. 3.8B,C,E,F but employing Ba. Ba prolonged bursts in all cells: either spikes/burst significantly increased while bursts still terminated (*i*: control vs. Ba spikes/burst: 3.4 ± 0.3 vs. 9.4 ± 0.2; $p < 0.05$; n=2), or bursting was eliminated and the cell typically showed either high-frequency tonic firing or quiescence (*ii*, n=1). (B) Ba increased the input resistance significantly for voltage intervals above -55mV while leaving voltage intervals below -55mV unchanged ($p < 0.05$ for each interval above -55mV and $p > 0.05$ for each interval below -55mV; n=5 for each interval). (C) Ba significantly depolarized AIIs (zero-current voltage, control vs. Ba: -53.2 ± 0.7 mV vs. -44.0 ± 1.1mV; n=5; $p < 0.001$). (D-F) Protocols as in (A-C) but employing XE-991. XE increased excitability in all spiking cells (D*i*: control vs. XE spikes/burst for cells retaining burst mode: 4.6 ± 2.6 vs. 16.5 ± 6.5; n=2; D*ii*: n=3 cells showed high-frequency tonic firing only following XE), significantly increased input resistances at depolarized potentials (E, $p < 0.05$ for each interval above -50 mV and $p > 0.05$ for each interval below -50mV; n=5 for [-45,-40], n=8 otherwise), and significantly depolarized AIIs (F, zero-current voltage, control vs. XE: -44.2 ± 1.6 mV vs. -39.3 ± 2.1 mV; n=7; $p < 0.01$). (G) Addition of M-type K antagonists did not increase initial spike heights (increase relative to control: LP: 101 ± 1%, n=7; Ba: 102 ± 1%, n=4; XE: 93 ± 7%, n=5; $p > 0.05$ for all). (H) As in Fig. 3.8, spikes per spontaneously-occurring burst were measured in control and in the presence of voltage-gated channel antagonists: Cd (*i*; 3.0 ± 0.5 vs. 2.7 ± 0.4; n=3; $p > 0.05$), riluzole (*ii*, 2.7 ± 1.0 vs. 2.5 ± 0.7; n=3; $p > 0.05$), Cd and riluzole coapplied (*iii*, 3.0 ± 0.4 vs. 3.5 ± 1.1; $p > 0.05$; n=3), or Cs (*iv*, 2.3 ± 0.3 vs. 2.1 ± 0.1; $p > 0.05$; n=3). (I) Spikes/burst were compared from the control bursts in (G) to spikes/burst occurring in cells recorded with 5 mM BAPTA in the recording pipette (2.8 ± 0.5 vs. 3.7 ± 0.8; control: n=12, BAPTA: n=5; $p > 0.05$).

3.4.7. Modeling results indicate spike are initiated in a single compartment only

The previous results illustrate that spikes are generated electrotonically distal to the soma, but do not address the number of independent spike initiation sites. Therefore, we employed a compartmental model of the AII (the "stylized" AII, constrained by our previous experiments; see Sect. 3.3.5) to examine how the activity of one or more distal initiation sites would be reflected in somatic responses. Stylized AIIs were subjected to the same current injections and voltage steps that were applied experimentally (Fig. 3.10A), and simulated and recorded responses were compared.

Notably, four fundamental revisions were done to the previous Na/K_A AII model to produce the stylized AII (among other changes; see Sect. 3.3.5). First, a distal M-type K conductance, as constrained by the previous experimental data, was incorporated. Second, the AII morphology was simplified in order to facilitate the interpretation of model output. Third and fourth, the morphology was increased in surface area and Na kinetics were sped up; these final two revisions were critical for capturing the superposing nature of AII spikes (see below).

Simulated responses from a model with a single initiation site reproduced the features of spiking seen experimentally (Fig. 3.10B): voltage steps evoked repetitive, stereotyped action currents, and current injections elicited bursts of superposing spikes with the inter-spike interval exhibiting a clear refractory nature. A model with two initiation sites, however, failed to recapitulate the experimental data (Fig. 3.10C). Specifically, action currents and spikes exhibited haphazard superposition and the refractory period between spikes was eliminated.

The presence of two initiation sites in parallel was readily exposed by the voltage-clamp protocol within the model (Fig. 3.11A). For example, introduction of very weak heterogeneity (DC bias current of -0.1 pA at one initiation site; causing ~0.1 mV sustained hyperpolarization)

produced spikes from the two sites that could not be readily differentiated at the soma in current-clamp; this arose due to interactions between the initiation sites overcoming the weak heterogeneity (Fig. 3.11Aii). However, the voltage-clamp protocol still readily revealed the existence of two sites: a voltage-clamped soma that was interspersed between the two locations prevented interactions and revealed action currents with variable superposition (Fig. 3.11Aiii).

Incorporating additional spiking compartments (> 2) caused the model's predictions to deviate further from the experimental responses (e.g., Fig. 3.10D, three initiation sites). Thus, these simulations attest to the existence of a single, distal spike initiation site.

Finally, we considered the possibility of multiple initiation sites in series within the AII (Fig. 3.11B). The stylized three-compartment AII was supplemented with an additional passive cable (the "distal cable"; length = 30 μm) terminating in a distal varicosity, connected in series with the previous morphology (the "proximal cable"/"proximal varicosity") (Fig. 3.11Bi). The diameter of the passive distal cable was varied to assess the voltage response induced by a spike from the proximal initiation site.

Initially, the distal varicosity was taken to be passive. Due to the small size of the distal varicosity, in conjunction with its sealed end boundary condition, spike-induced responses in the distal varicosity were large even for extremely narrow distal cables. For example, at a diameter of 50 nm, peak responses were ~15 mV in the distal initiation site.

Due to this strong depolarization at this diameter, when a modest amount of Na was incorporated into the distal initiation site ($\bar{g}_{Na} = 20$ mS/cm^2), a spike in the proximal initiation site triggered a spike in the distal initiation site. In order to for the two sites to function relatively independently (and thus, not be equivalently represented by a single compartment), further reductions to the diameter were needed. In particular, we found that the diameter needed

to be decreased to $\leq$ 25 nm to begin to prevent a proximally-initiated event from evoking a near-immediate distal event (Fig. 3.11Biii). This requirement of an incredibly small diameter, in conjunction with a relatively long length, make it very unlikely that this neurite could exist in a physiological setting; indeed, this diameter is far below values found in EM reconstructions from AIIs in rabbit (J. Anderson, personal communication).

To understand how spikes from a single initiation site transformed and superposed in current-clamp recordings, we tracked the propagation of a single spike across the model AII membrane (Fig. 3.10E). We found that the somatic response was a highly-filtered representation of the fast, distally-initiated spike: as the spike arrived at the soma its waveform was attenuated and broadened, acting to conceal the initiation site AHP and recovery. As the somatic potential did not reflect the recovery dynamics at the initiation site, rapid distal firing events from a single site could produce superposing waveforms at the soma.

Why did the stylized AII model capture superposing spikes, while the Na/K_A model did not? This critical behavior emerged due to two important revisions in the stylized model; namely, a larger surface area (while maintaining a comparable somatic input resistance to the Na/K_A model; see Sect. 3.3.5) and faster Na kinetics. Both of these changes helped to produce spike-induced axial currents at the soma that were briefer than the somatic time constant itself, the key requirement for spike superposition. As the Na/K_A model had spike durations at the initiation site that were similar to that at the soma (Fig. 3.4Bii,iii), this previous model was incapable of producing spike superposition from a single site.

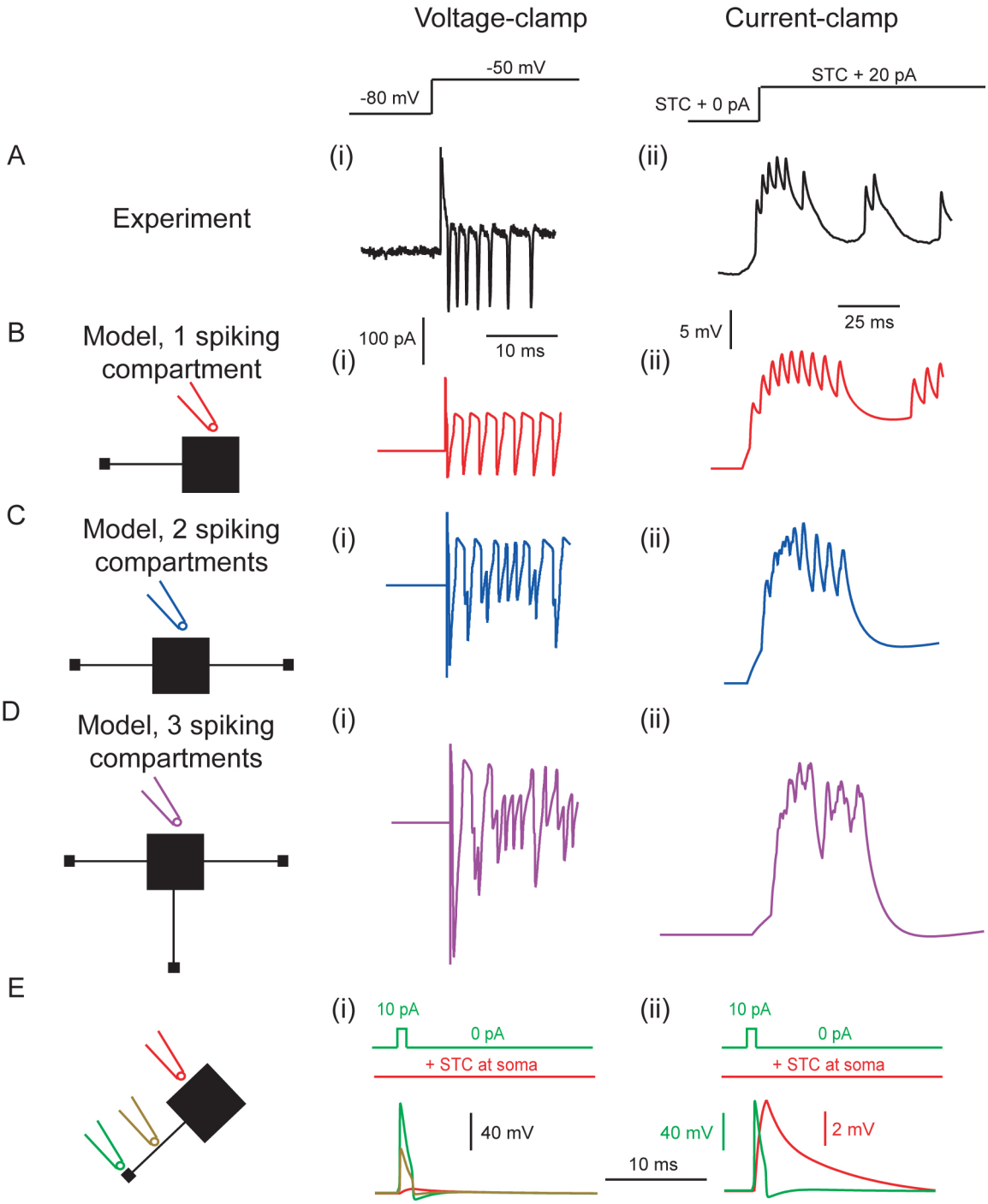
Voltage-clamp
Current-clamp
-50 mV
-80 mV
STC + 20 pA
STC + 0 pA
A
Experiment
(i)
(ii)
B
Model, 1 spiking compartment
100 pA
10 ms
5 mV
25 ms
C
Model, 2 spiking compartments
D
Model, 3 spiking compartments
E
10 pA
0 pA
+ STC at soma
40 mV
10 ms
2 mV

Figure 3.10. A computational model captures properties of experimentally-observed spiking only when a single initiation site is present

A. In experiments (*i*), spiking in an AII was induced by suprathreshold steps in different recording configurations. Representative responses are shown to a suprathreshold step from -80 mV to -50 mV in voltage-clamp (*ii*) and to a suprathreshold 20 pA step in current-clamp (*iii*). B. The morphology of a three-compartment AII model with a single initiation site is shown (not to scale; see Sect. 3.3.5) (*i*). With this model, the features of spiking were captured in both simulated voltage-clamp (*ii*) and current-clamp (*iii*) configurations. C. Simulations are the same as in (B) with an added second initiation site (*i*). This produced simulated somatic recordings which were disorganized and inconsistent with experimental results in both voltage-clamp (*ii*) and current-clamp (*iii*). D. Simulations are the same as in (B,C), except with three initiation sites. With the addition of a third site, the shortcoming of multiple initiation sites became more pronounced. E. A single dendritic spike was evoked by applying a 1 ms, 10 pA current pulse at the initiation site to the model cell, which was otherwise kept from firing via STC injection at the soma. The voltages across the AII compartments are shown (*i*), as well as an expanded view of the somatic response relative to the initiation site response to illustrate the change in time course (*ii*).

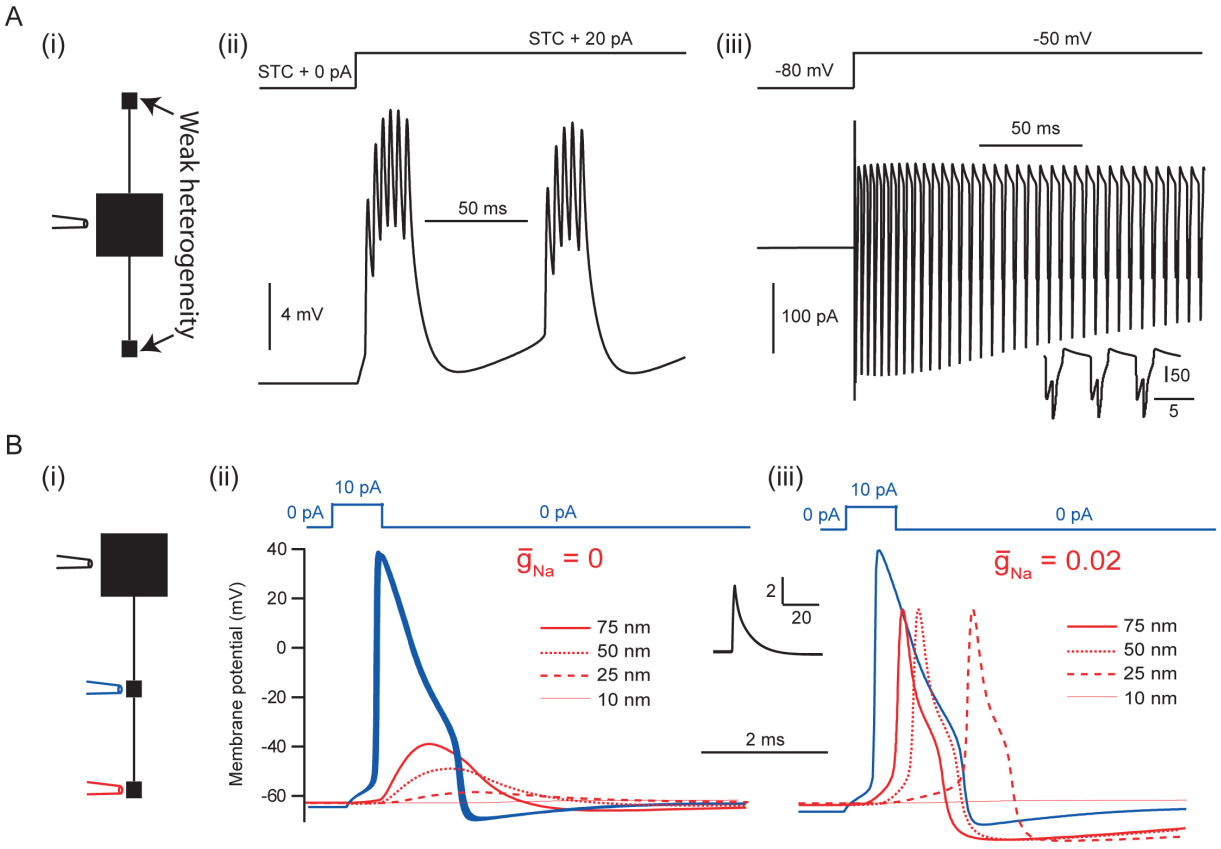
A
(i)
Weak heterogeneity
(ii)
STC + 0 pA
STC + 20 pA
50 ms
4 mV
(iii)
-80 mV
-50 mV
50 ms
100 pA
50
5
B
(i)
(ii)
10 pA
0 pA
0 pA
$\bar{g}_{Na}$ = 0
75 nm
50 nm
25 nm
10 nm
Membrane potential (mV)
40
20
0
-20
-40
-60
2
20
2 ms
(iii)
10 pA
0 pA
0 pA
$\bar{g}_{Na}$ = 0.02
75 nm
50 nm
25 nm
10 nm

Figure 3.11. Additional simulations support the functional equivalent of a single, distal initiation site only.
A*i*. Simulations are shown for a model with two initiation sites and very weak heterogeneity (-0.1 pA DC current at one initiation site). *ii.* This model produced somatically-recorded spikes in current-clamp that appeared to emerge from one initiation site. *iii.* When recorded in voltage-clamp configuration, the voltage-clamped soma prevented interaction between the two sites and revealed their existence. Inset: an expansion of the response ~200 ms after the voltage step. B. The presence of two initiation sites in series is unlikely to occur in the AII. *i.* A stylized model with two initiation sites is shown, with recordings sites illustrated. *ii.* Responses to a proximally-initiated spike are illustrated when the distal varicosity lacked voltage-gated Na channels. Four responses in the model are overlaid as a function of the diameter of the distal cable. Diameters are provided in the legend. *iii.* Responses when voltage-gated Na channels are present in the distal initiation site at a low density ($\bar{g}_{Na} = 0.02$ S/cm^2). Proximally-initiated spikes tended to evoke distally-initiated firing, except when distal cable diameters were unphysiologically small. In this figure, only one proximal initiation site trace is included for comparison. Insert, black: the somatic responses for all simulations are overlaid; at this resolution, there is no difference in responses across the diameters shown in both *ii* and *iii*.

3.4.8. The stylized model AII captures and elucidates experimental recordings

Having verified that the stylized AII model with one initiation site could capture basic properties of AII spiking, we confirmed the robustness of this model by simulating the experiments of Figures 3.3, 3.6-3.8 and used the model to gain mechanistic insight into these results.

First, we found that the stylized AII exhibited bursts with superposing spikes just depolarized to spike threshold, whereas tonic spiking occurred at more elevated potentials (Fig. 3.12A, cf. Fig. 3.3). Bursting arose from rapid firing being gradually overwhelmed by recruitment of the slow K conductance; tonic firing occurred at more depolarized potentials when the slow K conductance could not suppress spiking completely (Fig. 3.13, A-D).

Second, simulating the antagonism of K channels recapitulated experimental results (Fig. 3.12B, cf. Fig . 3.6). A 75% reduction in the A-type K conductance, mimicking application of 2 mM TEA (Tian et al., 2010), produced a small increase in initial spike height. Moreover, this A-type K reduction also produced a perturbed burst waveform similar to that seen in experiments; inspection of the initiation site voltage indicated that this arose due to a filtered version of impaired recovery at the initiation site (Fig. 3.13, E-F). Conversely, reducing or completely eliminating the slow K conductance did not change the initial spike height.

Third, the stylized AII model captured the transient TTX-sensitive after-potentials (Fig. 3.12C, cf. Fig. 3.7), which emerged from the difference in kinetics between fast Na and slow K channels. After-depolarizations occurred because the Na conductance activated more quickly than the slow K conductance following return from hyperpolarization; after-hyperpolarizations occurred because the slow K conductance deactivated slowly upon return from depolarization.

Fourth, the model captured LP-, XE-, and Ba-induced prolongation of bursts (Fig. 3.12D, cf. Figs. 3.8, 3.9). At intermediate reductions in slow K density, bursts were prolonged but still terminated; for larger reductions in density, the burst mode was eliminated altogether and the model AII exhibited only tonic spiking.

We sought to investigate this transition between bursting and tonic spiking more closely by monitoring both the somatic voltage and the activation level of slow K while the density of slow K was slowly stepped (Fig. 3.14). First, we initialized the density of slow K to be 15 mS/cm^2 and applied a large (~32 pA) hyperpolarizing current to the AII soma: this placed the model cell in a tonic spike mode just above the threshold for bursting. Next, we slowly increased the density of slow K within the model (step increases of 0.1 mS/cm^2 every 2 sec), producing a gradual hyperpolarization of the AII. Following each density increase, small

damped oscillations were observed in both the slow K activation and the somatic membrane potential.

The long duration of each density step, relative to the timescale of decaying oscillations following each step, allowed us to identify the density step where the bifurcation occurred: at a density increase of $\Delta\bar{g}_S$ = 0.9 mS/cm^2, the AII transitioned from tonic spiking to bursting (Fig. 3.14A,B). During this transition, the slow K activation exhibited growing oscillations with an exponential envelope; these oscillations had a frequency similar to the damped oscillations below the bifurcation point. After increasing slow K density sufficiently to cause bursting to emerge, we then decreased the density in steps in an analogous fashion. The return to tonic spiking exhibited hysteresis, requiring substantially further reduction in slow K density to leave the burst mode (Fig. 3.14A, transition from bursting to tonic firing occurred at $\Delta\bar{g}_S$ = -0.5 mS/cm^2). These observations demonstrated a bistability between the two firing modes of the AII and suggest that the transition from tonic spiking to bursting occurred via a subcritical Hopf bifurcation.

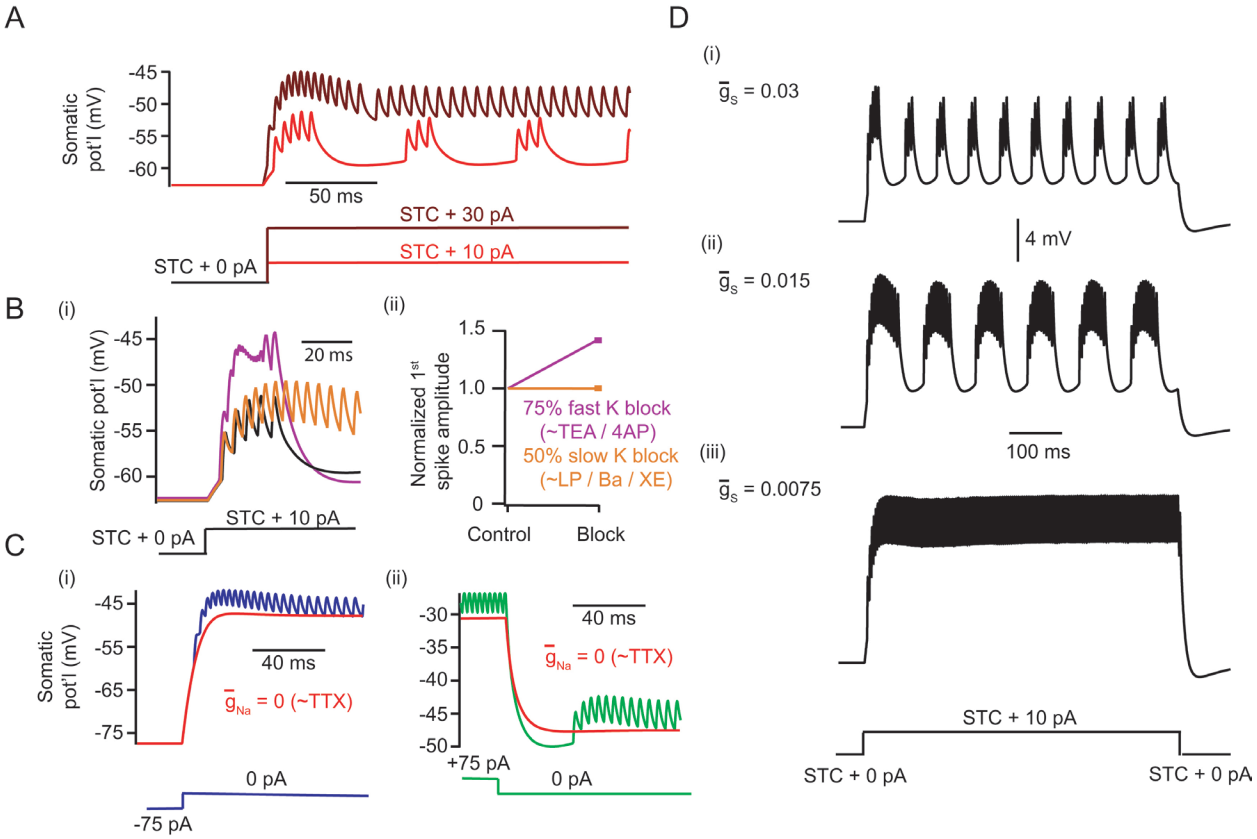

Figure 3.12. The simple AII model captures many experimental features

A. Somatic responses to small (10 pA) and large (30 pA) current steps following STC showed bursting and tonic firing, respectively. B. Somatic voltage traces following K channel reduction, simulating the effects of TEA/4AP and LP/Ba/XE application. Results are shown for control (black), for a 75% reduction of fast A-type K density (purple, 143% initial spike height relative to control), and for a 50% reduction of slow K density (gold, 100% initial spike height relative to control). C. Somatic voltages following large depolarizing (*i*) or hyperpolarizing (*ii*) current offsets are illustrated. After-hyperpolarizations and after-depolarizations were present and greatly reduced by eliminating Na from the model (red). D. Changes in burst duration evoked by reductions in slow K density. In control conditions (slow K density $\overline{g}_S$ = 0.03 at initiation site), 3 spikes/burst occurred. Reducing this density to 0.015 prolonged burst durations (*ii*, 11 spikes/burst), whereas further reduction to 0.0075 produced tonic spiking (*iii*).

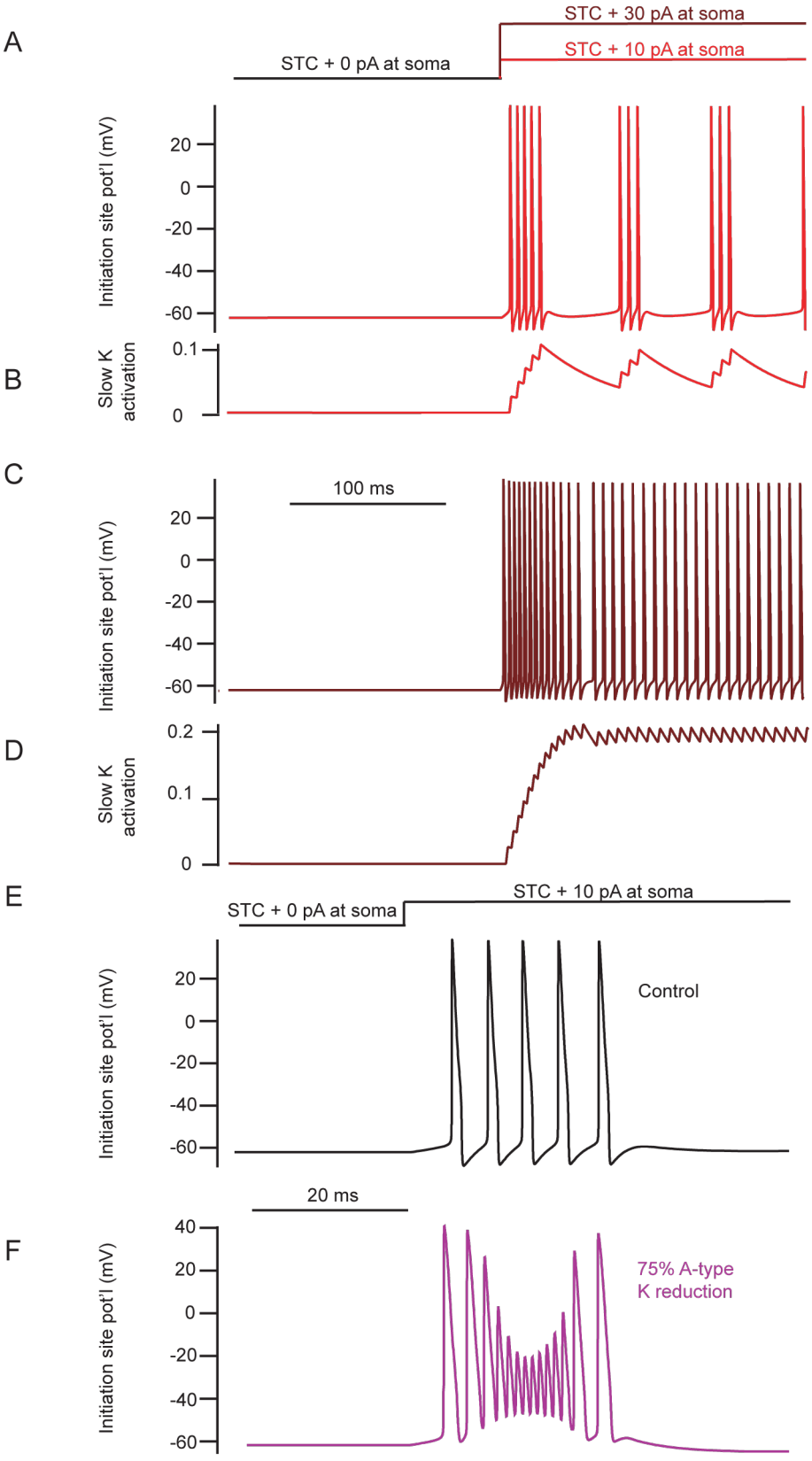
A
STC + 30 pA at soma
STC + 10 pA at soma
STC + 0 pA at soma
Initiation site pot'l (mV)
20
0
-20
-40
-60
B
Slow K activation
0.1
0
C
100 ms
Initiation site pot'l (mV)
20
0
-20
-40
-60
D
Slow K activation
0.2
0.1
0
E
STC + 0 pA at soma
STC + 10 pA at soma
Initiation site pot'l (mV)
20
0
-20
-40
-60
Control
F
20 ms
Initiation site pot'l (mV)
40
20
0
-20
-40
-60
75% A-type
K reduction

Figure 3.13. Examining the membrane potential and slow K activation at the initiation site provides mechanistic insight into experimental results

A. During burst firing, a series of spikes resembling action potentials were evoked at the initiation site in the model AII. B. Each spike activated a fraction of slow K, eventually halting bursting and producing a transient suppression of firing. C. When the soma was further depolarized through a larger current injection, slow K could not completely suppress spiking; rather, a transient period of high-frequency burst-like firing emerged followed by tonic spiking. D. Slow K activation increased initially during the burst-like episode then varied around a steady level during tonic firing. E. Spiking at the initiation site in control conditions, following a current step at the soma. F. Spiking at the initiation site following a 75% reduction in A-type K density. Recovery was inhibited, producing smaller amplitude spikes in rapid succession. The delayed activation of slow K eventually aided in repolarizing the initiation site and enhanced recovery.

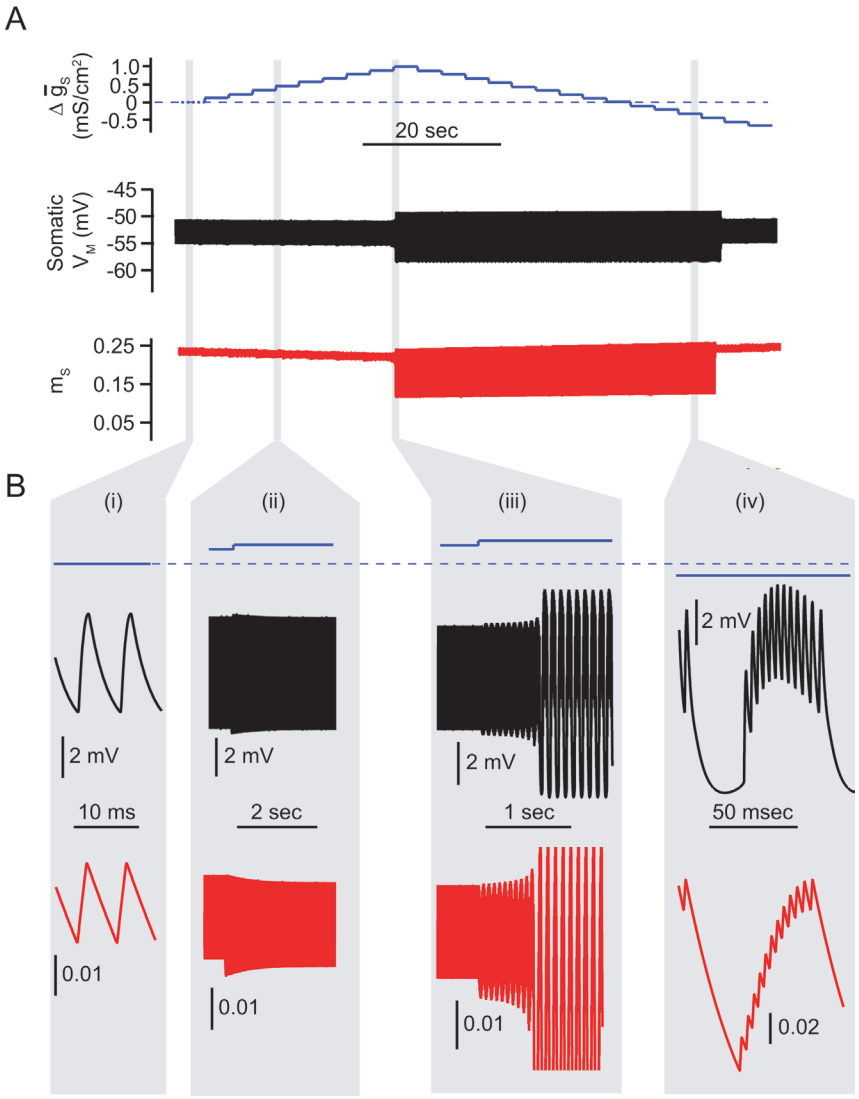
A
Δ ḡS (mS/cm²)
1.0
0.5
0
-0.5
20 sec
Somatic VM (mV)
-45
-50
-55
-60
mS
0.25
0.15
0.05
B
(i)
(ii)
(iii)
(iv)
2 mV
2 mV
2 mV
2 mV
10 ms
2 sec
1 sec
50 msec
0.01
0.01
0.01
0.02

Figure 3.14. The model AII appears to undergo a subcritical Hopf bifurcation when slow K density is increased.
A. The density of the slow K was increased in step increments (blue) to a maximum of $\Delta\bar{g}_S$ = 0.9 mS/cm^2. This produced a gradual hyperpolarization of the AII (black), eventually causing it to go into burst firing. The activation of slow K, m_S, is also illustrated (red). After entering the burst mode, the transition back to tonic firing exhibited hyteresis, occurring at $\Delta\bar{g}_S$ = -0.5 mS/cm^2. B. Expansions of the four labeled components in A: tonic firing was initially present (i); after step increments in slow K, the illustrated variables underwent damped oscillations (ii); upon a step to $\Delta\bar{g}_S$ = 0.9 mS/cm^2, the firing mode underwent a bifurcation and exhibited a growing exponential envelope (iii); after the bifurcation, burst firing was present (iv).

3.4.9. Experimental evidence for a single, distal initiation site

Our model neuron with a single initiation site reproduced the experimental data well, and we therefore sought to verify the existence of such a site experimentally. Working with the Singer Laboratory and the Li Laboratory, this was investigated in three different ways.

One, in collaboration with the Singer Laboratory, TTX was applied locally to individual neurites visualized after filling recording AIIs with a fluorescent tracer (see Cembrowski et al., 2011). A single process was targeted that appeared to be distinct from the dendritic arbor; in some cases, this neurite could be observed clearly extending away for some distance from its origin on the primary dendrite (Fig. 3.15Ai, arrow) (see also Wu et al., 2011). Local application of TTX (50 nM) to the distal termini of these neurites suppressed or completely eliminated spikes recorded at the somata (Fig. 3.15Aiv). In contrast, application of TTX to other portions of the dendritic tree, including compartments as close as 10-20 μm to the distal termini, had noticeably weaker effects (Fig. 3.15Aii-iv). In particular, in every cell tested, the strongest suppression of spiking was observed following application of TTX to the distal terminus. It is notable that in some instances, this terminus was physically well-separated from the remainder of

the neuron (eg, Fig. 3.15Ai), likely minimizing TTX exposure to the vast majority of the AII membrane.

Two, also in collaboration with the Singer Laboratory, the distal portion of the target neurite was removed in order to demonstrate that its presence was required for spike initiation. While recording spikes with a somatic recording pipette containing a fluorescent tracer, the visualized neurite was drawn into a second pipette and pulled away from the cell. After removing the distal portion of this neurite, spiking was completely abolished in the AII (Fig. 3.15Bi; n=7). Importantly, this occurred despite peak ramp currents typically inducing depolarizations >20 mV above the previous V_{thres} (Fig. 3.16).

This loss of spiking was likely not due to deterioration of cell health. In a subset of cells from the previous protocol (n=2), prior to removing the putative initiation site neurites were excised without affecting spiking (filled symbols, Fig. 13.5Biii). Moreover, in a separate group of cells (outlined symbols, Fig. 13.5Bii,iii; n=3), removing non-initiation site neurites did not affect spiking. Thus, the removal of the distal portion of a single and specific neurite was sufficient to eliminate spiking in the AII.

Three, if spiking is indeed initiated at a single site on the AII morphology before propagating passively toward the soma, it would be expected that Na channel expression also would be concentrated at a single site. Therefore, in collaboration with the Li Laboratory, immunohistochemistry was used to examine the localization of Na channels and the Na channel-binding protein ankyrin-G on AIIs: retinae in which AIIs express GFP under the control of the Fbxo32 promoter (Gong et al., 2003; Siegert et al., 2009) (Fig. 3.15C) were incubated with antibodies against GFP, ankyrin-G, and Na channels (see Cembrowski et al., 2011). In tranverse sections, it was found that anti-Na channel and anti-ankyrin-G antibody labeling was colocalized

and restricted to individual neurites like those studied electrophysiologically (Fig. 3.15Cii). These processes were examined in more detail in retinal whole mounts: GFP-expressing neurites exhibiting ankyrin-G expression clearly extended from the proximal portions of individual AIIs (Fig. 3.15Ciii; note the anti-Na channel antibody was not used in whole mount experiments because it generated more non-specific (background) signal than the anti-ankyrin-G antibody). These results are consistent with a recent report (Wu et al., 2011) and bolster our electrophysiological and computational evidence for a single, distal site underlying spiking.

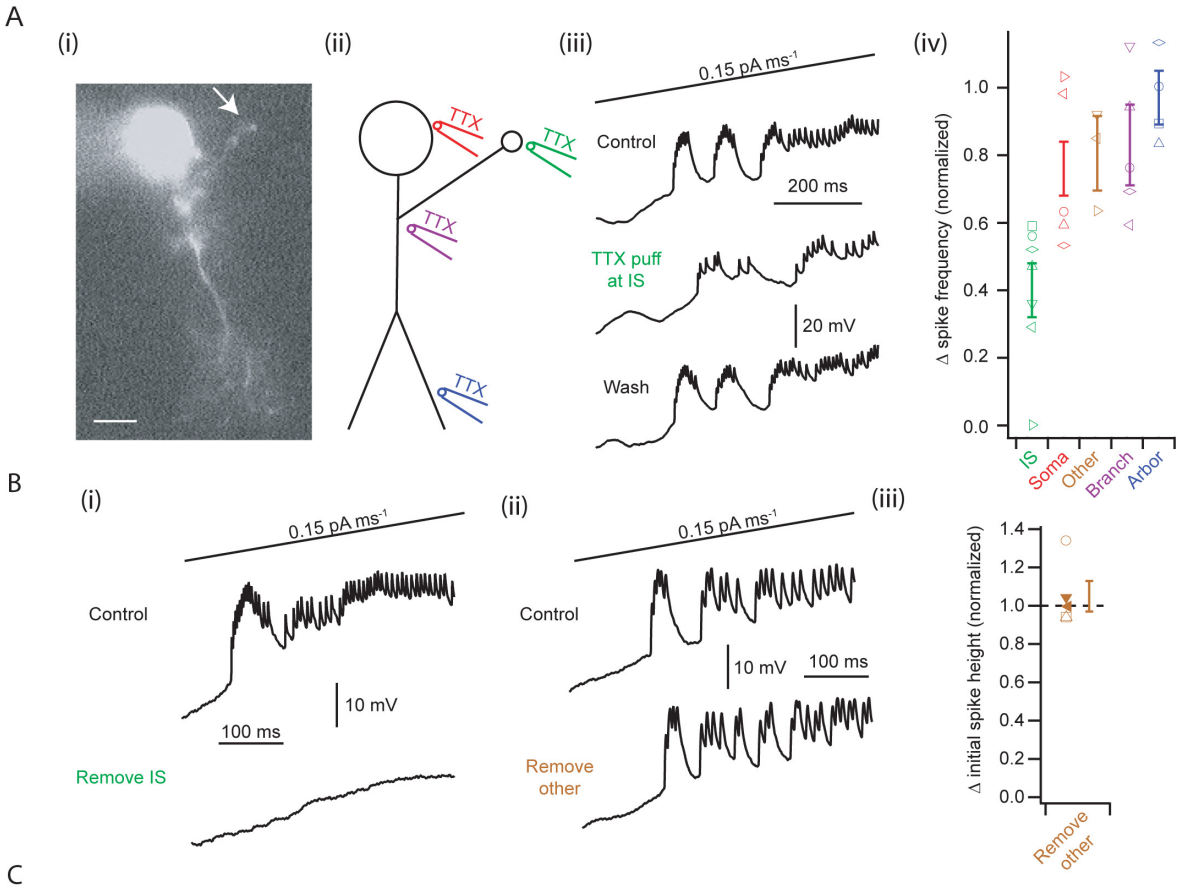
A
(i)
(ii)
(iii)
(iv)
TTX
TTX
TTX
TTX
0.15 pA ms-1
Control
200 ms
TTX puff at IS
20 mV
Wash
Δ spike frequency (normalized)
1.0
0.8
0.6
0.4
0.2
0.0
IS
Soma
Other
Branch
Arbor
B
(i)
(ii)
(iii)
0.15 pA ms-1
Control
10 mV
100 ms
Remove IS
0.15 pA ms-1
Control
10 mV
100 ms
Remove other
Δ initial spike height (normalized)
1.4
1.2
1.0
0.8
0.6
0.4
0.2
0.0
Remove other

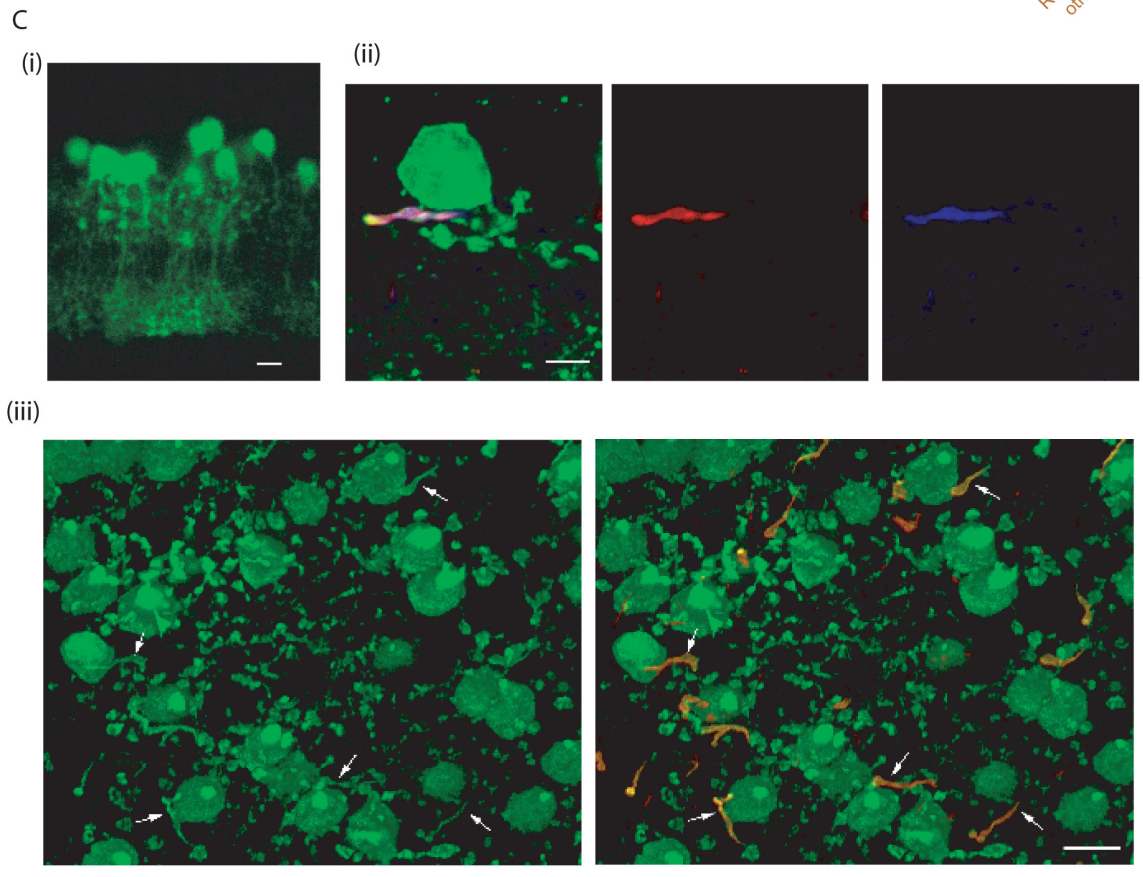
C
(i)
(ii)
(iii)

Figure 3.15. Experimental evidence for a single, distal initiation site.
A. Responses following local TTX applications. (i) A filled AII showed a single, asymmetric neurite terminating in a potential initiation site (arrow). Scale bar = 5 μm. (ii) Schematic illustrating puff locations. (iii) During a slow current ramp (-75 pA to 75 pA at 0.15 pA/ms), spiking was suppressed in the AII following local application of TTX to the putative initiation site. Spike rates recovered after ~1 minute. (iv) Summary of the reduction in normalized spike frequency following local application of TTX (normalized change in frequency following application: initiation site "IS": 0.40±0.08, n=7; soma: 0.76±0.12, n=5; other (see Cembrowski et al., 2011): 0.80±0.10, n=3; branch: 0.83±0.11, n=5; arbor: 0.97±0.08, n=4). B. Responses following neurite excision. (i) Following excision of the putative initiation site, the AII became quiescent (current ramp as in Aii). (ii) In a separate AII, example responses are shown when a non-spiking neurite was removed. (iii) Summary of the normalized change in initial spike height following removal of non-spiking neurites (post-removal = 105 ± 8% of control, n=5; $p > 0.05$). C. (i) A confocal image of a transverse, *in vitro* slice preparation of the Fbxo32-GFP retina revealed GFP fluorescence confined largely to neurons with the distinct morphology of AIIs. Scale bar = 5 μm. (ii). In a transverse section of retina, a GFP-expressing AII (green) was labeled with antibodies against ankyrin-G (red) and Na channels (pan-Na; blue). The Na channels and ankyrin-G were co-localized in a single process that appeared to extend from the AII's primary dendrite. Scale bar = 5 μm. C. In a retinal whole-mount, GFP-expressing AII somata and dendrites were visualized (green). GFP-positive processes that were clearly connected to AIIs (arrows) expressed ankyrin-G (red). Scale bar = 10 μm.

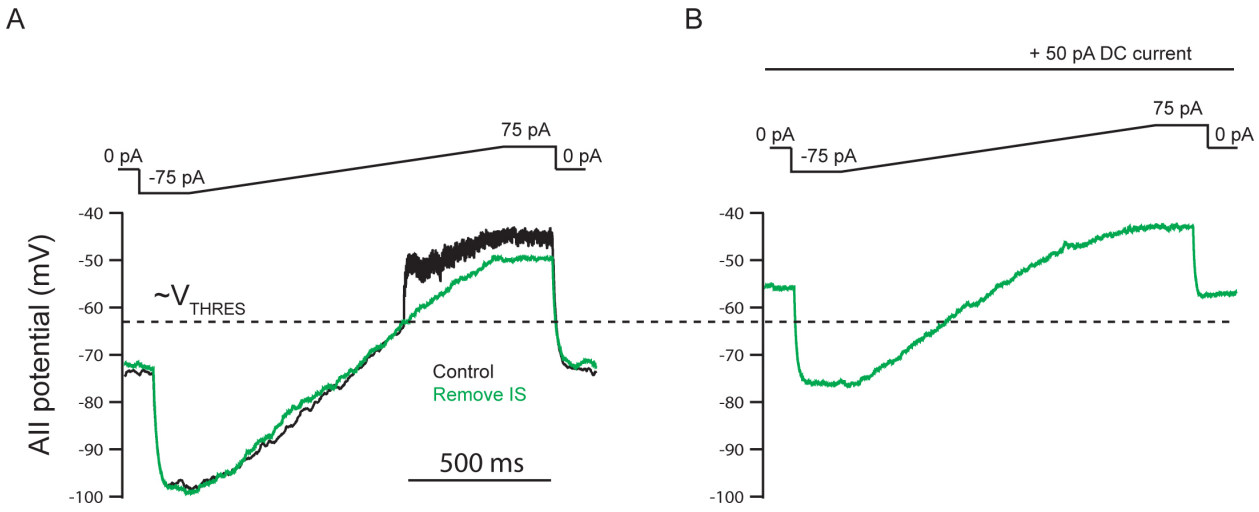

Figure 3.16. Removing the initiation site silences spiking over all potentials tested
A. Example traces, displayed over the full duration of the current ramp, before and after removing the putative initiation site. B. After removing the initiation site, depolarizing the AII by adding an additional 50 pA of DC current failed to elicit any spikes.
In both A and B, a subthreshold current (STC) of -50 pA was also applied.

3.4.10. A morphologically-realistic model reproduces experimental results

Having described the dendritic compartment constituting the spike initiation site, we thought it important to extend our inquiries beyond a three-compartment model and to verify that a model with a realistic morphology (the "complete" model) captured the experimental results. An AII was filled and imaged (see Sect. 3.3.7), revealing the presence of a long cable branching asymmetrically from the primary dendrite (Fig. 3.17A; arrow: putative initiation site). Based on this imaged AII, the complete model produced attenuation between the initiation site and soma similar to that generated by the three-compartment AII (Fig. 3.17B,C; cf. Fig. 3.10D). Additionally, the complete model generated the dual modes of firing seen experimentally and in the simple model (Fig. 3.17D; cf. Figs. 3.3,3.11A).

Importantly, this model illustrated that the extent of attenuation was very similar at the soma, lobular appendages, and arboreal dendrite (Fig. 3.17C). Therefore, the reduction of the morphologically-complex AII into a simple stylized model is justified when considering spike dynamics. In addition, this finding suggests that spike heights are similar at the physically separated locations where AIIs contact ON and OFF cone bipolar cells (via electrical and chemical synapses, respectively).

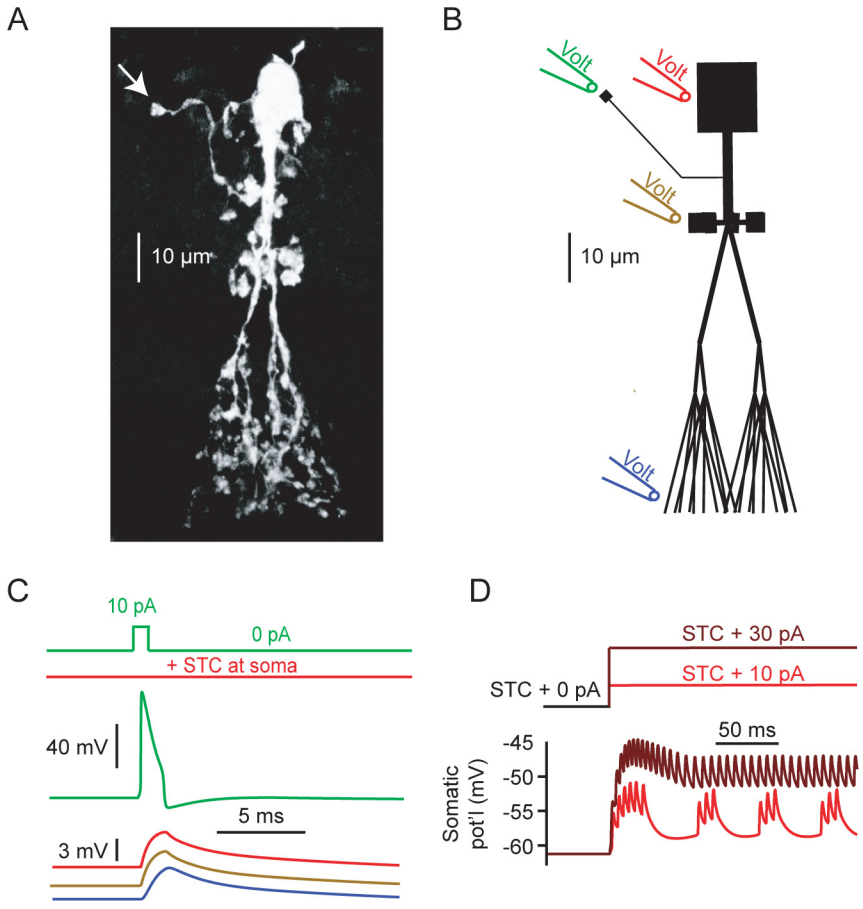

Figure 3.17. The complete model behaves similarly to the reduced three-compartment stylized model and captures experimental responses.
A. A confocal reconstruction of an individual AII. A long, unbranched cable with a putative initiation site was present (arrow). B. The "complete" AII model, with respective recording locations illustrated. C. A single dendritic spike was evoked in the model AII by applying a 1 ms, 10 pA current pulse at the initiation site, which was otherwise kept from firing via STC injection at the soma (cf. Fig. 3.11D). The spike attenuated significantly as it propagated towards the primary dendrite. After reaching this neurite, however, voltage responses were similar at the soma, lobular appendages, and distal dendritic arbor (traces offset for clarity). D. The complete morphological model exhibited both burst and tonic firing.

3.4.11. Weak RB input is unlikely to synchronize AIIs

The previous results show that AIIs have a single excitable neurite that is electrically isolated from the majority of the membrane. Due to this electrotonic structure, there is the potential that the timing of firing in an oscillating AII might be very sensitive to the location of input; in particular, AIIs oscillating out of phase might be synchronized by inputs occurring at the initiation site.

To investigate this, we examined the phase shift induced by a mEPSP occurring at either the soma or the initiation site (see Sect. 3.3.10) in a bursting AII near threshold (period ~68 ms). The measurement of the phase shift was taken ~2 seconds after the initial perturbation to allow the stimulated AII to tend to the limit cycle trajectory. To construct a phase resetting curve (PRC) (Izhikevich, 2007), we employed 69 trials for each input location, with inputs on successive trials delayed by 1 ms relative to the previous trial. A stimulus phase of zero was defined to be at the initiation of the first spike in a burst.

First, we evoked individual mEPSPs at the initiation site (Fig. 3.18A). Due to the high input impedance of this neurite, these events produced a large local voltage excursion that usually led to the initiation of a spike. In turn, this produced a range of refractory periods that depended on whether the induced spike caused the subsequent initiation of a burst. This led to a PRC that seemed to exhibit discontinuities, although it is likely that this is an artifact of our limited 1 ms resolution.

Second, in a similar fashion we delivered individual mEPSPs to the soma (Fig. 3.18B). Somatically-occurring mEPSPs had much less of a tendency to induce spikes, as would be expected from filtering occurring across the stylized AII morphology in conjunction with the the lower input impedance of the soma. Nevertheless, the ensuing PRC still showed jump-like behavior when input led to the initiation of an additional spike.

For both the soma and initiation site, the steepness of the PRC illustrated that small changes in the timing of the input could produce large differences in the phase shift, depending on the phase of the AII. As release from RBs can exhibit substantial jitter in the timing of events (Jarsky et al., 2010; Tian et al., 2010), it would seem that mini RB input is not a reliable way to synchronize oscillatory AIIs. Of course, a caveat of our results is that they were calculated for only one type of input, and different types of RB inputs may produce PRCs that better facilitate synchronization; however, we did not investigate this further.

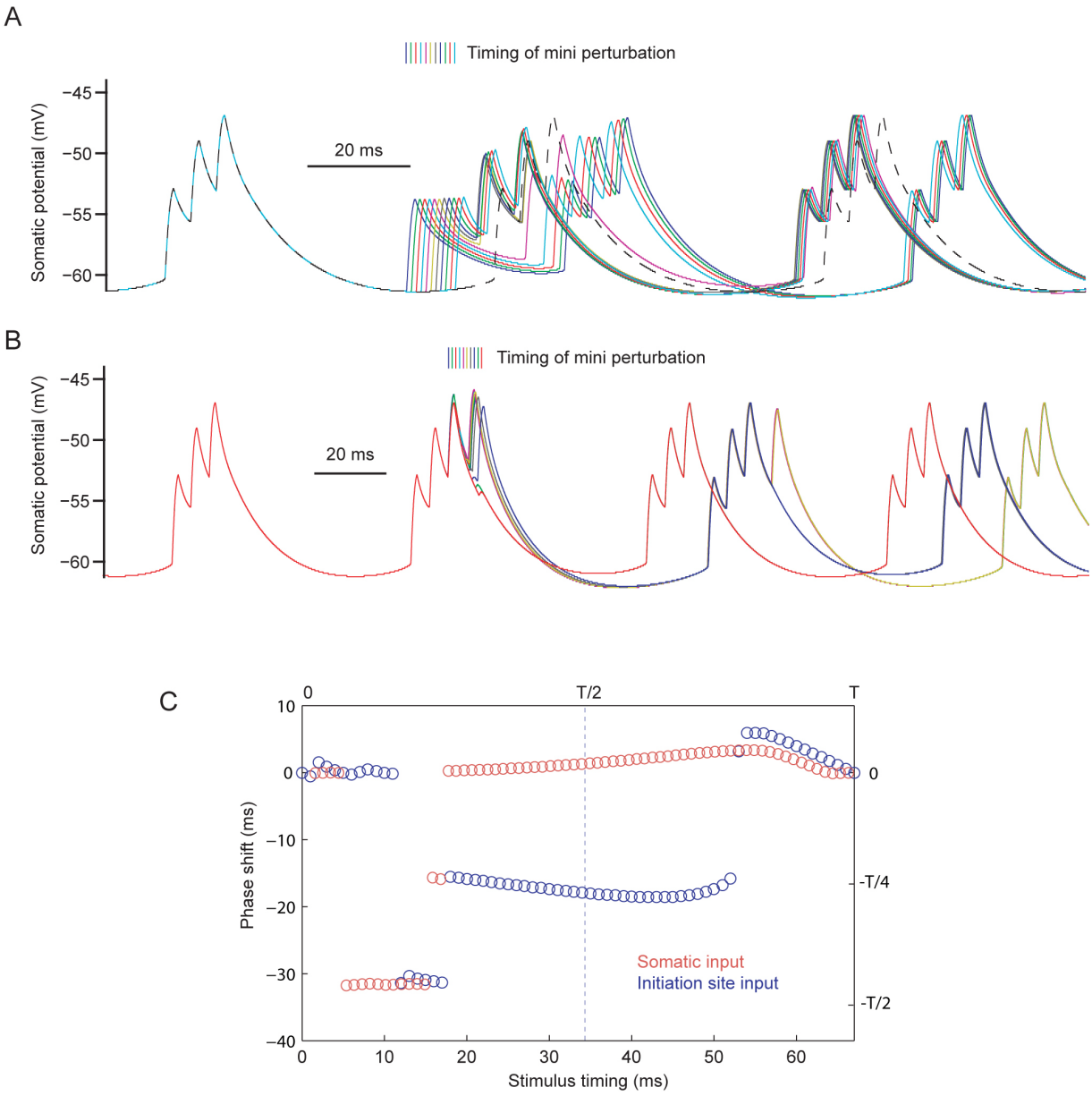
A
Timing of mini perturbation
Somatic potential (mV)
−45
−50
−55
−60
20 ms
B
Timing of mini perturbation
Somatic potential (mV)
−45
−50
−55
−60
20 ms
C
0
T/2
T
10
0
−10
−20
−30
−40
Phase shift (ms)
0
-T/4
-T/2
Somatic input
Initiation site input
0
10
20
30
40
50
60
Stimulus timing (ms)

Figure 3.18. Phase response curves following a mEPSP in the stylized model
A. Example responses in the AII are illustrated following the delivery of a single mEPSP to the initiation site at variable times. Here, the dotted line indicates the unperturbed case. B. As in A, but with the mEPSP having been delivered to the soma. C. The PRCs extracted from administering mEPSPs at the initiation site (blue) and at the soma (red).

3.4.12. Voltage-gated Na channels lead to negligible acceleration and amplification of RB input in the model AII

We next sought to investigate how the model AII responded to more physiologically-relevant RB input. We performed this next set of simulations in two steps, using a stochastic version of the RB-AII synapse model of Chapter 2 as well as the stylized AII model.

First, using the RB-AII synapse model, we simulated stochastic release from RBs evoked by physiologically-relevant RB voltages. To drive release, we used experimentally-obtained current-clamp RB responses to brief flashes of light (A. Sampath, personal communication; Fig. 3.19A). These responses were used as command voltages in a stochastic version of the RB-AII synapse model (see Sect. 3.3.11) to simulate the timing of discrete release events from the RB (Fig. 3.19B, top and middle panels).

Second, for a given realization, somatic mEPSPs were evoked in the stylized AII model according to the event times produced by the RB-AII synapse model (see Sect. 3.3.10; Fig. 3.19B, bottom panel). For each realization, the response in the AII was assessed both at rest (Fig. 3.19C, top) as well as when the AII was hyperpolarized (Fig. 3.19C, bottom; see Sect. 3.3.11); these two potentials corresponded to tonic and burst firing, respectively (Fig. 3.19C, left). To assess the contributions from voltage-gated Na channels, each realization in the two conditions was also run with Na channels were removed from the model (Fig. 3.19C, middle;

averaged response to 100 realizations depicted). Responses to realizations in each condition (rest vs. hyperpolarized and with vs. without Na channels) were averaged and compared (Fig. 3.19C, right).

In the tonic spiking regime, we found that Na channels contributed almost no transformation to RB-mediated events over all the flash intensities tested. This input tended to exert little modulation on the firing frequency of the AII and produced almost no amplification or acceleration (Fig. 3.19C, right). When AIIs were hyperpolarized, the increased driving force on the RB events increased the relative amplitudes of AII responses, as would be expected. Voltage-gated Na channels did not tend to enhance these inputs, however, for most flash strengths: very little change in amplitude was seen for stronger inputs, whereas some weak amplification (~10%) and acceleration (3-5 ms) occurred for dim flashes.

Finally, these simulations illustrated that depletion of the RB-AII synapse, rather than the intrinsic properties of the AII itself, acted to sharpen the RB response. The stochastic synapse model suggested that the available pool was typically depleted following the initial large voltage response (Fig. 3.19B), acting to transform the relatively sluggish RB flash input into a shortened response in the AII. We confirmed this by examining EPSCs evoked by simulated flash responses in the mean model of the RB-AII synapse (Chapter 2); as expected, in these simulations AII currents exhibited a much briefer time course than the corresponding RB voltages (Fig. 3.20). The result that AII responses are briefer than the RB voltage responses is consistent with previous experimental work (Snellman et al., 2009; Trexler et al., 2005).

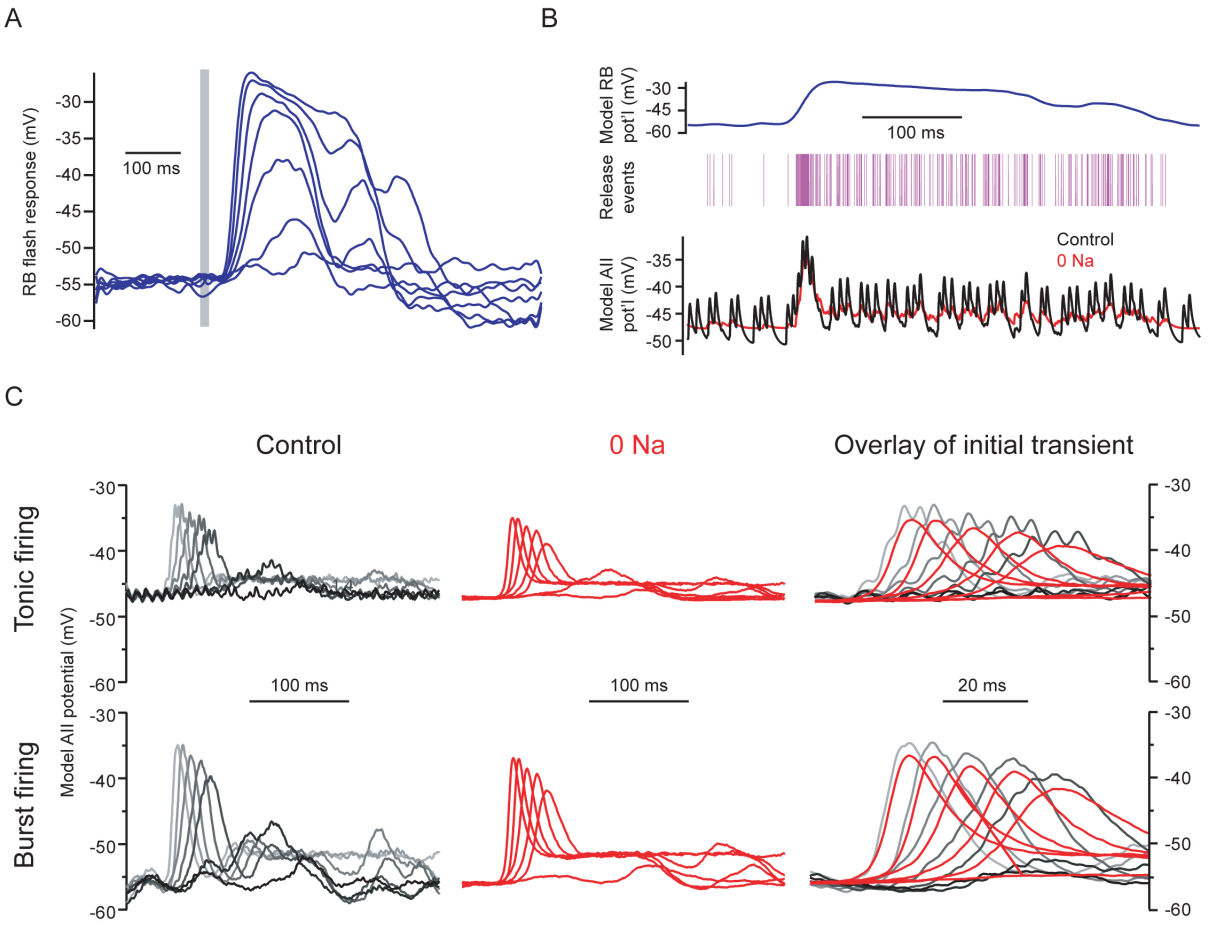
A
RB flash response (mV)
-30
-35
-40
-45
-50
-55
-60
100 ms
B
Model RB pot'l (mV)
-30
-45
-60
100 ms
Release events
Model AII pot'l (mV)
-35
-40
-45
-50
Control
0 Na
C
Control
0 Na
Overlay of initial transient
Tonic firing
Burst firing
Model AII potential (mV)
-30
-40
-50
-60
100 ms
100 ms
20 ms

Figure 3.19. Responses to stochastic RB input in the current-clamped stylized AII

A. In a current-clamped RB, example responses to flashes of different intensities are shown. Experimental data is pictured; in Rh*/rod/s, flash strengths were 0.2, 0.6, 1.4, 2.9, 6.0, 12.2, and 24.4. Peak responses increased monotonically in response to flash strength. Flash timing is denoted by the vertical grey bar. B. Example protocol used to drive the stylized AII model. A flash response was used as the RB command voltage (blue) in a stochastic version of the RB-AII synapse model of Chapter 2. This produced a series of discrete release events (purple) that evoked quantal mEPSPs in the stylized AII model. Responses in the AII were assessed in control conditions (black) and after Na channels were eliminated (red). C. The protocol depicted in B was used to drive the AII at rest (top) and when hyperpolarized (bottom), during which firing was predominantly tonic and bursting, respectively. Averaged responses to 100 stochastic trials were obtained in control conditions (black; left) and without Na channels (red; middle) for each flash intensity. Responses are overlaid at right.

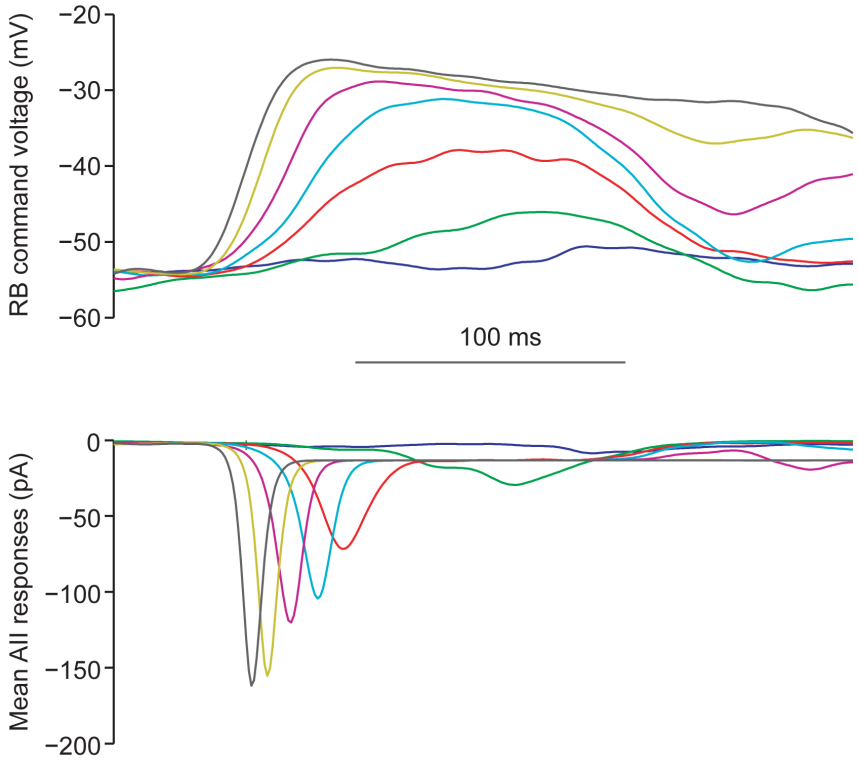

Figure 3.20. Responses to simulated flashes in the mean RB-AII synapse model.
Flash responses in the RB (top) were used to drive release in the mean RB-AII synapse model; this produced EPSCs in the AII that were much briefer than the RB depolarization.

3.4.13. Spiking can increase the spatial extent of signal propagation

Finally, we constructed a network of stylized AIIs coupled via gap junctions (see Sect. 3.3.12, Fig. 3.21A) in order to investigate how input propagated in a network initially hyperpolarized below threshold. To cause the network to rest hyperpolarized, the leak reversal potential was adjusted (see Sect. 3.3.12); within experiments, changes in membrane potential that approximated this effect could be captured by bath-applying L-AP4 to modulate the ON cone bipolar (CB) resting potential (ctrl vs. L-AP4: -43.8 ± 0.6 mV vs. -55.1 ± 1.2 mV; n=4; $p < 0.05$; Fig. 3.21B). Other work has shown that L-AP4 can exert even more pronounced effect by causing the AII to become markedly subthreshold (Tamalu and Watanabe, 2007).

When depolarizing input was injected into a single cell within the network, waves of spiking could be evoked that propagated to neighbouring AIIs. Depending on the properties of the input (say, the duration of depolarizing current step), waves of activity could be produced that remained localized to a subset of AIIs (e.g., Fig. 3.21C, D) or traversed the entire network (Fig. 3.21E). Importantly, this active propagation was much farther than would be expected from nonspiking cells: eliminating Na from the model reduced transmission to levels expected by steady-state coupling alone (~15%, constrained from experimental recordings; data not shown). Without spiking, transmission was effectively eliminated beyond the first postsynaptic cell, suggesting that this intrinsic spiking may play a role in determining the spatial extent of network signaling under certain conditions.

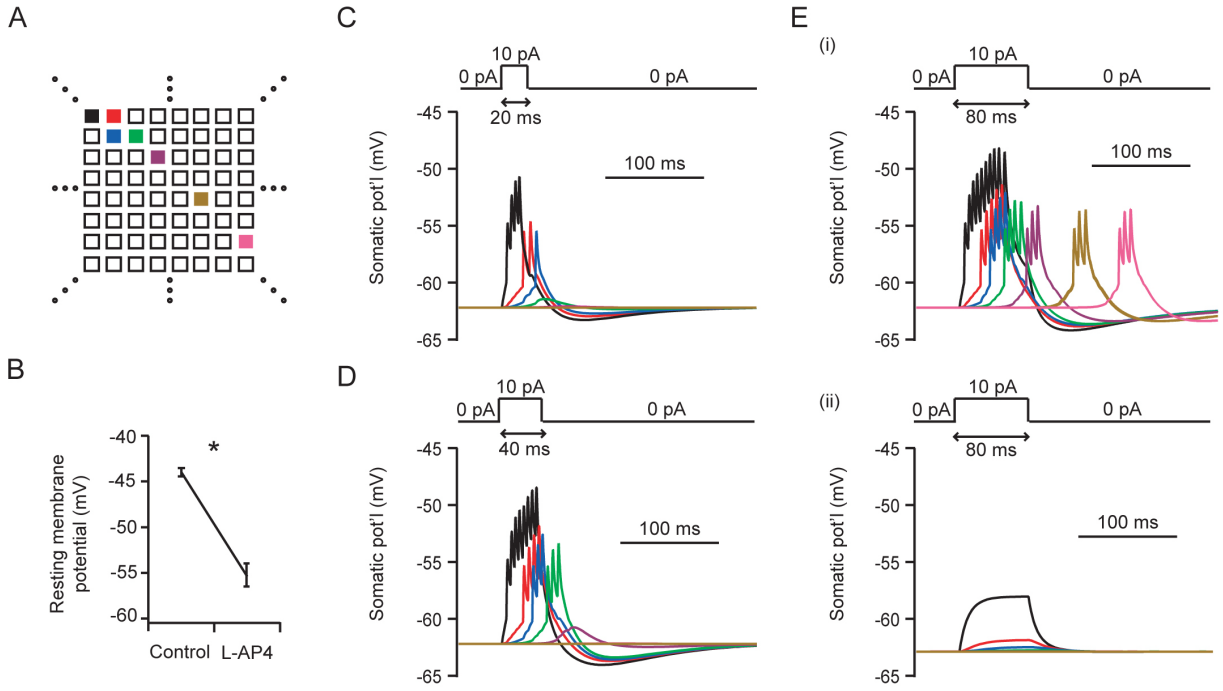

Figure 3.21. Transmission of inputs across the simulated AII network can depend on spiking.
A. Schematic of the network used to study transmission, with each square representing a stylized AII. Colored cells correspond to voltage traces in C-E. B. In experiments, L-AP4 exerted large changes on the resting membrane potential of the AII and placed the AII near spike threshold ($p < 0.05$). C. Responses in the hyperpolarized AII network are depicted following a depolarizing current injection for 20 ms to one AII (black). This produced a wave of activity that failed at the third synapse. D. As in C, but with an injection for 40 ms. This activity failed at the fifth synapse. E. (i) When the current step was taken to be 80 ms, bursts of activity were evoked that traversed the AII network. (ii) After removing Na channels from the AII model, responses were largely confined to the stimulated cell only.

3.5. Discussion

Here, we demonstrated that spikelets recorded in the soma of the axonless AII amacrine cell represent large events generated at a single, electrotonically-distal initiation site. At this dendritic location, a voltage-gated Na conductance appears to be colocalized with a slow M-type K conductance. Spikes generated at this site resemble action potentials that undergo filtering as they propagate to the soma where they are recorded. A morphologically-realistic model suggests the waveform of spikes in the complex dendritic arbor is similar to that at the soma. The AII exhibits an unexpected and interesting electrotonic structure: despite its small size, it contains an electronically remote dendritic compartment that acts like an axon initial segment.

3.5.1. Dual modes of firing in the AII

Shaped by an M-type K conductance, the AII exhibits two firing modes: bursting near threshold and tonic firing at more depolarized potentials. Na channel-mediated amplification of inputs, then, is likely to vary with the resting potential of the AII, as has been demonstrated previously (Tian et al., 2010).

The resting membrane potential of the AII *in vivo* is unknown. Reports of AII resting potentials from experiments *in vitro* vary significantly and do not exhibit a clear dependence on either species or the adaptational state of the retina: -65 mV (dark-adapted mouse, Pang et al., 2004), -59 mV (light-adapted rat, Boos et al., 1993), -50 mV (light-adapted mouse, Tian et al., 2010), -46 mV (dark-adapted mouse, Dunn et al., 2006), -37 mV (dark-adapted mouse, Tamalu and Watanabe, 2007). Although the reason(s) for this variability are unclear, it is notable that

these resting potentials span a voltage range in which both modes of firing can occur. Thus, it is reasonable to expect that the AII might exploit both in a physiological setting.

The AII's resting membrane potential appears to depend on the voltage of coupled ON CBs. It has been shown that application of L-AP4, which hyperpolarizes both rod bipolars (RBs) and ON CBs by agonizing their metabotropic glutamate receptors, also produces large (15-20 mV) hyperpolarizations in AIIs (Tamalu and Watanabe, 2007). The Singer Laboratory has found similar results when transmission from RBs is blocked (data not shown), suggesting that synaptic activity in gap junction-coupled ON CBs can shape the AII resting potential. This arrangement could provide a means by which activity in ON CBs modulates the excitability of AIIs; in particular, hyperpolarized ON CBs could bias AIIs towards bursting in darkness, whereas depolarized ON CBs might induce tonic spiking in brighter scenes.

Bursts may also act as a mechanism to enhance drive to gap junction-coupled cells. Individual spikes in AIIs are heavily filtered across gap junctions and therefore propagate poorly between coupled cells (Veruki and Hartveit, 2002a, b). Superposing spikes, as typically seen in burst waveforms, may provide a way to circumvent this filtering by producing amplified responses that are relatively broad in time. In this way, the mode of firing (burst vs. tonic spiking) may be an important determinant in transmitting Na-mediated events across gap junctions. This could provide a means of modulating the receptive field size of the AII, complementing the plasticity inherent to the AII-AII gap junctions themselves (Bloomfield and Volgyi, 2004; Veruki et al., 2008).

3.5.2. A single initiation site is consistent with published studies

Our proposal that an axonless neuron possesses a dendritic compartment akin to an axon initial segment may appear surprising, but in actuality, it is consistent with previously published studies of AII function. In studies of AIIs' electrical synapses (to both other AIIs and ON CBs), passive transmission of spikes between coupled neurons was observed (Veruki and Hartveit, 2002a, b). This result suggests that spikes are not generated near gap junctions, which are found in the distal dendritic arbor (Strettoi et al., 1992; Tsukamoto et al., 2001). This conclusion is predicted from analysis of our morphologically-realistic model AII, which predicts passive propagation of spiking across the arbor (Fig. 3.17D).

Additional evidence that the spike-generating mechanism is isolated comes from the observation that TTX had equivalent effects on the timing of AII output to the ON and OFF pathways (via gap junctions and inhibitory glycinergic synapses, respectively) (Tian et al., 2010). As gap junctions are located primarily on the distal dendrites, whereas glycinergic presynaptic terminals are found in proximal lobular appendages (Habermann et al., 2003; Strettoi et al., 1992; Tsukamoto et al., 2001), it is likely that active spiking does not occur at or between these sites. This, too, is predicted from our findings.

Finally, the AII's soma also can be excluded as the site of spike initiation as Na currents could not be recorded from these structures (Tian et al., 2010). Na channels, however, have been suggested to be spatially proximal to the soma and proximal dendrite rather than the dendritic arbor (Tamalu and Watanabe, 2007). Our results presented here identify a single location for this conductance: a long neurite which branches asymmetrically from the AII's primary dendrite (Fig. 3.15). This compartment fulfills the requirement that Na channels be relatively close (in a

spatial sense) to the AII soma (Tamalu and Watanabe, 2007), while enabling the initiation site to operate in electrotonic isolation from the soma.

3.5.3. Implications for circuit processing

The AII is a multifunctional neuron that plays important roles in both rod- and cone-mediated vision (Deans et al., 2002; Field et al., 2009; Manookin et al., 2008; Munch et al., 2009; Volgyi et al., 2004). How does the unconventional electrotonic structure of the AII contribute to processing within these various pathways? Based on our finding of an isolated functional spiking zone on a distinct AII process, it is natural to ask whether this process has its own dedicated inputs or outputs. Such strategically placed inputs could control the firing of the cell, and with it, modulate the processing of the other inputs that are distributed across the remainder of the dendrite. At the same time, outputs on the specialized process would likely have characteristics that are quite different from those throughout the remainder of the dendrite as a consequence of direct coupling to spiking.

While such inputs and outputs have not been established functionally, anatomical work using immunohistochemistry (Wu et al., 2011) and EM (Anderson et al., 2011) indicates that they may exist. Moreover, in recordings, weak RB input reliably evoked firing in control conditions but generated almost no somatic response after TTX application (Figure 5 in Tian et al., 2010). This finding is suggestive of some RB inputs being electrotonically close to the spike initiation site, and raises the intriguing possibility that spiking may preferentially amplify scotopic inputs. Thus, an important goal is to determine whether there are indeed functional synaptic contacts that are electrotonically proximal to the AII initiation site, and if so, to what

type(s) of cell(s) it establishes connections. This will provide substantial insight into the contributions of the AII to the visual processing performed by the retinal circuitry.

3.5.4. Concluding remarks

It is interesting to note that, in addition to the AII, two other classes of amacrine cells have been shown to be noncompact. These two cell types exploit different advantages of this electrotonic structure. In the starburst amacrine cell, individual neurites act as independent electrical units to produce direction-selective dendritic calcium signals (Euler et al., 2002). In the A17 amacrine cell, serial dendritic varicosities are separated by thin processes and function in isolation of one another, acting to process signals in parallel while minimizing wiring cost (Grimes et al., 2010). Thus, of the three largest known populations of amacrine cells (Strettoi and Masland, 1996), all have been shown to behave in a noncompact fashion.

References

Adams, P.R., Brown, D.A., and Constanti, A. (1982a). M-currents and other potassium currents in bullfrog sympathetic neurones. J Physiol *330*, 537-572.

Adams, P.R., Brown, D.A., and Constanti, A. (1982b). Pharmacological inhibition of the M-current. J Physiol *332*, 223-262.

Aiken, S.P., Lampe, B.J., Murphy, P.A., and Brown, B.S. (1995). Reduction of spike frequency adaptation and blockade of M-current in rat CA1 pyramidal neurones by linopirdine (DuP 996), a neurotransmitter release enhancer. Br J Pharmacol *115*, 1163-1168.

Anderson, J.R., Jones, B.W., Watt, C.B., Shaw, M.V., Yang, J.H., Demill, D., Lauritzen, J.S., Lin, Y., Rapp, K.D., Mastronarde, D*., et al.* (2011). Exploring the retinal connectome. Mol Vis *17*, 355-379.

Babai, N., Bartoletti, T.M., and Thoreson, W.B. (2010). Calcium regulates vesicle replenishment at the cone ribbon synapse. J Neurosci *30*, 15866-15877.

Baccus, S.A., and Meister, M. (2002). Fast and slow contrast adaptation in retinal circuitry. Neuron *36*, 909-919.

Beaudoin, D.L., Borghuis, B.G., and Demb, J.B. (2007). Cellular basis for contrast gain control over the receptive field center of mammalian retinal ganglion cells. J Neurosci *27*, 2636-2645.

Beaudoin, D.L., Manookin, M.B., and Demb, J.B. (2008). Distinct expressions of contrast gain control in parallel synaptic pathways converging on a retinal ganglion cell. J Physiol *586*, 5487-5502.

Bloomfield, S.A. (1992). Relationship between receptive and dendritic field size of amacrine cells in the rabbit retina. J Neurophysiol *68*, 711-725.

Bloomfield, S.A., and Dacheux, R.F. (2001). Rod vision: pathways and processing in the mammalian retina. Progress in Retinal and Eye Research *20*, 351-384.

Bloomfield, S.A., and Volgyi, B. (2004). Function and plasticity of homologous coupling between AII amacrine cells. Vision Res *44*, 3297-3306.

Bloomfield, S.A., and Xin, D. (2000). Surround inhibition of mammalian AII amacrine cells is generated in the proximal retina. J Physiol *523 Pt 3*, 771-783.

Bloomfield, S.A., Xin, D., and Osborne, T. (1997). Light-induced modulation of coupling between AII amacrine cells in the rabbit retina. Vis Neurosci *14*, 565-576.

Boos, R., Schneider, H., and Wassle, H. (1993). Voltage- and transmitter-gated currents of AII-amacrine cells in a slice preparation of the rat retina. J Neurosci *13*, 2874-2888.

Brown, S.P., and Masland, R.H. (2001). Spatial scale and cellular substrate of contrast adaptation by retinal ganglion cells. Nat Neurosci *4*, 44-51.

Cangiano, L., Gargini, C., Della Santina, L., Demontis, G., and Cervetto, L. (2007). High-pass filtering of input signals by the Ih current in a nonspiking neuron, the retinal rod bipolar cell. PLoS One *2*, e1327-e1327.

Carandini, M., Demb, J.B., Mante, V., Tolhurst, D.J., Dan, Y., Olshausen, B.A., Gallant, J.L., and Rust, N.C. (2005). Do we know what the early visual system does? J Neurosci *25*, 10577-10597.

Casini, G., Rickman, D.W., and Brecha, N.C. (1995). AII amacrine cell population in the rabbit retina: identification by parvalbumin immunoreactivity. J Comp Neurol *356*, 132-142.

Cembrowski, M.S., Logan, S.M., Tian, M., Li, W., Jia, L., Kath, W.L., Riecke, H., and Singer, J.H. (2011). The mechanisms of repetitive spike generation in an axonless retinal interneuron. Submitted, Cell Reports.

Chander, D., and Chichilnisky, E.J. (2001). Adaptation to temporal contrast in primate and salamander retina. J Neurosci *21*, 9904-9916.

Chichilnisky, E.J. (2001). A simple white noise analysis of neuronal light responses. Network *12*, 199-213.

Dacheux, R.F., and Raviola, E. (1986). The rod pathway in the rabbit retina: a depolarizing bipolar and amacrine cell. J Neurosci *6*, 331-345.

Deans, M.R., Gibson, J.R., Sellitto, C., Connors, B.W., and Paul, D.L. (2001). Synchronous activity of inhibitory networks in neocortex requires electrical synapses containing connexin36. Neuron *31*, 477-485.

Deans, M.R., Volgyi, B., Goodenough, D.A., Bloomfield, S.A., and Paul, D.L. (2002). Connexin36 is essential for transmission of rod-mediated visual signals in the mammalian retina. Neuron *36*, 703-712.

Demb, J.B. (2008). Functional circuitry of visual adaptation in the retina. J Physiol *586*, 4377-4384.

Demb, J.B., and von Gersdorff, H. (2008). Ultraweak signals can cause synaptic depression and adaptation. Neuron *57*, 802-804.

Destexhe, A., Rudolph, M., Fellous, J.M., and Sejnowski, T.J. (2001). Fluctuating synaptic conductances recreate in vivo-like activity in neocortical neurons. Neuroscience *107*, 13-24.

Dong, C.J., and Hare, W.A. (2003). Temporal modulation of scotopic visual signals by A17 amacrine cells in mammalian retina in vivo. J Neurophysiol *89*, 2159-2166.

Dreosti, E., Esposti, F., Baden, T., and Lagnado, L. (2011). In vivo evidence that retinal bipolar cells generate spikes modulated by light. Nat Neurosci *14*, 951-952.

Dunn, F.A., Doan, T., Sampath, A.P., and Rieke, F. (2006). Controlling the gain of rod-mediated signals in the Mammalian retina. J Neurosci *26*, 3959-3970.

Dunn, F.A., Lankheet, M.J., and Rieke, F. (2007). Light adaptation in cone vision involves switching between receptor and post-receptor sites. Nature *449*, 603-606.

Dunn, F.A., and Rieke, F. (2006). The impact of photoreceptor noise on retinal gain controls. Curr Opin Neurobiol *16*, 363-370.

Dunn, F.A., and Rieke, F. (2008). Single-photon absorptions evoke synaptic depression in the retina to extend the operational range of rod vision. Neuron *57*, 894-904.

Euler, T., Detwiler, P.B., and Denk, W. (2002). Directionally selective calcium signals in dendrites of starburst amacrine cells. Nature *418*, 845-852.

Euler, T., and Masland, R.H. (2000). Light-evoked responses of bipolar cells in a mammalian retina. J Neurophysiol *83*, 1817-1829.

Feigenspan, A., Teubner, B., Willecke, K., and Weiler, R. (2001). Expression of neuronal connexin36 in AII amacrine cells of the mammalian retina. J Neurosci *21*, 230-239.

Field, G.D., Greschner, M., Gauthier, J.L., Rangel, C., Shlens, J., Sher, A., Marshak, D.W., Litke, A.M., and Chichilnisky, E.J. (2009). High-sensitivity rod photoreceptor input to the blue-yellow color opponent pathway in macaque retina. Nat Neurosci *12*, 1159-1164.

Field, G.D., and Rieke, F. (2002). Nonlinear signal transfer from mouse rods to bipolar cells and implications for visual sensitivity. Neuron *34*, 773-785.

Field, G.D., Sampath, A.P., and Rieke, F. (2005). Retinal processing near absolute threshold: from behavior to mechanism. Annual Review of Physiology *67*, 1-24.

Fletcher, E.L., Hack, I., Brandstatter, J.H., and Wassle, H. (2000). Synaptic localization of NMDA receptor subunits in the rat retina. J Comp Neurol *420*, 98-112.

Freed, M.A. (2000). Parallel cone bipolar pathways to a ganglion cell use different rates and amplitudes of quantal excitation. J Neurosci *20*, 3956-3963.

Freed, M.A., Smith, R.G., and Sterling, P. (2003). Timing of quantal release from the retinal bipolar terminal is regulated by a feedback circuit. Neuron *38*, 89-101.

Gollisch, T., and Meister, M. (2010). Eye smarter than scientists believed: neural computations in circuits of the retina. Neuron *65*, 150-164.

Gong, S., Zheng, C., Doughty, M.L., Losos, K., Didkovsky, N., Schambra, U.B., Nowak, N.J., Joyner, A., Leblanc, G., Hatten, M.E*., et al.* (2003). A gene expression atlas of the central nervous system based on bacterial artificial chromosomes. Nature *425*, 917-925.

Grimes, W.N., Li, W., Chavez, A.E., and Diamond, J.S. (2009). BK channels modulate pre- and postsynaptic signaling at reciprocal synapses in retina. Nat Neurosci *12*, 585-592.

Grimes, W.N., Zhang, J., Graydon, C.W., Kachar, B., and Diamond, J.S. (2010). Retinal parallel processors: more than 100 independent microcircuits operate within a single interneuron. Neuron *65*, 873-885.

Habermann, C.J., O'Brien, B.J., Wassle, H., and Protti, D.A. (2003). AII amacrine cells express L-type calcium channels at their output synapses. J Neurosci *23*, 6904-6913.

Hartveit, E., and Veruki, M.L. (1997). AII amacrine cells express functional NMDA receptors. Neuroreport *8*, 1219-1223.

Heidelberger, R., Heinemann, C., Neher, E., and Matthews, G. (1994). Calcium dependence of the rate of exocytosis in a synaptic terminal. Nature *371*, 513-515.

Hines, M. (1984). Efficient computation of branched nerve equations. Int J Biomed Comput *15*, 69-76.

Hines, M.L., and Carnevale, N.T. (1997). The NEURON simulation environment. Neural Comput *9*, 1179-1209.

Hodgkin, A.L., and Huxley, A.F. (1952). A quantitative description of membrane current and its application to conduction and excitation in nerve. J Physiol *117*, 500-544.

Hsu, S.F., Augustine, G.J., and Jackson, M.B. (1996). Adaptation of Ca(2+)-triggered exocytosis in presynaptic terminals. Neuron *17*, 501-512.

Hu, H.J., and Pan, Z.H. (2002). Differential expression of K+ currents in mammalian retinal bipolar cells. Vis Neurosci *19*, 163-173.

Ichinose, T., and Lukasiewicz, P.D. (2007). Ambient light regulates sodium channel activity to dynamically control retinal signaling. J Neurosci *27*, 4756-4764.

Imredy, J.P., and Yue, D.T. (1994). Mechanism of Ca(2+)-sensitive inactivation of L-type Ca2+ channels. Neuron *12*, 1301-1318.

Izhikevich, E.M. (2007). Dynamical systems in neuroscience : the geometry of excitability and bursting (Cambridge, MA, MIT Press).

Jackman, S.L., Choi, S.Y., Thoreson, W.B., Rabl, K., Bartoletti, T.M., and Kramer, R.H. (2009). Role of the synaptic ribbon in transmitting the cone light response. Nat Neurosci *12*, 303-310.

Jarsky, T., Cembrowski, M., Logan, S.M., Kath, W.L., Riecke, H., Demb, J.B., and Singer, J.H. (2011). A synaptic mechanism for retinal adaptation to luminance and contrast. J Neurosci *31*, 11003-11015.

Jarsky, T., Tian, M., and Singer, J.H. (2010). Nanodomain control of exocytosis is responsible for the signaling capability of a retinal ribbon synapse. J Neurosci *30*, 11885-11895.

Jennings, C., and Aamodt, S. (2000). Computational approaches to brain function. Nature Neuroscience *3*, 1160-1160.

Jeon, C.J., Strettoi, E., and Masland, R.H. (1998). The major cell populations of the mouse retina. J Neurosci *18*, 8936-8946.

Juusola, M., Weckstrom, M., Uusitalo, R.O., Korenberg, M.J., and French, A.S. (1995). Nonlinear models of the first synapse in the light-adapted fly retina. J Neurophysiol *74*, 2538-2547.

Kaneko, Y., and Watanabe, S. (2007). Expression of Nav1.1 in rat retinal AII amacrine cells. Neurosci Lett *424*, 83-88.

Kim, K.J., and Rieke, F. (2001). Temporal contrast adaptation in the input and output signals of salamander retinal ganglion cells. J Neurosci *21*, 287-299.

Klumpp, D.J., Song, E.J., Ito, S., Sheng, M.H., Jan, L.Y., and Pinto, L.H. (1995a). The Shaker-like potassium channels of the mouse rod bipolar cell and their contributions to the membrane current. J Neurosci *15*, 5004-5013.

Klumpp, D.J., Song, E.J., and Pinto, L.H. (1995b). Identification and localization of K+ channels in the mouse retina. Vis Neurosci *12*, 1177-1190.

Korenberg, M.J., Sakai, H.M., and Naka, K. (1989). Dissection of the neuron network in the catfish inner retina. III. Interpretation of spike kernels. J Neurophysiol *61*, 1110-1120.

Kotani, S., Hirasawa, T., Suzuki, T., Sato, K., Sakakibara, M., and Tokimasa, T. (2000). Mechanisms underlying the M-current block by barium in bullfrog sympathetic neurons. Neurosci Lett *285*, 1-4.

Lee, Y.W., and Schetzen, M. (1965). Measuremnt of the Wiener kernels of a nonlinear system by cross-correlation. International Journal of Control *2*, 237-254.

Levitan, B., and Buchsbaum, G. (1996). Parallel cone bipolar to on-beta ganglion cell pathways in the cat retina: spatial responses, spatial aliasing, and spatial variance. J Opt Soc Am A Opt Image Sci Vis *13*, 1152-1165.

Li, X., Kamasawa, N., Ciolofan, C., Olson, C.O., Lu, S., Davidson, K.G., Yasumura, T., Shigemoto, R., Rash, J.E., and Nagy, J.I. (2008). Connexin45-containing neuronal gap junctions

in rodent retina also contain connexin36 in both apposing hemiplaques, forming bihomotypic gap junctions, with scaffolding contributed by zonula occludens-1. J Neurosci *28*, 9769-9789.

Liang, Z., and Freed, M.A. (2010). The ON pathway rectifies the OFF pathway of the mammalian retina. J Neurosci *30*, 5533-5543.

Ma, Y.P., Cui, J., Hu, H.J., and Pan, Z.H. (2003). Mammalian retinal bipolar cells express inwardly rectifying K+ currents (IKir) with a different distribution than that of Ih. J Neurophysiol *90*, 3479-3489.

Ma, Y.P., and Pan, Z.H. (2003). Spontaneous regenerative activity in mammalian retinal bipolar cells: roles of multiple subtypes of voltage-dependent Ca2+ channels. Vis Neurosci *20*, 131-139.

Manookin, M.B., Beaudoin, D.L., Ernst, Z.R., Flagel, L.J., and Demb, J.B. (2008). Disinhibition combines with excitation to extend the operating range of the OFF visual pathway in daylight. J Neurosci *28*, 4136-4150.

Manookin, M.B., and Demb, J.B. (2006). Presynaptic mechanism for slow contrast adaptation in mammalian retinal ganglion cells. Neuron *50*, 453-464.

Mao, B.Q., MacLeish, P.R., and Victor, J.D. (1998). The intrinsic dynamics of retinal bipolar cells isolated from tiger salamander. Vis Neurosci *15*, 425-438.

Margolis, D.J., and Detwiler, P.B. (2007). Different mechanisms generate maintained activity in ON and OFF retinal ganglion cells. J Neurosci *27*, 5994-6005.

Marmarelis, P.Z., and Marmarelis, V.Z. (1978). Analysis of physiological systems: the white-noise approach (New York, Plenum Press).

Marmarelis, P.Z., and Naka, K.I. (1973). Nonlinear analysis and synthesis of receptive-field responses in the catfish retina. II. One-input white-noise analysis. J Neurophysiol *36*, 619-633.

Masland, R.H. (2001). The fundamental plan of the retina. Nat Neurosci *4*, 877-886.

Matthews, G. (1999). Synaptic mechanisms of bipolar cell terminals. Vision Res *39*, 2469-2476.

Matthews, G., and Fuchs, P. (2010). The diverse roles of ribbon synapses in sensory neurotransmission. Nat Rev Neurosci *11*, 812-822.

Maxeiner, S., Dedek, K., Janssen-Bienhold, U., Ammermuller, J., Brune, H., Kirsch, T., Pieper, M., Degen, J., Kruger, O., Willecke, K.*, et al.* (2005). Deletion of connexin45 in mouse retinal neurons disrupts the rod/cone signaling pathway between AII amacrine and ON cone bipolar cells and leads to impaired visual transmission. J Neurosci *25*, 566-576.

Mennerick, S., and Matthews, G. (1996). Ultrafast exocytosis elicited by calcium current in synaptic terminals of retinal bipolar neurons. Neuron *17*, 1241-1249.

Mills, S.L., and Massey, S.C. (1995). Differential properties of two gap junctional pathways made by AII amacrine cells. Nature *377*, 734-737.

Morkve, S.H., Veruki, M.L., and Hartveit, E. (2002). Functional characteristics of non-NMDA-type ionotropic glutamate receptor channels in AII amacrine cells in rat retina. J Physiol *542*, 147-165.

Munch, T.A., da Silveira, R.A., Siegert, S., Viney, T.J., Awatramani, G.B., and Roska, B. (2009). Approach sensitivity in the retina processed by a multifunctional neural circuit. Nat Neurosci *12*, 1308-1316.

Murphy, G.J., and Rieke, F. (2006). Network variability limits stimulus-evoked spike timing precision in retinal ganglion cells. Neuron *52*, 511-524.

Murphy, G.J., and Rieke, F. (2008). Signals and noise in an inhibitory interneuron diverge to control activity in nearby retinal ganglion cells. Nat Neurosci *11*, 318-326.

Nelson, R. (1982). AII amacrine cells quicken time course of rod signals in the cat retina. J Neurophysiol *47*, 928-947.

Oesch, N., and Diamond, J. (2009). A night vision neuron gets a day job. Nat Neurosci *12*, 1209-1211.

Oesch, N., Euler, T., and Taylor, W.R. (2005). Direction-selective dendritic action potentials in rabbit retina. Neuron *47*, 739-750.

Oltedal, L., and Hartveit, E. (2010). Transient release kinetics of rod bipolar cells revealed by capacitance measurement of exocytosis from axon terminals in rat retinal slices. J Physiol *588*, 1469-1487.

Oltedal, L., Veruki, M.L., and Hartveit, E. (2009). Passive membrane properties and electrotonic signal processing in retinal rod bipolar cells. Journal of Physiology-London *587*, 829-849.

Palmer, M.J. (2006). Modulation of Ca(2+)-activated K+ currents and Ca(2+)-dependent action potentials by exocytosis in goldfish bipolar cell terminals. J Physiol *572*, 747-762.

Palmer, M.J., Hull, C., Vigh, J., and von Gersdorff, H. (2003). Synaptic cleft acidification and modulation of short-term depression by exocytosed protons in retinal bipolar cells. J Neurosci *23*, 11332-11341.

Pan, Z.H. (2000). Differential expression of high- and two types of low-voltage-activated calcium currents in rod and cone bipolar cells of the rat retina. J Neurophysiol *83*, 513-527.

Pan, Z.H., and Hu, H.J. (2000). Voltage-dependent Na(+) currents in mammalian retinal cone bipolar cells. J Neurophysiol *84*, 2564-2571.

Pan, Z.H., Hu, H.J., Perring, P., and Andrade, R. (2001). T-type Ca(2+) channels mediate neurotransmitter release in retinal bipolar cells. Neuron *32*, 89-98.

Pang, J.J., Gao, F., and Wu, S.M. (2004). Light-evoked current responses in rod bipolar cells, cone depolarizing bipolar cells and AII amacrine cells in dark-adapted mouse retina. J Physiol *558*, 897-912.

Petrides, A., and Trexler, E.B. (2008). Differential output of the high sensitivity rod photoreceptor: AII amacrine pathway. Journal of Comparative Neurology *507*, 1653-1662.

Protti, D.A., Flores-Herr, N., and von Gersdorff, H. (2000). Light evokes Ca2+ spikes in the axon terminal of a retinal bipolar cell. Neuron *25*, 215-227.

Publio, R., Oliveira, R.F., and Roque, A.C. (2009). A computational study on the role of gap junctions and rod Ih conductance in the enhancement of the dynamic range of the retina. PLoS One *4*, e6970.

Rall, W. (1977). Core Conductor Theory and Cable Properties of Neurons. In Handbook of Physiology: Cellular Biology of Neurons, E.R. Kandel, J.M. Brookhardt, and V.M. Mountcastle, eds. (Bethesda, MD, American Physiological Society), pp. 39-97.

Rall, W., and Rinzel, J. (1973). Branch input resistance and steady attenuation for input to one branch of a dendritic neuron model. Biophys J *13*, 648-687.

Raviola, E., and Dacheux, R.F. (1987). Excitatory dyad synapse in rabbit retina. Proc Natl Acad Sci USA *84*, 7324-7328.

Rieke, F. (2001). Temporal contrast adaptation in salamander bipolar cells. J Neurosci *21*, 9445-9454.

Robbins, J., Trouslard, J., Marsh, S.J., and Brown, D.A. (1992). Kinetic and pharmacological properties of the M-current in rodent neuroblastoma x glioma hybrid cells. J Physiol *451*, 159-185.

Sampath, A.P., and Rieke, F. (2004). Selective transmission of single photon responses by saturation at the rod-to-rod bipolar synapse. Neuron *41*, 431-443.

Schnee, M.E., and Brown, B.S. (1998). Selectivity of linopirdine (DuP 996), a neurotransmitter release enhancer, in blocking voltage-dependent and calcium-activated potassium currents in hippocampal neurons. J Pharmacol Exp Ther *286*, 709-717.

Scott, L.L., Hage, T.A., and Golding, N.L. (2007). Weak action potential backpropagation is associated with high-frequency axonal firing capability in principal neurons of the gerbil medial superior olive. J Physiol *583*, 647-661.

Shapley, R. (1997). Retinal physiology: adapting to the changing scene. Curr Biol *7*, R421-423.

Shapley, R.M., and Enroth-Cugell, C. (1984). Visual adaptation and retinal gain controls. Prog Retinal Res *3*, 263-346.

Sharpe, L.T., and Stockman, A. (1999). Rod pathways: the importance of seeing nothing. Trends Neurosci *22*, 497-504.

Siegert, S., Scherf, B.G., Del Punta, K., Didkovsky, N., Heintz, N., and Roska, B. (2009). Genetic address book for retinal cell types. Nat Neurosci *12*, 1197-1204.

Singer, J.H. (2007). Multivesicular release and saturation of glutamatergic signalling at retinal ribbon synapses. J Physiol *580*, 23-29.

Singer, J.H., and Diamond, J.S. (2003). Sustained Ca2+ entry elicits transient postsynaptic currents at a retinal ribbon synapse. J Neurosci *23*, 10923-10933.

Singer, J.H., and Diamond, J.S. (2006). Vesicle depletion and synaptic depression at a mammalian ribbon synapse. J Neurophysiol *95*, 3191-3198.

Singer, J.H., Lassova, L., Vardi, N., and Diamond, J.S. (2004). Coordinated multivesicular release at a mammalian ribbon synapse. Nat Neurosci *7*, 826-833.

Smith, R.G., and Vardi, N. (1995). Simulation of the AII amacrine cell of mammalian retina: functional consequences of electrical coupling and regenerative membrane properties. Vis Neurosci *12*, 851-860.

Snellman, J., Zenisek, D., and Nawy, S. (2009). Switching between transient and sustained signalling at the rod bipolar-AII amacrine cell synapse of the mouse retina. J Physiol *587*, 2443-2455.

Sterling, P., Freed, M.A., and Smith, R.G. (1988). Architecture of rod and cone circuits to the on-beta ganglion cell. J Neurosci *8*, 623-642.

Sterling, P., and Matthews, G. (2005). Structure and function of ribbon synapses. Trends Neurosci *28*, 20-29.

Strettoi, E., and Masland, R.H. (1996). The number of unidentified amacrine cells in the mammalian retina. Proc Natl Acad Sci USA *93*, 14906-14911.

Strettoi, E., Raviola, E., and Dacheux, R.F. (1992). Synaptic connections of the narrow-field, bistratified rod amacrine cell (AII) in the rabbit retina. J Comp Neurol *325*, 152-168.

Stuart, G., Spruston, N., and Häusser, M. (1999). Dendrites (Oxford ; New York, Oxford University Press).

Tamalu, F., and Watanabe, S. (2007). Glutamatergic input is coded by spike frequency at the soma and proximal dendrite of AII amacrine cells in the mouse retina. Eur J Neurosci *25*, 3243-3252.

Tian, M., Jarsky, T., Murphy, G.J., Rieke, F., and Singer, J.H. (2010). Voltage-gated Na channels in AII amacrine cells accelerate scotopic light responses mediated by the rod bipolar cell pathway. J Neurosci *30*, 4650-4659.

Trexler, E.B., Li, W., and Massey, S.C. (2005). Simultaneous contribution of two rod pathways to AII amacrine and cone bipolar cell light responses. J Neurophysiol *93*, 1476-1485.

Tsukamoto, Y., Morigiwa, K., Ueda, M., and Sterling, P. (2001). Microcircuits for night vision in mouse retina. J Neurosci *21*, 8616-8623.

van Wyk, M., Wassle, H., and Taylor, W.R. (2009). Receptive field properties of ON- and OFF-ganglion cells in the mouse retina. Vis Neurosci *26*, 297-308.

Vardi, N., and Smith, R.G. (1996). The AII amacrine network: coupling can increase correlated activity. Vision Res *36*, 3743-3757.

Veruki, M.L., and Hartveit, E. (2002a). AII (Rod) amacrine cells form a network of electrically coupled interneurons in the mammalian retina. Neuron *33*, 935-946.

Veruki, M.L., and Hartveit, E. (2002b). Electrical synapses mediate signal transmission in the rod pathway of the mammalian retina. J Neurosci *22*, 10558-10566.

Veruki, M.L., Morkve, S.H., and Hartveit, E. (2003). Functional properties of spontaneous EPSCs and non-NMDA receptors in rod amacrine (AII) cells in the rat retina. J Physiol *549*, 759-774.

Veruki, M.L., Oltedal, L., and Hartveit, E. (2008). Electrical synapses between AII amacrine cells: dynamic range and functional consequences of variation in junctional conductance. J Neurophysiol *100*, 3305-3322.

Veruki, M.L., Oltedal, L., and Hartveit, E. (2010). Electrical coupling and passive membrane properties of AII amacrine cells. J Neurophysiol *103*, 1456-1466.

Volgyi, B., Deans, M.R., Paul, D.L., and Bloomfield, S.A. (2004). Convergence and segregation of the multiple rod pathways in mammalian retina. J Neurosci *24*, 11182-11192.

Volterra, V. (1959). Theory of functionals and of integral and integro-differential equations. (New York, NY, Dover Publications).

von Gersdorff, H., and Matthews, G. (1996). Calcium-dependent inactivation of calcium current in synaptic terminals of retinal bipolar neurons. J Neurosci *16*, 115-122.

von Gersdorff, H., and Matthews, G. (1997). Depletion and replenishment of vesicle pools at a ribbon-type synaptic terminal. J Neurosci *17*, 1919-1927.

von Gersdorff, H., and Matthews, G. (1999). Electrophysiology of synaptic vesicle cycling. Annu Rev Physiol *61*, 725-752.

Walraven, J., Enroth-Cugell, C., Hood, D.C., Macleod, D.I.A., and Schnapf, J.L. (1990). The control of visual sensitivity. In Visual Perception: The Neurophysiological Foundations, L. Spillman, and J.S. Werner, eds. (Academic Press), pp. 53-101.

Wang, H.S., Pan, Z., Shi, W., Brown, B.S., Wymore, R.S., Cohen, I.S., Dixon, J.E., and McKinnon, D. (1998). KCNQ2 and KCNQ3 potassium channel subunits: molecular correlates of the M-channel. Science *282*, 1890-1893.

Wang, Y.V., Weick, M., and Demb, J.B. (2011). Spectral and temporal sensitivity of cone-mediated responses in mouse retinal ganglion cells. J Neurosci *31*, 7670-7681.

Wassle, H., Grunert, U., and Rohrenbeck, J. (1993). Immunocytochemical staining of AII-amacrine cells in the rat retina with antibodies against parvalbumin. J Comp Neurol *332*, 407-420.

Wiener, N. (1949). Extrapolation, interpolation, and smoothing of stationary time series (Cambridge, MA, MIT Press).

Wiener, N. (1958). Nonlinear problems in random theory (Cambridge, MA, MIT Press).

Wu, C., Ivanova, E., Cui, J., Lu, Q., and Pan, Z.H. (2011). Action potential generation at an axon initial segment-like process in the axonless retinal AII amacrine cell. J Neurosci *31*, 14654-14659.

Xin, D., and Bloomfield, S.A. (1999). Comparison of the responses of AII amacrine cells in the dark- and light-adapted rabbit retina. Vis Neurosci *16*, 653-665.

Xu, J., and Wu, L.G. (2005). The decrease in the presynaptic calcium current is a major cause of short-term depression at a calyx-type synapse. Neuron *46*, 633-645.

Zaczek, R., Chorvat, R.J., Saye, J.A., Pierdomenico, M.E., Maciag, C.M., Logue, A.R., Fisher, B.N., Rominger, D.H., and Earl, R.A. (1998). Two new potent neurotransmitter release enhancers, 10,10-bis(4-pyridinylmethyl)-9(10H)-anthracenone and 10,10-bis(2-fluoro-4-pyridinylmethyl)-9(10H)-anthracenone: comparison to linopirdine. J Pharmacol Exp Ther *285*, 724-730.

Zador, A.M., Agmon-Snir, H., and Segev, I. (1995). The morphoelectrotonic transform: a graphical approach to dendritic function. J Neurosci *15*, 1669-1682.

Zaghloul, K.A., Boahen, K., and Demb, J.B. (2003). Different circuits for ON and OFF retinal ganglion cells cause different contrast sensitivities. J Neurosci *23*, 2645-2654.

Zaghloul, K.A., Boahen, K., and Demb, J.B. (2005). Contrast adaptation in subthreshold and spiking responses of mammalian Y-type retinal ganglion cells. J Neurosci *25*, 860-868.

Zhou, Z.J., and Fain, G.L. (1996). Starburst amacrine cells change from spiking to nonspiking neurons during retinal development. Proc Natl Acad Sci USA *93*, 8057-8062.

Zhou, Z.Y., Wan, Q.F., Thakur, P., and Heidelberger, R. (2006). Capacitance measurements in the mouse rod bipolar cell identify a pool of releasable synaptic vesicles. J Neurophysiol *96*, 2539-2548.